ADVERTIMENT. La consulta d'aquesta tesi queda condicionada a l'acceptació de les següents condicions d'ús: La difusió d'aquesta tesi per mitjà del servei TDX (www.tesisenxarxa.net) ha estat autoritzada pels titulars dels drets de propietat intel·lectual únicament per a usos privats emmarcats en activitats d'investigació i docència. No s'autoritza la seva reproducció amb finalitats de lucre ni la seva difusió i posada a disposició des d'un lloc aliè al servei TDX. No s'autoritza la presentació del seu contingut en una finestra o marc aliè a TDX (framing). Aquesta reserva de drets afecta tant al resum de presentació de la tesi com als seus continguts. En la utilització o cita de parts de la tesi és obligat indicar el nom de la persona autora.

ADVERTENCIA. La consulta de esta tesis queda condicionada a la aceptación de las siguientes condiciones de uso: La difusión de esta tesis por medio del servicio TDR (www.tesisenred.net) ha sido autorizada por los titulares de los derechos de propiedad intelectual únicamente para usos privados enmarcados en actividades de investigación y docencia. No se autoriza su reproducción con finalidades de lucro ni su difusión y puesta a disposición desde un sitio ajeno al servicio TDR. No se autoriza la presentación de su contenido en una ventana o marco ajeno a TDR (framing). Esta reserva de derechos afecta tanto al resumen de presentación de la tesis como a sus contenidos. En la utilización o cita de partes de la tesis es obligado indicar el nombre de la persona autora.

WARNING. On having consulted this thesis you're accepting the following use conditions: Spreading this thesis by the TDX (www.tesisenxarxa.net) service has been authorized by the titular of the intellectual property rights only for private uses placed in investigation and teaching activities. Reproduction with lucrative aims is not authorized neither its spreading and availability from a site foreign to the TDX service. Introducing its content in a window or frame foreign to the TDX service is not authorized (framing). This rights affect to the presentation summary of the thesis as well as to its contents. In the using or citation of parts of the thesis it's obliged to indicate the name of the author

Universitat Politècnica de Catalunya
Institut d'Estudis Espacials de Catalunya

Multi-dimensional Simulations of Mixing in Classical Novae

by

Jordi Casanova i Bustamante

A thesis submitted for the degree of

Doctor of Philosophy

Advisors:
Jordi José i Pont
Enrique García–Berro Montilla

Barcelona, June 2011

Contents

List of Figures

List of Tables

Chapter 1

Introduction

During the past 60 years large theoretical and observational efforts have been invested in studying classical novae. The theoretical efforts comprise both numerical studies and nuclear experiments, while the observational efforts encompass detailed photometric and spectroscopic analyses at almost all wavelengths. The discovery of the binary nature of this phenomenon, the first theories that revealed its thermonuclear origin and the first one-dimensional hydrodynamical simulations, among other advances, started to constrain the underlying physics of novae and paved the road to understand these unique stellar explosions. All these efforts have helped in constructing a reliable theory, the so-called *thermonuclear runaway model*, that provides a solid explanation of several characteristics of nova events. However, being many and impressive the achievements of this model, there are still many facets of nova outbursts that remain to be thoroughly explored and for which a satisfactory explanation is lacking.

1.1 Novae as cataclysmic variables

Cataclysmic variables (hereafter, CVs) are close binary systems composed of a compact object (either a CO or an ONe white dwarf) and a companion star which can be a main-sequence star, a hydrogen-rich white dwarf, a red giant — known as Algol-like CVs — a helium white dwarf or a helium star — also known as helium CVs (Iben & Fujimoto, 2008). Each star is characterized by its Roche lobe, which is defined as the influence area surrounding the star due to its gravitational field. Matter which is located within the Roche lobe is bound to the star and cannot escape. In CVs, the companion star is filling (or almost filling) its Roche-Lobe. It is worth mentioning that about 25% of all CVs host a magnetic primary star (and thereof, the name of magnetic CVs). Those CVs that have very strong magnetic fields ($B \geq 10^7$ G) are named polar CVs. In this group of stars, accretion proceeds along the magnetic poles of the compact object, and thus, an accretion disk is not formed. In intermediate polar CVs, the magnetic field is softer ($10^6 \leq B \leq 10^7$ G) and an accretion disk can be formed, although the inner regions are truncated (Warner, 2008). Classical novae are a particular sub-class of CVs, in which accretion of hydrogen-rich matter on top of the surface of the white dwarf causes a thermonuclear runaway. Novae can be classified as CO or ONe novae, depending on the composition of the accreting white dwarf (the later being more massive). Because of the high temperatures achieved during the outbursts, nova envelopes undergo substantial nuclear processing. Indeed, the nuclear activity in ONe novae goes beyond the CNO mass region, moving towards the MgAl and NeNa regions, while heavier isotopes are produced.

The existence of novae (stars that become brighter in the sky) has been known for centuries, but a consistent theory was not accepted until the last century (Duerbeck, 2008). Already in the 18th century, Newton (1726) proposed that novae could be driven by accretion of comets, and hence would appear as brighter stars in the sky after burning the extra fuel. Late in the 19th century Pickering (1895), among others, postulated that some spectral features observed in novae may be explained by mass ejection from a star. Later on, Schatzman (1949, 1951), Cameron (1959) and Gurevitch & Lebedinsky (1957) contributed to describe the thermonuclear nature of classical novae, which indeed was responsible of the sudden explosion on the very outer layers of the compact star. Again from observational studies, Walker (1954) postulated the binarity of novae, which translated into a large step towards the complete knowledge of the phenomenon. Kraft (1963, 1964) confirmed its binary nature and also introduced the fact that the thermonuclear runaway would take place after the accreting episode of hydrogen-rich matter on top of the compact star, an idea that was also suggested by Paczyński (1965). The observational advances and the thermonuclear studies merged and set the basis of the modern classical nova theory, which started with the beginning of computational simulations, 40 years ago, when Sparks (1969) carried out the first hydrodynamical calculation.

1.2 The thermonuclear runaway model

Classical novae are stellar explosions that take place in close stellar binary systems (José et al., 2006; José & Hernanz, 2007b; Starrfield et al., 2008), with orbital periods in the range 1-15 h. The primary is a degenerate, white dwarf star, while the secondary is a low-mass, K-M dwarf, main sequence star (although there is evidence pointing towards more evolved companions in some cases). The secondary fills its Roche lobe and matter from its outer layers starts flowing through the inner Lagrangian point L_1 (the point at which the two Roche lobes intersect) and spirals in towards the white dwarf. Since this material carries angular momentum, it forms an accretion disk around the white dwarf component. A fraction of this material ultimately piles up on top of the white dwarf (for about 10^5 years). These mass-transfer episodes result in accretion of hydrogen-rich matter on the primary at typical rates ranging from 10^{-10} to $10^{-9}\, M_\odot$ yr^{-1}, accumulating between 10^{-5} and $10^{-4}\, M_\odot$ on top of the white dwarf. Accretion proceeds until $T \sim 2.5 \times 10^7$ K, when the accretion timescale becomes larger than the nuclear timescale ($\tau_{\rm acc} > \tau_{\rm nuc}$). Matter accumulates and compresses in partially degenerate conditions, due to the high densities attained. As a result, the envelope is heated, but since the material is degenerate, the temperature rise is not accompanied by the expansion of the envelope layers, paving the road for a thermonuclear explosion.

When the temperature is high enough, say $T \sim 10^7$ K, thermonuclear reactions can take place, first through the pp chains, followed by an extension of the nuclear activity towards the CNO cycle. Consequently, hydrogen is ignited, but since pressure is almost insensitive to temperature, matter undergoes a thermonuclear runaway, driven by (p,α) and (p,γ) reactions, together with β^+ disintegrations (José et al., 2006). The runaway is basically triggered by the ^{12}C(p,γ)^{13}N reaction (José & Hernanz, 2008). However, it is worth mentioning that in low metallicity binaries, some studies suggest that the triggering reaction could be ^{14}N(p,γ)^{15}O (Shen & Bildsten, 2009), although the importance of ^{12}C(p,γ)^{13}N cannot be excluded at all. Nevertheless, the suite of nuclear processes suggested to operate during nova outbursts are unable to reproduce the observed high metallicities (much above solar) inferred from the ejecta. Therefore, it is widely accepted that some mixing has to take place at the core-envelope interface to account for the inferred metallicity enhancements — typically, $Z = 0.25$ to 0.50 (Gehrz et al., 1998). This is assumed to operate through injection of fresh ^{12}C from the outer layers of the white dwarf core into the envelope. In essence, the mixing process, whose origin has remained unsolved over the past 40 years, is the key ingredient to reproduce the nucleosynthetic pattern inferred from classical nova explosions.

As the temperature at the base of the envelope increases, burning continues and nuclear activity settles in the cold mode of the CNO cycle, proceeding via the chain of reactions ^{12}C(p,γ)^{13}N(β^+)^{13}C(p,γ)^{14}N. At this stage, the nuclear timescale becomes smaller than the dynamical timescale, $\tau_{\rm nuc} < \tau_{\rm dyn}$, and hence burning continues while the temperature in the accreted envelope keeps raising. Vast amounts of energy are released that cannot be removed by means of conductive and radiative processes anymore, and convection sets in. Convection plays a main role in the thermonuclear runaway, since it will spread the local perturbations and drive further mixing. At high temperatures, $T \sim 10^8$ K, the timescale for proton capture onto ^{13}N becomes shorter than the corresponding disintegration time. This leads the nuclear activity towards the hot CNO cycle, which is basically driven by the chain of reactions ^{12}C(p,γ)^{13}N(p,γ)^{14}O, ^{14}N(p,γ)^{15}O and ^{16}O(p,γ)^{17}F (José & Hernanz, 1998). A fraction of the very abundant and short-lived isotopes ^{13}N ($\tau_{1/2} = 866$ s), ^{14}O ($\tau_{1/2} = 102$ s), ^{15}O ($\tau_{1/2} = 176$ s), and ^{17}F ($\tau_{1/2} = 93$ s), that are produced in the nuclear reactions of the CNO-cycle, are transported to the outermost layers of the envelope by convection before decaying, because the turnover time for convection is smaller than the timescale for β^+ decays (Starrfield et al., 1972). In the outermost layers of the envelope, these isotopes are not destroyed by proton captures because of the lower temperatures. In these cold layers, these unstable isotopes disintegrate releasing a huge amount of energy. Degeneracy is then lifted. In fact, this is the key ingredient that powers the expansion and ejection stages of the explosion, since it provides the external layers with the required kinetic energy to escape (Starrfield et al., 1972). As a consequence, it is expected that the products of these β^+ disintegrations (i.e., ^{13}C, ^{14}N, ^{15}N, and ^{17}O) would have sizable abundances in the ejecta.

The thermonuclear runaway that defines a classical nova outburst lasts for a few minutes and drives peak temperatures between ~ 1 and 4×10^8 K. The suite of nuclear processes that operate in the envelope results in non-solar isotopic abundance ratios in the ejecta. During these events about $10^{-4} - 10^{-5}\, M_\odot$, enriched in CNO and/or other intermediate-mass elements, are ejected into the interstellar medium with velocities that achieve $\sim 10^3$ km s^{-1}. In fact, it is believed that novae are the major sources of ^{13}C and ^{17}O in the Galaxy (José & Hernanz, 1998; José et al., 2006; José & Hernanz, 2007b; Starrfield et al., 1998, 2008). Moreover, they also contribute, to some extent, to the Galactic abundance of ^{15}N. Other species, like ^{31}P, ^{32}S, or ^{35}Cl can also be produced in the most massive ONe novae (José, 1996; José & Hernanz, 1998; José, 2005; José et al., 2006; José & Hernanz, 2007b, 2008). Neon novae can accrete more matter than carbon-oxygen novae because the presence of ^{12}C in the outer white dwarf layers is smaller. Thus, accretion proceeds for a longer period of time before ignition. Additionally, the level of degeneracy is larger in ONe novae because of its higher density. All this translates into higher peak temperatures and a nuclear activity that extends towards heavier isotopes (NeNa and MgAl mass regions). Instead, carbon-oxygen novae have a more limited production of isotopes, since the nuclear activity does not proceed beyond the CNO region. The nucleosynthetic endpoint of classical novae explosions is around ^{40}Ca (José & Hernanz, 1998), but it is worth mentioning that recent studies suggest that explosions in extremely metal-defficient (primordial) novae may reach Cu-Zn (José et al., 2007; José & Hernanz, 2008). Actually, the small range of temperatures and the limited number of isotopes involved make classical novae unique explosive stellar events that can be used to constrain nuclear inputs, and vice versa. Several studies have been carried out to measure accurate rates of the key reactions and to limit their uncertainties (José et al., 1999a; Iliadis et al., 2002). This issue has a large impact on the accuracy of the final abundances of the elements synthetized in a nova outburst. Among all the nuclear processes, some reactions are still affected by large uncertainties (José et al., 1999a; Iliadis et al., 2002; José et al., 2006). In particular, more efforts should be made to evaluate and restrict the rates of ^{18}F(p,α), ^{25}Al(p,γ) and ^{30}P(p,γ).

1.3 Classical novae: observational constraints

The thermonuclear runaway theory described in the previous section is the result of numerous hydrodynamical calculations. These calculations had been complemented with observational efforts and nuclear physics experiments to better understand the physics of classical novae. In particular, the predictions of the thermonuclear runaway theory need to be confirmed by observations, while nuclear astrophysics provides more accurate nuclear information. In the following sections, we summarize the contribution from observations and nuclear astrophysics to the the theory of classical novae.

1.3.1 Observational properties

The Galactic rate of classical novae explosions is 30 ± 10 yr^{-1} (Shafter, 2002), but around the plane and bulge of the Galaxy the rate is larger (Warner, 2008). Nova explosions have a very distinctive light curve, characterized by a sudden rise in brightness magnitude (by 8–18 magnitudes) and peak luminosities in the range 10^4–10^5 $L_\odot$. Many novae present a pre-maximum halt and a final rise of about 2 magnitudes. This first phase, which lasts only for a few days is followed by a decline phase, the duration of which varies depending upon the nature of the nova. Payne-Gaposchkin (1957) classified nova light curves as a function of the time needed to decrease 2 magnitudes. For instance, very fast or fast requiere less than 25 days, while slow novae would need more than 81 days (250 days for the very slow nova class). Additionally, some novae experience a quiet decrease of their light curve, whereas some other exhibit oscillations of about 1.5 magnitudes or go through a transition phase (decreasing from 7 to 10 magnitudes) for months until recovery (Warner, 2008). All novae are supposed to recur with periods ranging from $\sim 10^4$ to 10^5 yr (except for the recurrent nova class, with recurrence times of ~ 100 yr) (Warner, 2008).

γ-ray emission is also one of the important signatures of novae. The predicted emission of γ-rays from novae is closely related to the synthesis of ^{7}Be(^{7}Li), ^{13}N, ^{18}F, ^{22}Na and ^{26}Al. Preliminary studies of the potential γ-ray signatures associated with such explosions (Clayton & Hoyle, 1974; Clayton, 1981; Leising & Clayton, 1987) already pointed in this direction. From then on, several satellites such as the International Gamma-Ray Astrophysics Laboratory (INTEGRAL) or the Compton Gamma-Ray Observatory (CGRO), among others, have surveyed the sky to detect γ-ray emission. Also, many efforts have been made on the theoretical side to accurately model this γ-ray emission. Both ^{13}N and ^{18}F have short lifetimes (862 s and 158 min respectively) and disintegrate by emitting positrons, which experience electron-positron annihilation. Thus, these two isotopes power a line emission at 511 keV and a lower-energy continuum (due to positronium emission and comptonization), with a cut-off at $\sim 20 - 30$ keV. ^{22}Na and ^{26}Al instead, have longer lifetimes, $\tau = 3.75$ yr and $\tau = 10^6$ yr respectively, and produce line emission at

1.275 keV and 1.809 keV (detected by HEAO 3 and COMPTEL) respectively, plus some contribution to the 511 keV line in both cases. ^{7}Be has an intermediate lifetime (τ = 77 d) and produces an emission line at 478 keV after capturing an electron (Hernanz, 2008). The electron-positron annihilation line and the continuum produced right after the outburst, represent the strongest (but shortest) γ-ray signal. The continuum contains information on the expanding envelope after the explosion (Gomez-Gomar et al., 1998; Hernanz et al., 1999). Whereas both ONe and CO novae produce ^{13}N and ^{18}F, the emission corresponding to ^{7}Be is more likely associated to CO novae (Hernanz et al., 1996), while the emission from ^{22}Na (and ^{26}Al) would definitely point to an ONe nova (Jose et al., 1997; José et al., 1999b). It is worth noting that only the cumulative emission from ^{26}Al can be observed, since its lifetime is much longer than the nova recurrence time. Unfortunately, the contribution of novae to the Galactic levels of ^{26}Al is not well known. Note as well that the cumulative emission from ^{22}Na could also be observed.

Studies of X-ray emission reveal details of the behavior of classical novae during their hot stages. Over the past three decades EXOSAT, ROSAT, BEPPOSAX, CHANDRA and XMM have surveyed the sky and have contributed to constrain some properties of novae (Krautter, 2008). Basically, X-ray emission manifests as hard X-rays, due to shocks between the ejecta and the surrounding area, and/or soft X-rays, related to residual nuclear burning on top of the white dwarf after the explosion (Starrfield et al., 1974; Starrfield, 1989; Sala & Hernanz, 2005). This X-ray emission is important since it is known that its duration is linked to the amount of mass that remains on top of the white dwarf after the outburst. This emission can last from a few months, for the most massive white dwarfs, to a few years — see Henze et al. (2009) and references therein. Thus, the soft X-ray emission offers a unique tool to unveil the possible role of classical and recurrent novae as potential type Ia supernova progenitors.

The identification of pre-solar grains of putative nova origin also helps in constraining the theoretical models (José & Shore, 2008). It is now widely accepted that novae are factories of presolar grains, as shown by infrared (Evans, 1990; Gehrz et al., 1998; Gehrz, 1999) and ultraviolet studies (Shore et al., 1994b). Preliminary studies suggested that presolar nova grains could be identified by a number of specific signatures due to the overproduction of ^{13}C, ^{14}C, ^{18}O, ^{22}Na, ^{26}Al, ^{30}Si (Clayton & Hoyle, 1976). For instance, a low ^{20}Ne/^{22}Ne ratio would be a clear signature of a nova explosion: since noble gases, such as Ne, do not easily condense, this would be interpreted as due to in situ decay of ^{22}Na trapped in the grain. A few isolated pre-solar grains, five SiC and two graphite grains, from the Murchison and Acfer meteorites have shown imprints characteristic of nova nucleosynthesis, such as low ^{12}C/^{13}C and ^{14}N/^{15}N, high ^{30}Si/^{28}Si ratios, close-to-solar ^{29}Si/^{28}Si ratios, a high ^{26}Al/^{27}Al ratio for two of the grains and low ^{20}Ne/^{22}Ne ratio only for one grain (Amari et al., 2001; Amari, 2002; José et al., 2004). A major concern for the firm identification of these grains as nova grains was that in order to match grain data, models had to assume that the ejected material mixed with ten times close-to-solar material (José & Shore, 2008). More recently, three additional SiC grains from the Murchison meteorite were analyzed by Nittler & Hoppe (2005), revealing low carbon and nitrogen ratios as the previous nova candidate grains but also Ti in non-solar ratios which pointed towards a supernova progenitor. Although both samples are not isotopically identical, and Ti production in novae cannot be ruled out under some extreme conditions, such as low-luminosity white dwarfs (José & Hernanz, 2007a), slow white dwarf accretors (Glasner & Truran, 2009) or primordial novae (José et al., 2007), this stresses the need to rely on a large number of isotopes before conclusions on grain paternity can be firmly established.

1.4 Open questions

As it becomes clear from the previous sections, classical novae have been vastly studied during the last decades, and using many different tools (observations, theory and simulations). All these studies have helped to understand the gross features of a nova explosion. However, there are still some open issues which are needed to complete the puzzle. Amongst them we mention the following ones. Firstly, there is still some discrepancy between the amount of ejected mass inferred from observations and the values reported from hydrodynamic simulations. Indeed, observations yield larger ejected masses, implying that the contribution of novae to the Galactic abundances is still uncertain. Another relevant issue is the production of ^{7}Li. The detection of ^{7}Li would confirm one of the predictions of the thermonuclear runaway model, since current simulations predict a large overproduction of this isotope in CO novae. More experimental and theoretical efforts are also needed to shed light on the specific contribution of novae to the Galactic ^{26}Al. Also, theoretical models predict the presence of potential γ-ray emmitters in the nova ejecta. The detection of γ-rays from novae would confirm important predictions of the thermonuclear runaway model. Another important and yet unexplained phenomenon is the inhomogeneous distribution of abundances as seen in the ejecta, an aspect that one-dimensional models cannot reproduce. Finally, despite the important efforts devoted during the past 20 years to multi-dimensional nova simulations, the nature of the mixing process that operates at the core-envelope interface remains still unsolved.

1.5 Mixing in classical novae: a multi-dimensional approach

Many one-dimensional nova simulations have been performed in the past and most of them are able to reproduce fairly well the gross observational properties of novae. In particular, these simulations can reasonably account for the abundances in the ejected material, the nucleosynthetic end-point, the shape of the light curve, the luminosity,... However, several aspects remain to be explained, as discussed in the previous sections. Perhaps, the most important ones are that current simulations cannot account for the amount of ejected mass inferred from observations and, moreover, they cannot provide a convincing explanation for the mixing mechanism at core-envelope interface. Actually, this is a common drawback of one-dimensional models, since these simulations cannot account for multi-dimensional effects (like convection and mixing). Consequently, multi-dimensional hydrodynamical calculations are required to address these issues and to shed more light on the unexplained features of classical nova explosions. Finally, it has to be taken into account that the abundances inferred from the ejected material are intimately related to the mixing processes on top of the white dwarf and to the precise time at which this mixing takes place.

To account for the gross observational properties of classical novae — in particular, a metallicity enhancement above solar values in the ejecta — numerical models assume mixing between the (solar-like) material transferred from the companion and the outermost layers (CO- or ONe-rich) of the underlying white dwarf. It is worth mentioning that one-dimensional simulations parameterize this mixing assuming that an arbitrary percentage of core material is injected into the envelope. Furthermore, these calculations also use the Mixing Lenght Theory (Böhm-Vitense, 1958) to represent the convective fluid motion, which clearly cannot account for the gross convective pattern. This is not a satisfactory procedure, and the nature of the mixing mechanism that operates at the core-envelope interface has puzzled stellar modelers for about 40 years, since the first one-dimensional nova simulation was performed (Sparks, 1969). In the past three decades, trying to shed light on the unkown mixing mechanism has been a priority for the astronomical community. Several mixing mechanisms have been proposed (Shore et al., 1994a):

1. Diffusive mixing. During the accretion phase, part of the accreted hydrogen can diffuse inwards and mix with the outermost white dwarf layers. Due to compression, these hydrogen-rich layers ignite and heavy isotopes from the core can be convectively transported (Prialnik & Kovetz, 1984; Kovetz & Prialnik, 1985; Fujimoto & Iben, 1992; Iben et al., 1991, 1992). The lower the accretion rate, the more mixing is found, since hydrogen can diffuse for a longer time. Thus, the metallicity enhancement seems to depend on the value adopted for the mass-accretion rate.

2. Shear mixing. Shear can be induced by differential rotation within the accretion disk in such a way that instabilities arise and generate convective motions, which would mix the material (Durisen, 1977; Kippenhahn & Thomas, 1978; MacDonald, 1983; Livio & Truran, 1987; Fujimoto, 1988; Sparks & Kutter, 1987; Kutter & Sparks, 1987, 1989). However, this mechanism does not seem to reproduce the observed mixing. Moreover, the simulations reported by Kut-

ter & Sparks (1987) and Sparks & Kutter (1987) did not result in any nova-like explosion for different mass-accretion rates.

More recently, another mixing mechanism related to shear has been proposed: an imposed wind profile on top of the white dwarf star would originate the formation of gravity waves on the surface. These translate into an effective mixing at the core-envelope interface when the imposed velocity is high enough (Rosner et al., 2001; Alexakis et al., 2002; Calder et al., 2002a; Alexakis et al., 2004a,b).

3. Convective overshoot. Numerical studies suggest that convective overshoot operating at the innermost layers of the accreted envelope would efficiently dredge-up material from the core and carry it into the envelope during the peak of the thermonuclear runaway (Woosley, 1986; Glasner & Livne, 1995; Glasner et al., 1997, 2007).

The contribution of fluid instabilities should also be taken into account as a potential seed for the CNO enhancement. The role of these instabilities deserves a special attention, since it is found that Kelvin-Helmholtz (Glasner & Livne, 1995; Glasner et al., 1997, 2007) and Rayleigh-Taylor instabilities (Shankar et al., 1992; Shankar & Arnett, 1994) may play an important role and actively take part in the onset of convection. It is worth mentioning that several mixing mechanisms may act during different stages of the nova process (during the accretion phase and/or during the thermonuclear runaway stage) and contribute to the overall metallicity enhancement. Multi-dimensional studies could naturally address these questions and shed light into the problem, since dimensionality will allow us to track the fluid motion and the implications derived from convection. The multi-dimensional nova simulation era started 20 years ago with the preliminary studies carried out by Shankar et al. (1992) and Shankar & Arnett (1994). Although their simulations were a rough approximation to the problem, they introduced the basis for the next generation of models mapping a one-dimensional model onto the grid of a code that could follow the evolution in two or three dimensions. This idea was further developed by Glasner & Livne (1995); Glasner et al. (1997, 2007) and Kercek et al. (1998, 1999). Up to date, only these two groups have performed multi-dimensional studies of mixing during classical nova explosions. Whereas the first group (Glasner et al., 1997) found that mixing is basically produced during the outburst, with huge convective cells that efficiently dredge-up ^{12}C from the core, the second group (Kercek et al., 1998), did not find any effective mechanism operating at the core-envelope interface during the thermonuclear runaway and concluded that mixing has to take place much prior to the late stages of the outburst. Both studies used the same one-dimensional model as input, and it has been suggested that the reason for the different results obtained relies on a different choice of the boundary conditions, which are determined by the different type of codes used: Lagrangian versus Eulerian (Glasner et al., 2005).

The existing controversy calls for additional multi-dimensional simulations to properly establish the link between fluid instabilities and mixing during classical nova explosions.

1.6 Outline of this thesis

The aim of this thesis is the multi-dimensional study of mixing at the core-envelope interface, describing as well how convection sets in and extends, and how the burning front starts and propagates. To carry out the calculations we have used the *FLASH* code, which is an Eulerian, parallelized multi-dimensional hydrodynamical code developed at the Flash Center of the University of Chicago. The *FLASH* code implements all the basic tools to model stellar explosions, such as classical novae.

The structure of this thesis is as follows: in chapter 2, we present a two-dimensional simulation of mixing in CO classical novae. This is followed in chapter 3 by a sensitivity study, aimed at testing the possible influence of the initial perturbation (duration, strength, location, and size), the resolution adopted, or the size of the computational domain on the results. In chapter 4, we present the first three-dimensional simulation of mixing up to date. Through these chapters, we also investigate the feasibility of Kelvin-Helmholtz instabilities as a natural mechanism for self-enrichment of the accreted envelope with core material, and the interplay between turbulence and the inhomogeneous abundance distribution observed in the ejecta. Movies of the different multi-dimensional simulations are provided in the attached CD-ROM and briefly described in appendix D. The main conclusions of this thesis and their physical implications are summarized in chapter 5, where we also provide some guidelines for future work. A detailed description of the *FLASH* code is presented in appendix A. This is complemented by a suite of hydrodynamical tests aimed at validating the code (appendix B), and a description of procedure for mapping the initial one-dimensional model onto the multi-dimensional grid of Godunov-like schemes (appendix C). Finally, in appendix E we outline the time requirements of simulations presented in this thesis, which were performed at the MareNostrum super-computer of the Barcelona Supercomputing Center.

Chapter 2

Mixing at the core-envelope interface in nova outbursts

The assumption of spherical symmetry in classical nova models (and in general, in stellar explosions) excludes an entire sequence of events associated with the way that a thermonuclear runaway (hereafter, TNR) initiates (presumably as a point-like ignition) and propagates. The first study of localized TNRs on white dwarfs was carried out by Shara (1982) on the basis of semianalytical models. He suggested that heat transport was too inefficient to spread a localized TNR to the entire white dwarf surface, concluding that localized, *volcanic-like* TNRs were likely to occur. But his analysis, based only on radiative and conductive transport, ignored the major role played by convection on the lateral thermalization of a TNR.

The importance of multi-dimensional effects for TNRs in thin stellar shells was revisited by Fryxell & Woosley (1982). In the framework of nova outbursts, the authors concluded that the most likely scenario involves TNRs propagated by small-scale turbulence. On the basis of dimensional analysis and flame theory, the authors derived the velocity of the deflagration front spreading through the stellar surface, in the form $v_{\rm def} \sim (h_P v_{\rm conv}/\tau_{\rm burn})^{1/2}$, where h_P is the pressure scale height, $v_{\rm conv}$ the characteristic convective velocity, and $\tau_{\rm burn}$ the characteristic timescale for fuel burning. Typical values for nova outbursts yield $v_{\rm def} \sim 10^4$ cm s^{-1} (that is, the flame propagates halfway throughout the stellar surface in about ~ 1.3 days). Shear-driven mixing induced by accretion of matter possessing angular momentum was also investigated by Kutter & Sparks (1987), but their numerical simulations failed to obtain a strong enough TNR to power a nova outburst — see Sparks & Kutter (1987).

The first multi-dimensional hydrodynamic calculations of this process were performed by Shankar et al. (1992) and Shankar & Arnett (1994). They evolved an accreting, $1.25\,M_\odot$ white dwarf with a 1-D hydro code that was mapped into a 2-D domain (a spherical-polar grid of 25×60 km). The explosive event was then followed with a 2-D version of the Eulerian code *PROMETHEUS*. A 12-isotope network, ranging from ^{1}H to ^{17}F, was included to treat the energetics of the explosion. Unfortunately, the subsonic nature of the problem, coupled with the use of an explicit code (with a timestep limited by the Courant-Friedrichs-Levy condition), posed severe limitations on the study, which had to be restricted to very extreme (rare) cases, characterized by huge temperature perturbations of about $\sim 100 - 600\%$, in small regions at the base of the envelope. The total computed time was only about 1 second. The calculations revealed that instantaneous, local temperature fluctuations cause Rayleigh-Taylor instabilities. Their rapid rise and subsequent expansion (in a dynamical timescale) cools the hot material and halts the lateral spread of the burning front, suggesting that such local temperature fluctuations are not important in the initiation or early stages of the TNR. The study, therefore, favored the local volcanic-like TNRs proposed by Shara (1982).

Glasner & Livne (1995) and Glasner et al. (1997) revisited these early attempts using 2-D simulations performed with the code *VULCAN*, an arbitrarily Lagrangian Eulerian (ALE) hydrocode capable of handling both explicit and implicit steps. As in Shankar et al. (1992), a slice of the star ($0.1\ \pi^{\rm rad}$), in spherical-polar coordinates with reflecting boundary conditions, was adopted. The resolution near the envelope base was around 5×5 km. As before, the evolution of an accreting, $1\,M_\odot$ CO white dwarf was initially followed using a 1-D hydro code (to overcome the early, computationally challenging phases of the TNR), and then mapped into a 2-D domain as soon as the temperature at the envelope base reached $T_{\rm b} \sim 10^8$ K. As in the previous works, the 2-D runs relied on a 12-isotope network. The simulations showed a good agreement with the gross picture described by 1-D models (for instance, the critical role played by the β^+-unstable nuclei ^{13}N, ^{14,15}O, and ^{17}F, in the ejection stage, and consequently, the presence of large amounts of ^{13}C, ^{15}N, and ^{17}O in the ejecta). However, some remarkable differences were also identified. The TNR was initiated by an ensemble of irregular, localized eruptions at the envelope base caused by buoyancy-driven temperature fluctuations indicating that combustion proceeds in a host of many localized flames — not as a thin front — each surviving only a few seconds. Nevertheless, these authors concluded that turbulent diffusion efficiently dissipates any local burning around the core, so the fast stages of the TNR cannot be localized and the runaway must spread through the entire envelope. In contrast to 1-D models, the core-envelope interface was convectively unstable, providing a source for the metallicity enhancement of the envelope by means of a Kelvin-Helmholtz instability — resembling the convective overshooting proposed by Woosley (1986). Efficient dredge-up of CO material from the outermost white dwarf layers accounts for $\sim 30\%$ metal enrichment of the envelope (the accreted envelope was assumed to be solar-like, without any pre-enrichment), in agreement with the inferred metallicites in the ejecta from CO novae (Gehrz et al., 1998). Finally, larger convective eddies were observed, extending up to 2/3 of the envelope height with typical velocities $v_{\rm conv} \sim 10^7$ cm s^{-1}. Despite these differences, however, the expansion and progress of the TNR towards the outer envelope quickly became almost spherically symmetric, although the initial burning process was not.

The results of another set of 2-D simulations were published shortly afterward by Kercek et al. (1998), which aimed to confirm the general behaviors reported by Glasner et al. (1997), in this case with a version of the Eulerian *PROMETHEUS* code. A similar domain (a box of about 1800×1100 km) was adopted, but using a cartesian, plane-parallel geometry to allow the use of periodic boundary conditions. Two resolution simulations were performed, one with a coarser 5×5 km grid as in Glasner et al. (1997), and a second with a finer 1×1 km grid. The calculations used the same initial model as Glasner et al. (1997), and produced qualitatively similar but somewhat less violent outbursts. In particular, they obtained longer TNRs with lower $T_{\rm peak}$ and $v_{\rm ejec}$, caused by large differences in the convective flow patterns. Whereas Glasner et al. (1997) found that a few, large convective eddies dominated the flow, most of the early TNR was now governed by small, very stable eddies (with $l_{\rm max} \sim$ 200 km), which led to more limited dredge-up and mixing episodes. The authors attributed these discrepancies to the different geometry and, more significantly, to the boundary conditions adopted in both simulations.

The only 3-D nova simulation to date was performed by Kercek et al. (1999), adopting a computational domain of 1800×1800×1000 km with a resolution of 8×8×8 km. It produced flow patterns that were dramatically different from those found in the 2-D simulations (much more erratic in the 3-D case), including mixing by turbulent motions occurring on very small scales (not fully resolved with the adopted resolution) and peak temperatures being achieved that were slightly lower than in the 2-D case (a consequence of the slower and more limited dredge-up of core material). The envelope attained a maximum velocity that was a factor $\sim$ 100 smaller than the escape velocity and, presumably, no mass ejection (except for a possible wind mass-loss phase). In view of these results, the authors concluded that CO mixing must take place prior to the TNR, in contrast to the main results of Glasner et al. (1997)[1].

In summary, two independent studies, that of Glasner et al. (1997) and that of Kercek et al. (1998), based upon the same 1-D initial model, reached nearly opposite conclusions about the strength of the runaway and its capability to power a fast nova. The origin of these differences was carefully analyzed by Glasner et al. (2005), who concluded that the early stages of the explosion, prior to the onset of the TNR — when the evolution is almost quasi-static — are extremely sensitive to the outer boundary conditions — see, e.g., Glasner et al. (2007), for a 2-D nova simulation initiated when the temperature at the envelope base is only 5×10^7 K). Several outer

---

[1] Other multi-dimensional studies (Rosner et al., 2001; Alexakis et al., 2004a,b) focused on the role of shear instabilities in the stratified fluids that form nova envelopes. They concluded that mixing can result from the resonant interaction between large-scale shear flows in the accreted envelope and gravity waves at the interface between the envelope and the underlying white dwarf. However, to account for significant mixing, a very high shear (with a specific velocity profile) had to be assumed.

boundary conditions were examined. The study showed that Lagrangian simulations, where the envelope is allowed to expand and mass is conserved, are consistent with spherically symmetric solutions. In contrast, in Eulerian schemes with a "free outflow" outer boundary condition — the choice adopted in Kercek et al. (1998) — the outburst can be artificially quenched.

In light of these conundrums, a reanalysis of the role of late mixing at the core-envelope interface during nova outbursts seems mandatory. To this end, we performed an independent 2-D simulation, identical to Glasner et al. (1997) and Kercek et al. (1998), with another multi-dimensional hydrodynamic code to investigate whether mixing can occur in an Eulerian framework with an appropriate choice of the outer boundary conditions.

2.1 Models and input physics

The 2-D simulation reported in this chapter used *FLASH*, a parallelized, hydrodynamical, Eulerian code based on the piecewise parabolic interpolation of physical quantities for solving the hydrodynamical equations and with an adaptive mesh refinement procedure. *FLASH* also uses a monotonicity constraint (rather than artificial viscosity) to control oscillations near discontinuities, a feature shared with the *MUSCL* scheme of van Leer (1979). For consistency with Glasner et al. (1997) and Kercek et al. (1998), the same initial model was used. The model was computed by Glasner et al. (1997) on the basis of a 1-D, implicit hydro code, assuming accretion of solar composition matter ($Z = 0.02$) onto the surface of a $1\,M_\odot$ CO white dwarf at a rate of $5 \times 10^{-9}\,M_\odot\,\mathrm{yr}^{-1}$. The accumulation of matter in degenerate conditions drives a temperature increase in the envelope, resulting in a superadiabatic temperature gradient and eventually convective transport. The initial model corresponds to the time when the temperature at the innermost envelope zone is $\approx 10^8$ K. At this stage, the mass of the accreted envelope reaches $2 \times 10^{-5}\,M_\odot$. This radial profile has been mapped onto a 2-D cartesian grid of 800×800 km and is initially relaxed to guarantee hydrostatic equilibrium. The initial computational grid comprises 112 radial layers (including the outermost part of the CO core) and 512 lateral layers. Calculations rely on the adaptive mesh refinement with a minimum resolution 1.6×1.6 km (simulations with a finer resolution will be presented in chapter 3).

A reduced nuclear reaction network was used to compute the energetics of the explosion: it consists of 13 isotopes (^{1}H, ^{4}He, ^{12,13}C, ^{13,14,15}N, ^{14,15,16,17}O, and ^{17}F — as in Glasner et al. (1997) and Kercek et al. (1998) — supplemented with ^{18}F to include the important ^{17}O(p, γ)^{18}F reaction), linked through a net of 18 nuclear processes (mainly, p-captures and β^+-decays). Reaction rates are taken from Angulo et al. (1999) and some more recent updates — see José et al. (2006), and references therein.

Periodic boundary conditions were adopted at both lateral sides, while hydrostatic boundary conditions are fixed at both the bottom (reflecting) and the top (outflow).[2] The set of boundary conditions are similar to those implemented in Glasner et al. (1997) and Kercek et al. (1998), but note that the outer computational grid adopted in Glasner et al. (1997) is Lagrangian instead of Eulerian (to follow the late expansion stages of the TNR). Finally, energy transport is included using an effective thermal diffusion coefficient that includes radiative and conductive opacities (Timmes, 2000).

2.2 Results

In Glasner et al. (1997), significant numerical noise was present at the onset of their calculations that produced temperature fluctuations of about 10–20%. We introduced (just at the initial time-step) a Gaussian temperature perturbation at the core-envelope interface of 5%. For comparison, the value in Kercek et al. (1998) was 1%. The size of the initial perturbation was 2 km, much smaller than the contemporary depth of the accreted envelope ($\sim$ 800 km). The initial perturbation produces fluctuations that move along the core-envelope interface during the first seconds of the simulations. These fluctuations, in turn, spawn Kelvin-Helmholtz vortices, which clearly show up about 200 s later (Fig. 2.1), and appear to initiate a turbulent cascade. Filaments and buoyant plumes are fully resolved in these simulations. At this stage, the fluid is characterized by a large Reynolds number, with a characteristic eddy length of 50 km, fluid velocities of $10^5 - 10^6$ cm s^{-1}, and a dynamic viscosity of 10^4 P. These Kelvin-Helmholtz instabilities transport unburnt CO-rich material from the outmost layers of the white dwarf core and inject it into the envelope. The characteristic eddy turnover time is $l_{\rm conv}/{\rm v}_{\rm conv} \sim 10$ s.

As the Kelvin-Helmholtz vortices grow in size, more CO-rich material is transferred into the envelope. Convection becomes more turbulent. The initially small convective eddies merge into huge shells (Fig. 2.2), as seen also in Glasner et al. (1997). At this stage, the nuclear energy generation rate reaches 10^{15} erg g^{-1} s^{-1}, while the characteristic burning timescale decreases to $\sim$5 s — Fig. 2.3. The convective filaments continue growing in size and progressively occupy the whole envelope length. Although not resolved in these simulations, and in contrast to the 3-D case, the conservation of vorticity in 2-D forces the largest eddies to grow in an inverse vorticity cascade, while energy flows to the viscous scale with a distribution that deviates from the Kolmogorov spectrum — see, e.g., Lesieur et al. (2001), and Shore (2007). At this time, the temperature at the envelope base reaches $\sim 2 \times 10^8$ K, at fluid velocities of 10^8 cm s^{-1} (of the order of the escape velocity, characteristic of the dynamic phases of the explosion), and a nuclear energy generation rate of 10^{16} erg $^{-1}$ s^{-1} — see Fig. 2.3. The convective turnover time is now $\sim$ 5 s. The

---

[2] Technical details of how boundary conditions are implemented in Godunov-type codes can be found in Zingale et al. (2002).

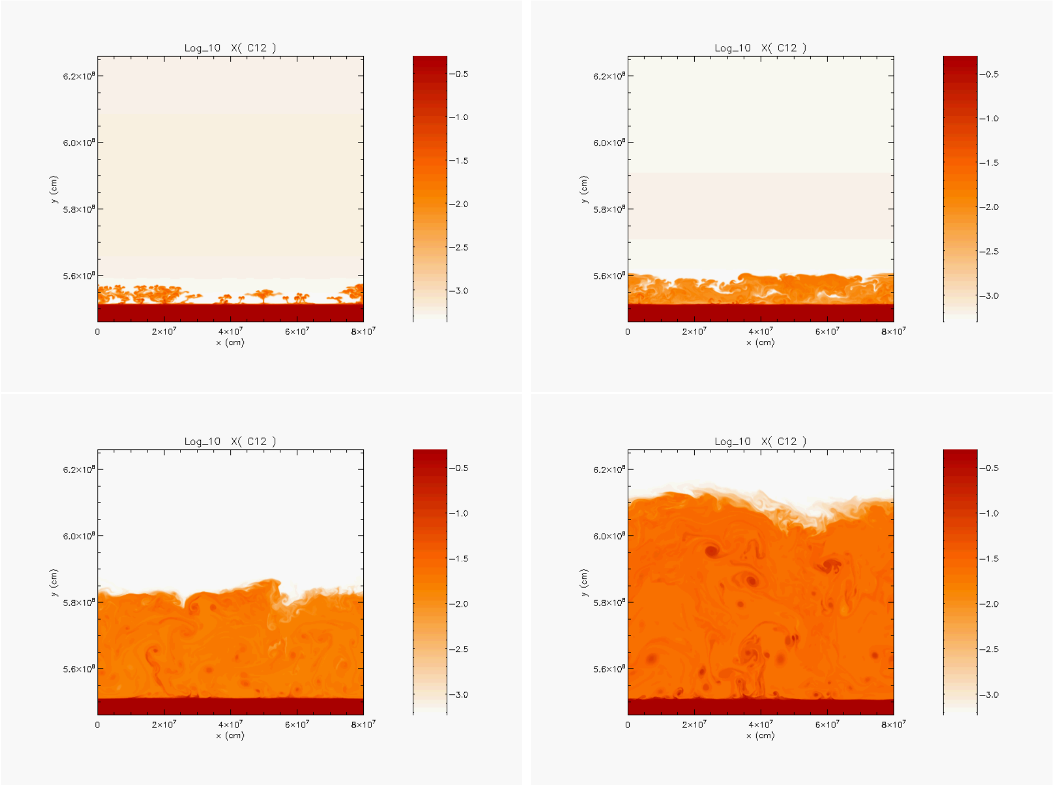

Figure 2.1: Snapshots of the development of Kelvin-Helmholtz instabilities at t = 215 s (upper left panel), 235 s (upper right), 279 s (lower left), and 498 s (lower right), shown in terms of ^{12}C mass fraction (in logarithmic scale). The injection of core material driven by the Kelvin-Helmholtz instabilities translates into a mass-averaged abundance of CNO-nuclei in the envelope of 0.079, 0.082, 0.089, and 0.17, respectively. The mean CNO abundance at the end of the simulations reaches 0.20, by mass.

mean CNO abundance in the envelope has increased to 0.20, a value that agrees well with both the previous simulations by Glasner et al. (1997) and the mean metallicities inferred from observations of the ejecta in non-neon (CO) novae — see José & Shore (2008). At this stage, since the outer envelope layers had started to escape the computational (Eulerian) domain, simulations were stopped.

Our 2-D simulations, in agreement with the results reported in Glasner et al. (1997), show that the progress and extension of the TNR throughout the envelope occurs with almost spherical symmetry, even though the structure of the ignition is not. This explains the success of 1-D models in reproducing the gross observational properties (light curves, velocities of the ejecta, nucleosynthesis) of nova explosions (Starrfield et al., 2009; Yaron et al., 2005; Starrfield et al., 1998; José & Hernanz, 1998; Kovetz & Prialnik, 1997).

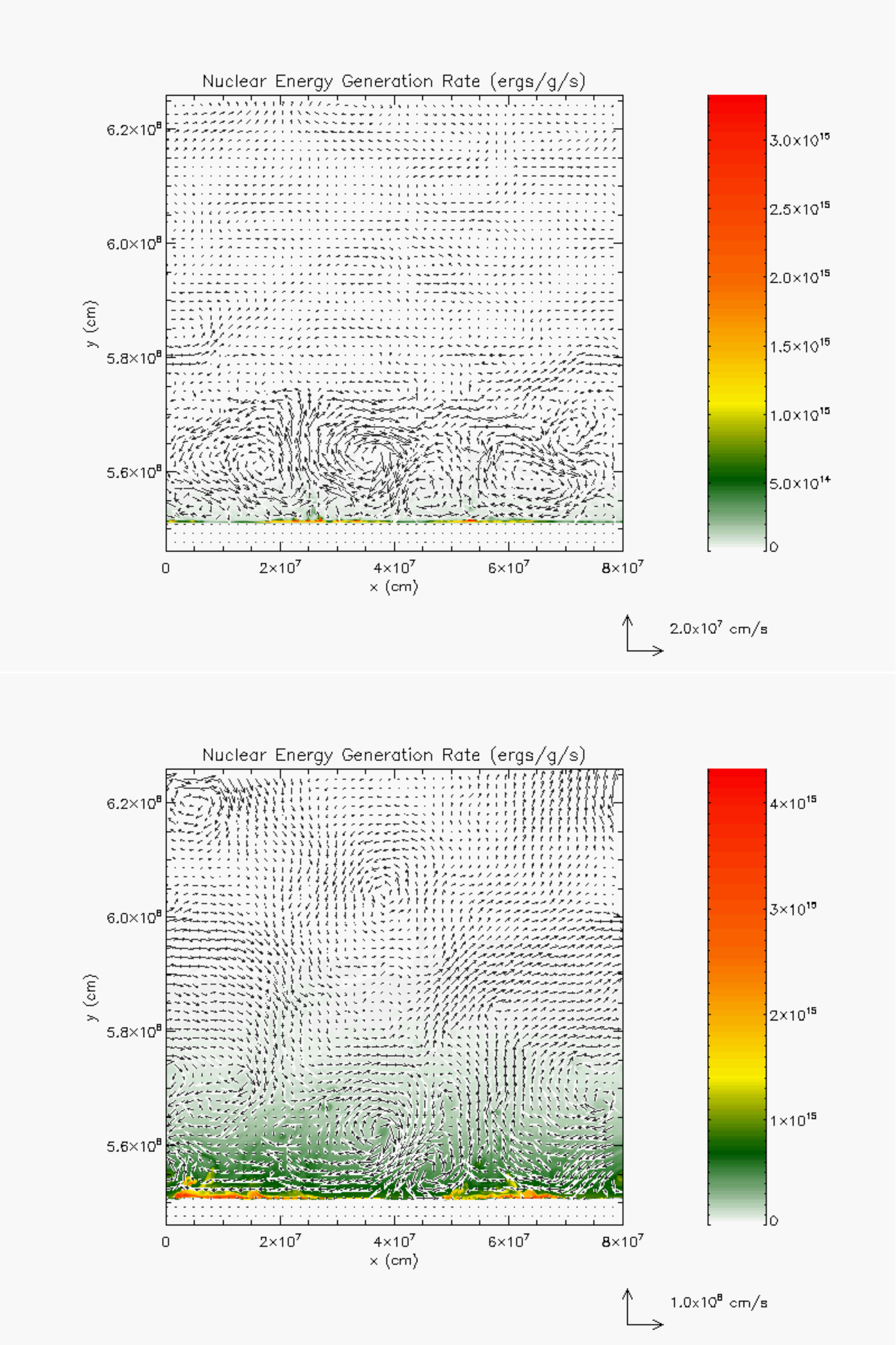

Figure 2.2: Same as Fig. 2.1, but for the velocity fields at $t = 279$ s (top) and 498 s (bottom), superimposed on a plot of the nuclear energy generation rate (in erg g^{-1} cm^{-1}).

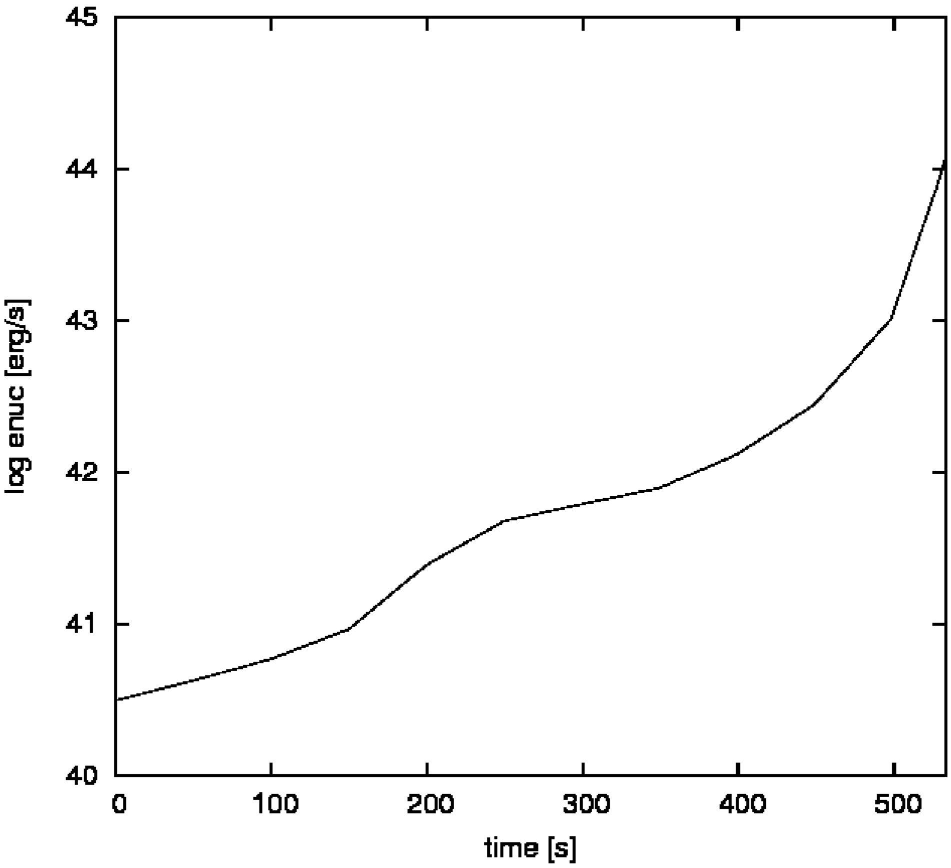

Figure 2.3: Time evolution of the overall nuclear burning rate.

2.3 Discussion and conclusions

We have analyzed the possible self-enrichment of the solar-composition accreted envelope with material from the underlying white dwarf during nova outbursts in a multi-dimensional framework. We have found that a shear flow at the core-envelope interface (which unlike the spherically symmetric case, does not behave like a rigid wall) drives mixing through Kelvin-Helmholtz instabilities. Large convective eddies develop close to the core-envelope interface, of a size comparable to the height of the envelope (similar to the pressure scale height in 1-D simulations), mixing CO-rich material from the outermost layers of the underlying white dwarf into the accreted envelope. The metallicity enrichment achieved in the envelope, $Z \sim 0.20$, is in agreement with observations of CO nova ejecta. Our 2-D simulations also show that even for a point-like TNR ignition, the expansion and progress of the runaway is almost spherically symmetric for nova conditions. We note that the adopted resolution as well as the size, intensity, and location of the initial perturbation have a very limited impact on the results, principally affecting the timescale for the onset of the Kelvin-Helmholtz instability but not the final, mean metallicity. Details will be extensively discussed in chapter 3. Our results agree with earlier 2-D hydrodynamic simulations (Glasner et al., 1997) and solve the controversy raised by another 2-D study (Kercek et al., 1998) that questioned the efficiency of this mixing mechanism, and hence the corresponding strength of the runaway and its capability to power a fast nova outburst.

Chapter 3

Mixing in classical novae: a 2-D sensitivity study

Classical novae are cataclysmic stellar events. Their thermonuclear origin, theorized by Schatzman (1949, 1951) and Cameron (1959) — see also Gurevitch & Lebedinsky (1957) and references therein — has been established through multiwavelength observations and numerical simulations pioneered by Sparks (1969), who performed the first 1-D, hydrodynamic nova simulation. These efforts helped to establish a basic picture, usually referred to as the *thermonuclear runaway* model (TNR), which has been successful in reproducing the gross observational properties of novae, namely the peak luminosities achieved, the abundance pattern, and the overall duration of the event; see Starrfield et al. (2008) and José & Hernanz (2007b) for recent reviews.

Many details of the dynamics of nova explosions remain to be explored. In particular, there are many observed cases of nonspherical ejecta, inferred from line profiles during the early stages of the outburst and from imaging of the resolved ejecta, including multiple shells, emission knots, and chemical inhomogeneities. Although the broad phenomenology of the outburst can be captured by 1-D calculations, it is increasingly clear that the full description requires a multi-dimensional hydrodynamical simulation of such outbursts. To match the energetics, peak luminosities, and the abundance pattern, models of these explosions require mixing of the material accreted from the low-mass stellar companion with the outer layers of the underlying white dwarf. In fact, because of the moderate temperatures achieved during the TNR, a very limited production of elements beyond those from the CNO-cycle is expected (Starrfield et al., 1998, 2009; José & Hernanz, 1998; Kovetz & Prialnik, 1997; Yaron et al., 2005), and the specific chemical abundances derived from observations (with a suite of elements ranging from H to Ca) cannot be explained by thermonuclear processing of solar-like material. Mixing at the core-envelope interface represents a likely mechanism.

The details of the mixing episodes by which the envelope is enriched in metals have challenged theoreticians for nearly 40 years. Several mechanisms have been proposed, including diffusion-induced mixing (Prialnik & Kovetz, 1984; Kovetz & Prialnik, 1985; Iben et al., 1991, 1992; Fujimoto & Iben, 1992), shear mixing at the disk-envelope interface (Durisen, 1977; Kippenhahn & Thomas, 1978; MacDonald, 1983; Livio & Truran, 1987; Kutter & Sparks, 1987; Sparks & Kutter, 1987), convective overshoot-induced flame propagation (Woosley, 1986), and mixing by gravity wave breaking on the white dwarf surface (Rosner et al., 2001; Alexakis et al., 2004a,b). The multi-dimensional nature of mixing has been addressed by Glasner & Livne (1995) and Glasner et al. (1997, 2005, 2007) with 2-D simulations of CO-novae performed with *VULCAN*, an arbitrarily Lagrangian Eulerian (ALE) hydrocode capable of handling both explicit and implicit steps. They report an effective mixing triggered by Kelvin-Helmholtz instabilities that produced metallicity enhancements to levels in agreement with observations. Similar studies — using the same initial model as Glasner et al. (1997) — were conducted by Kercek et al. (1998, 1999) in 2-D and 3-D, respectively. Their results, computed with the Eulerian code *PROMETHEUS*, displayed mild TNRs with lower peak temperatures and velocities than Glasner et al. (1997) and insufficient mixing. While Glasner et al. (1997) argue that substantial mixing can naturally occur close to peak temperature, when the envelope becomes fully convective and drives a powerful TNR, Kercek et al. (1998) conclude instead that mixing must take place much earlier: if it occurs around peak temperature, it leads to mild explosions or to events that do not resemble a nova.

The differences between these studies have been carefully analyzed by Glasner et al. (2005), who conclude that the early stages of the explosion, before TNR ignition when the evolution is quasi-static, are extremely sensitive to the adopted outer boundary conditions. They show that Lagrangian simulations, in which the envelope is allowed to expand and mass is conserved, lead to consistent explosions. In contrast, in Eulerian schemes with a "free outflow" outer boundary condition, the choice adopted in Kercek et al. (1998), the outburst can be artificially quenched. The scenario has been revisited in chapter 2 of this thesis and in Casanova et al. (2010), who show that simulations with an Eulerian scheme — the *FLASH* code — and a proper choice of the outer boundary conditions can produce deep-mixing of the solar-like accreted envelopes with core material. The puzzling results reported by Kercek et al. (1998) stress the need for a systematic evaluation of the effect that different choices of model parameters (e.g., the intensity and location of the initial temperature perturbation, resolution, or size of the computational domain) may have on the results. To this end, we performed a series of 9 numerical simulations in 2-D aimed at testing the influence of these parameters on the level of metal enhancement of the envelope. Here we report the results of these simulations.

This chapter is organized as follows. In section 3.1 we explain our input physics and initial conditions. Then section 3.2 is devoted to studying the mixing at the core-envelope interface for our fiducial model. In section 3.3 the effects of the size of the initial perturbation are analyzed, while in section 3.4 we discuss the effects of the size of the computational domain. In section 3.5 we quantify the influence of the grid resolution. Finally, in section 3.6 we discuss the significance of our results and draw our conclusions.

3.1 Input physics and initial conditions

The simulations reported in this chapter were performed with *FLASH*, a parallelized explicit Eulerian code, based on the piecewise parabolic interpolation of physical quantities for solving the hydrodynamical equations, and with adaptive mesh refinement — see Fryxell et al. (2000). As in chapter 2 — see also Casanova et al. (2010) — we used the same initial model as Glasner et al. (1997) and Kercek et al. (1998): a $1\,M_\odot$ CO white dwarf that accretes solar composition matter ($Z = 0.02$) at a rate of $5 \times 10^{-9}\,M_\odot\ \mathrm{yr}^{-1}$. The model was evolved spherically (1-D) and mapped onto a 2-D cartesian grid, when the temperature at the base of the envelope reached $\approx 10^8$ K. It initially comprised 112 radial layers — including the outermost part of the CO core — and 512 horizontal layers. The mass of the accreted envelope was about $2 \times 10^{-5}\,M_\odot$. Nuclear energy generation is handled through a network of 13 species (^{1}H, ^{4}He, ^{12,13}C, ^{13,14,15}N, ^{14,15,16,17}O, and ^{17,18}F), and connected through 18 nuclear reactions. We adopted the conductive and radiative opacities from Timmes (2000) and an equation of state based on Timmes & Swesty (2000). Periodic boundary conditions were imposed on both sides of the computational domain with vertical hydrostatic equilibrium with an outflow constraint at the top and a reflecting constraint at the bottom on the velocity — see Zingale et al. (2002). A summary of the main characteristics of the 9 models computed in this chapter is given in Table 3.1, where H is the distance from the perturbation to the initial core-envelope interface, R_x and R_y[1], δT, and δt are the size, strength, and duration of the temperature perturbation, and Z the mass-averaged metallicity of the envelope at the end of the calculations.

In this section, we describe the basic features of our fiducial model A, as a framework for further discussion of the effect of the parameter choices on our results. A movie, showing the development of Kelvin-Helmholtz instabilities, in terms of the ^{12}C content, up to the time when the convective front hits the upper computational boundary, is presented in appendix D (supplementary movie 2D_C12.wmv). The simulation was performed for the conditions of model A, as summarized in Table 3.1.

For all sequences reported in this chapter, the relaxation of the initial model to guarantee hydrostatic equilibrium, together with the small amount of numerical viscosity — in contrast with the simulations performed by Glasner et al. (1997) — requires an initial perturbation close to the core-envelope interface to trigger the onset of instabilities early in the calculations. The initial perturbation is applied

---

[1] The different values adopted for R_x and R_y in models F and G are used to account for the assumption of a rectangular (rather than square) computational domain.

Table 3.1: Models computed.

Model	H (km)	$R_x \times R_y$ (km)	δT	δt (s)	Resolution (km)	Computational Domain (km)	t_{KH} (s)	t_Y (s)	Z
A	0	1 × 1	5%	10^{-10}	1.56 × 1.56	800 × 800	155	496	0.224
B	0	1 × 1	5%	10	1.56 × 1.56	800 × 800	28	347	0.212
C	0	1 × 1	0.5%	10^{-10}	1.56 × 1.56	800 × 800	155	493	0.209
D	5	1 × 1	5%	10^{-10}	1.56 × 1.56	800 × 800	154	496	0.235
E	5	5 × 5	5%	10^{-10}	1.56 × 1.56	800 × 800	156	486	0.209
F	0	2 × 1	5%	10^{-10}	1.56 × 1.56	1600 × 800	151	493	0.206
G	0	1 × 1.25	5%	10^{-10}	1.56 × 1.56	800 × 1000	156	526	0.291
H	0	1 × 1	5%	10^{-10}	1 × 1	800 × 800	162	584	0.201
I	0	1 × 1	5%	10^{-10}	0.39 × 0.39	800 × 800	268	893	0.205

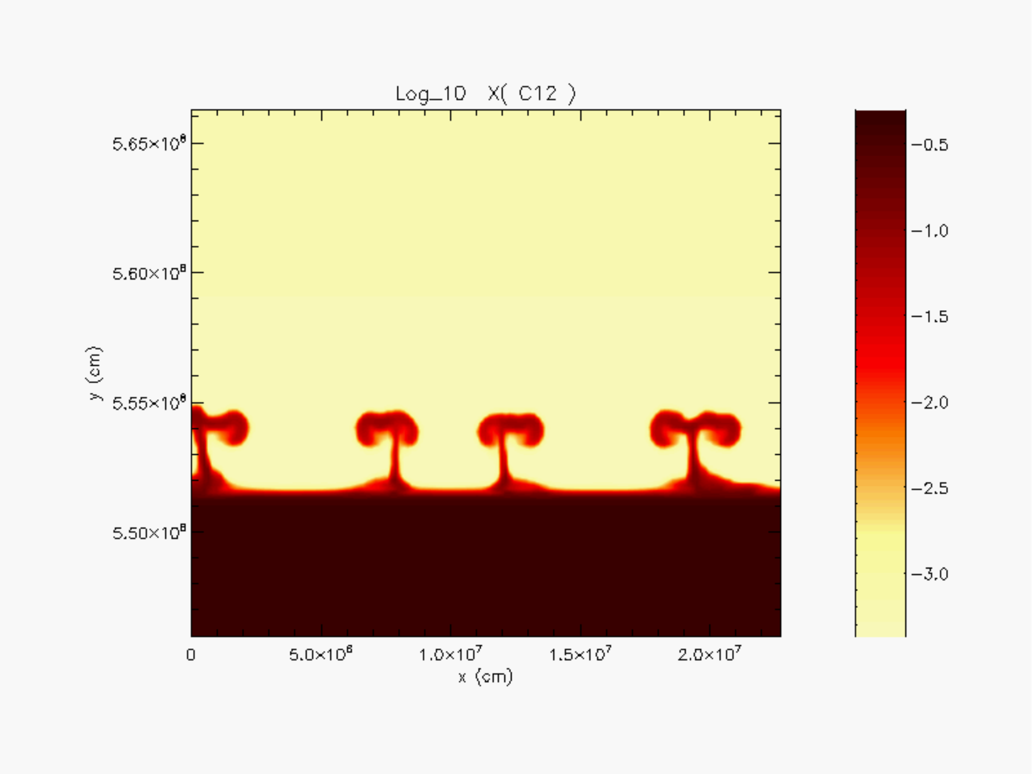

Figure 3.1: Snapshot of the development of early instabilities, which later spawn Kelvin-Helmholtz instabilities, shown in terms of the ^{12}C mass fraction (in logarithmic scale) for model A, 158 s from the start of the simulation when the core-envelope interface temperature is $T_{\rm base} \sim 1.36 \times 10^8$ K.

to the temperature using four parameters: strength, location, size and duration. Model A assumes a *top-hat* temperature perturbation wherever $((x - x_0)/R_x)^2 + ((y - y_0)/R_y)^2 \leq 1$, where x and y are the space coordinates measured from the center of the perturbation, $(x_0,\, y_0)$, and R_x and R_y indicate its spatial extent. We fixed $x_0 = 5 \times 10^7$ cm in all sequences. The strength of the perturbation is 5% in temperature in all cases but one (see table 3.1). It is 1 km wide, applied only during the initial timestep (that is, the temperature is fixed only during 10^{-10} s), and imposed on the core-envelope interface ($y_0 = 5.51 \times 10^8$ cm). The resolution adopted in model A is 1.56 × 1.56 km, and the size of the computational domain is 800 × 800 km.

3.2 2-D simulations of mixing at the core-envelope interface

The initial perturbation drives a shear flow that triggers the formation of instabilities (Fig. 3.1), about 150 s after the start of the simulation. As soon as material from the core is mixed into the envelope, small convective cells develop. At this early stage, the fluid has a large Reynolds number, with a characteristic eddy length of 50 km, fluid velocities ranging between $v = 10^5 - 10^6$ cm s^{-1}, and a dynamic viscosity[2] of 2×10^4 P. The fluid velocity v remains below the speed of sound c_s (that is, the Mach number Ma= v/c_s is always less than unity, see Fig. 3.2), hence, the fluid displays a deflagration rather than a detonation — see Williams (1985), for a thorough analysis of the differences between flame propagation under detonation and deflagration conditions. At $t = 235$ s, the characteristic eddy turnover time is $l_\mathrm{conv}/v_\mathrm{conv} \sim 10$ s. The merging of the small convective cells into large eddies, characteristic of 2-D simulations, with a size comparable to the height of the envelope, reinforces the injection of CO-rich material into the envelope. Convection becomes more turbulent. At this stage ($t = 450$ s), the nuclear energy generation rate exceeds 10^{15} erg g^{-1} s^{-1}, while the characteristic convective timescale decreases to ~ 5 s. The convection front propagates progressively upwards (Fig. 3.3, top panel), with a velocity of ~ 10 km/s, and eventually reaches the top of our computational domain. The envelope base reaches a peak temperature of 1.64×10^8 K. At this time ($t = 496$ s), when matter starts to cross the outer boundary of the computational domain, we stop the calculations because of the Eulerian nature of the *FLASH* code. At this final stage, the mean mass-averaged metallicity in the envelope reaches $Z \sim 0.22$. It is worth noting, however, that the convective eddies are still pumping metal-rich matter through the core-envelope interface. Hence, it is likely that the final metallicity in the envelope will be larger. The simulation shows that the induced Kelvin-Helmholtz vortices can naturally lead to self-enrichment of the accreted envelope with core material to levels that agree with observations and that the expansion and progress of the runaway is almost spherically symmetric for nova conditions even for a point-like TNR ignition.

3.3 Effect of the initial perturbation

To quantify the influence of the initial perturbation on our results, we have performed a series of 2-D hydrodynamic tests for a set of different durations, strengths (intensities), locations and sizes of the perturbation. For simplicity, a top-hat perturbation, centered at $x_0 = 5 \times 10^7$ cm, has been adopted in all models reported in

---

[2] The dynamic viscosity evaluates the resistance to flow of a fluid under an applied force. More precisely, it is defined as the tangential force per unit area required to move one horizontal plane with respect to the other at unit velocity when maintaining a unit distance apart by the fluid.

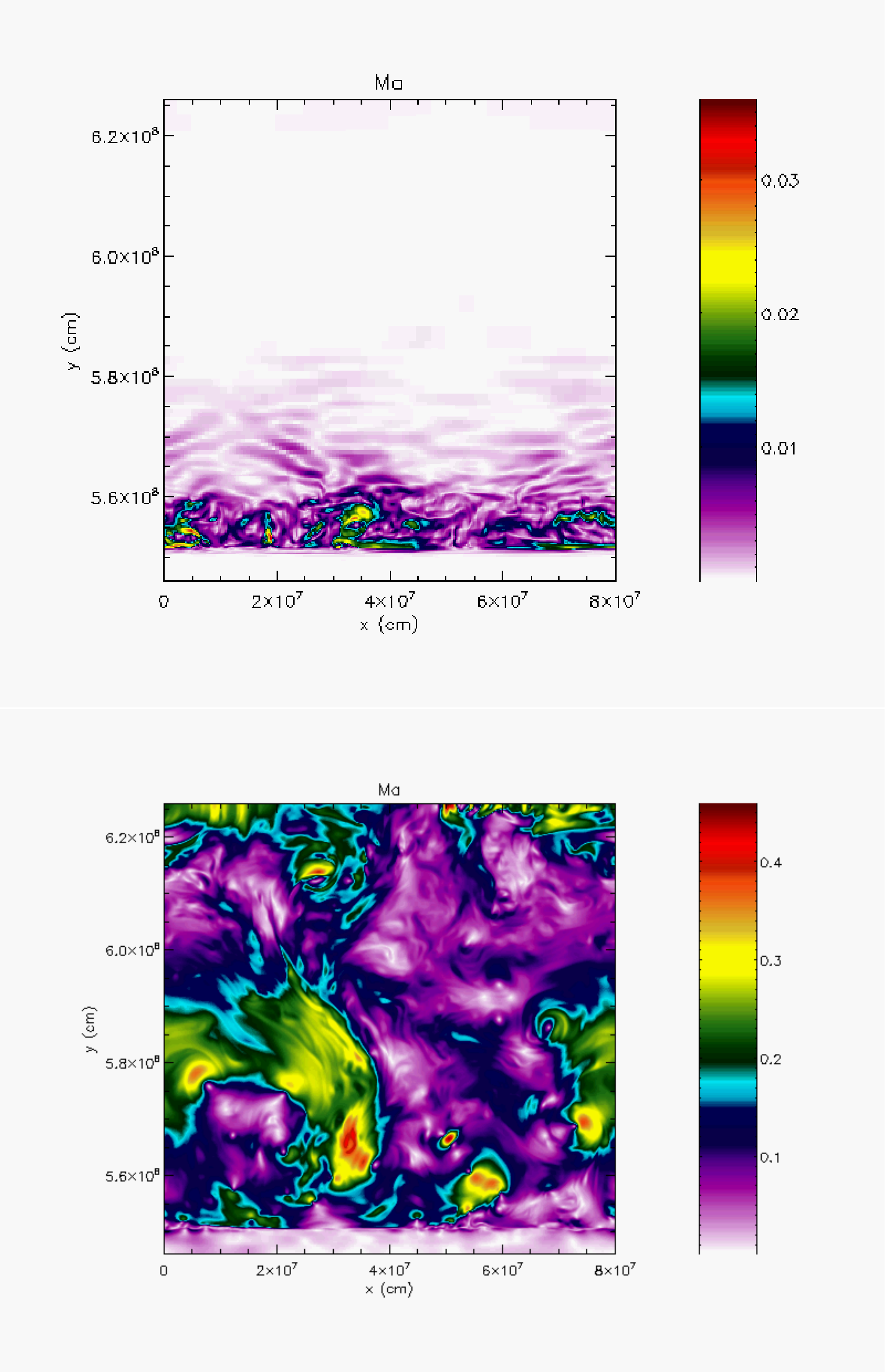

Figure 3.2: Mach number at two different moments of the simulation, $t = 230$ s (top panel) and 496 s (bottom panel), for model A.

this chapter.

The effect of the duration of the perturbation was checked by means of a test case (model B), identical to model A but with a perturbation lasting for 10 s. As shown in Table 3.1, the characteristic timescales for model B, such as the time required for the first instabilities to show up, $T_{\rm KH}$, or the time needed by the convective front to hit the outer boundary, t_Y, become shorter. The role played by a temperature perturbation can be understood in terms of the energy injected into the envelope: the longer the duration of the perturbation, the larger the energy injected, and thus, the shorter the characteristic timescales of the TNR. This has little effect, however, on the overall metallicity enhancement in the envelope since a final CNO mass fraction of ~ 0.212 was found in model B, whereas ~ 0.224 resulted in model A.

Both models A and B assumed temperature perturbations of $\delta T \sim 5\%$ during the initial timestep $\sim 10^{-10}$ s and 10 s, respectively. To test the possible influence of the strength of the perturbation, a test case with $\delta T \sim 0.5\%$ (model C) has also been computed. As shown in Table 3.1 and Fig. 3.4, the time evolution of models A and C is very similar, and hence, similar final mean CNO mass fractions at the end of the simulations were found (with $Z = 0.209$ in model C).

The effect of the location of the perturbation along the vertical axis has also been studied: whereas model A assumed a temperature perturbation of $\sim 5\%$, applied at the innermost envelope shell ($y_0 = 5.51 \times 10^8$ cm), in model D, a similar perturbation was placed ~ 5 km above the core-envelope interface ($y_0 = 5.515 \times 10^8$ cm). Both models exhibit a very similar temporal evolution, with almost identical times for the appearance of the first instabilities and for the time required to reach the outer boundary. Similar envelope mean CNO mass fractions (0.224 and 0.235, respectively) were also found.

Finally, the influence of the size of the perturbation has also been analyzed. Whereas model D was evolved with an initial temperature perturbation of size $R_x =$ 1 km and $R_y = 1$ km, model E assumed $R_x = 5$ km and $R_y = 5$ km. As before, very similar characteristic timescales (see Table 3.1) and final mean CNO mass fractions (0.235 and 0.209, respectively) were found.

To summarize, the specific choice of the parameters that define the initial temperature perturbation has a negligible effect on metallicity enhancement of the envelope.

3.4 Effect of the size of the computational domain

The choice of the computational domain represents a compromise between computational time requirements and numerical accuracy. Several considerations constrain its minimum size. On one hand, the merger of large convective eddies often found in 2-D simulations may be severely affected by the adoption of a small computational domain. On the other hand, nova outbursts eventually result in mass ejection. With an Eulerian code such as *FLASH*, it is not possible to track the material that flows

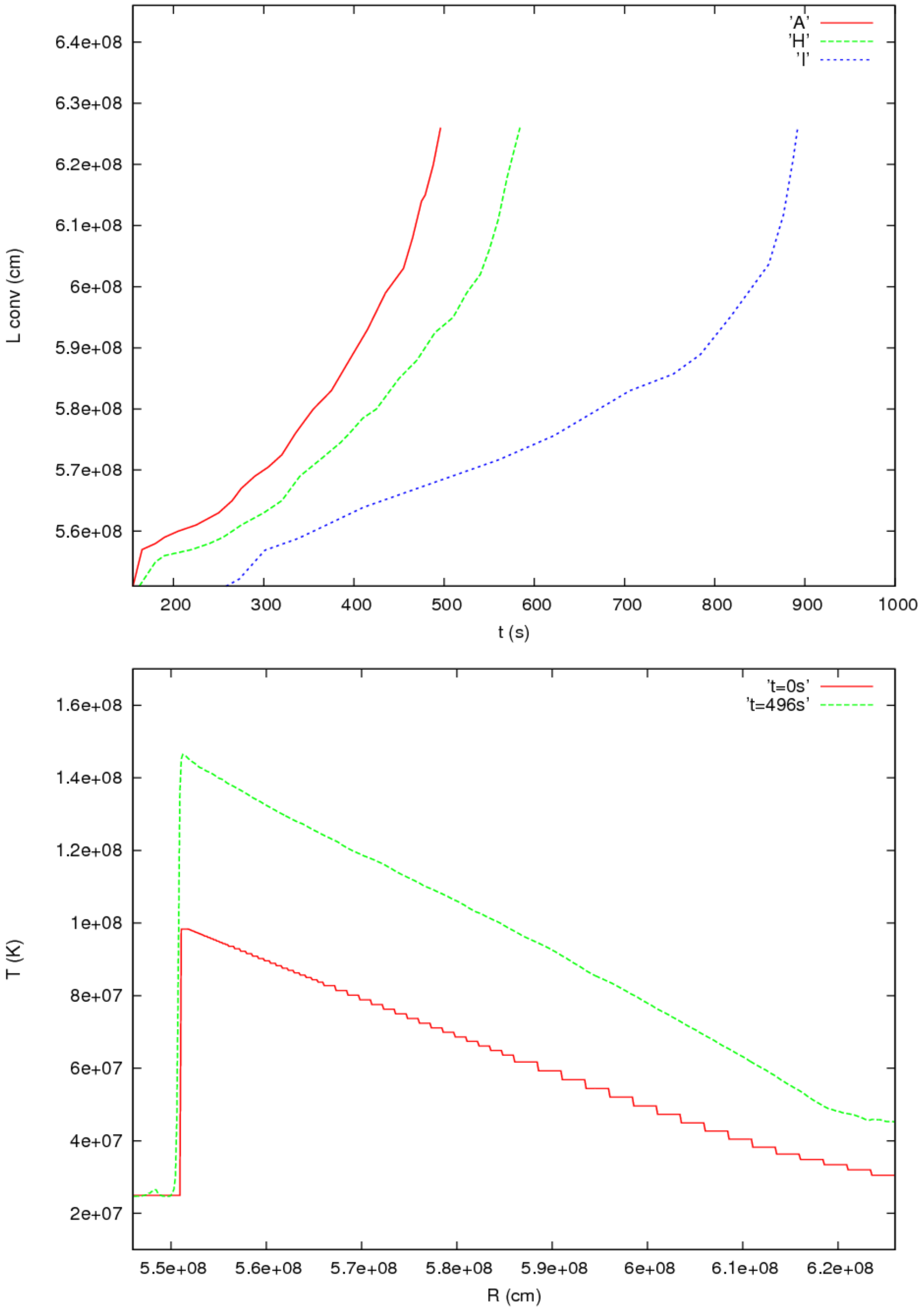

Figure 3.3: Top panel: propagation of the convective front as a function of time, for models A, H, and I. Bottom panel: temperature profile versus radius at two different times, $t = 0$ s (solid line; $T_{\rm base} = 9.84 \times 10^7$ K) and $t = 496$ s (dashed line; $T_{\rm base} = 1.64 \times 10^8$ K), for model A.

off the grid, and hence, it is important to use domains that are as large as possible along the radial direction (while being sufficiently wide along the horizontal axis). Unfortunately, when the initial 1-D model is mapped into the 2-D grid, and relaxed to guarantee hydrostatic equilibrium, densities quickly underflow values for large heights (Zingale et al., 2002).

The specific size adopted for most of the models computed in this chapter, i.e. 800×800 km, is a bit smaller than those used in Glasner et al. (1997) — $0.1\pi^{\mathrm{rad}}$, in spherical-polar coordinates — and in Kercek et al. (1998) — 1800×1100 km, in a cartesian, plane-parallel geometry. In this section, we analyze possible dependences of the results on the adopted size of the computational domain. To this end, two additional simulations were performed. In the first one (model F), a wider computational domain has been adopted (i.e., 1600×800 km). In the second (model G), aimed at testing the influence of the vertical (radial) length, a domain of 800×1000 km has been used (where the choice of 1000 km results from numerical restrictions that limit the vertical extent of our computational domain).

As shown in Table 3.1, the horizontal width (model F) has no noticeable effect on the timescales of the simulations, either for the time required for the onset of the first instabilities or for the time required for the convective front to reach the outer boundary. The mass-averaged CNO abundance in the envelope reached ~ 0.206 at the end of this simulation, close to the value found for model A. These results confirm that 800 km is an appropriate choice for the width of the computational domain, stressing that above a threshold value the course of the TNR is insensitive to the adopted width, in agreement with the sensitivity study performed by Glasner et al. (2007).

The specific length adopted along the vertical direction (see model G), while unimportant for the time of appearance of the instabilities (around 155 s after the start of the simulation, as in model A), affects the time required to reach the outer boundary, located 200 km above the value adopted for model A. Moreover, the larger extension of the computational domain along the radial (vertical) direction allows the convective eddies to pump additional metal-rich core material into the envelope compared with all the simulations reported previously in this paper. Indeed, the mean, mass-averaged metallicity in model G achieves the largest value of all the simulations reported, ~ 0.291. This result suggests that the likely mean mass-averaged metallicity driven by Kelvin-Helmholtz instabilities should be $Z \approx 0.3$. In summary, we conclude that the size of the computational domain, above a certain threshold value, has little influence on the physical quantities that are more directly related with the mixing process at the core-envelope interface.

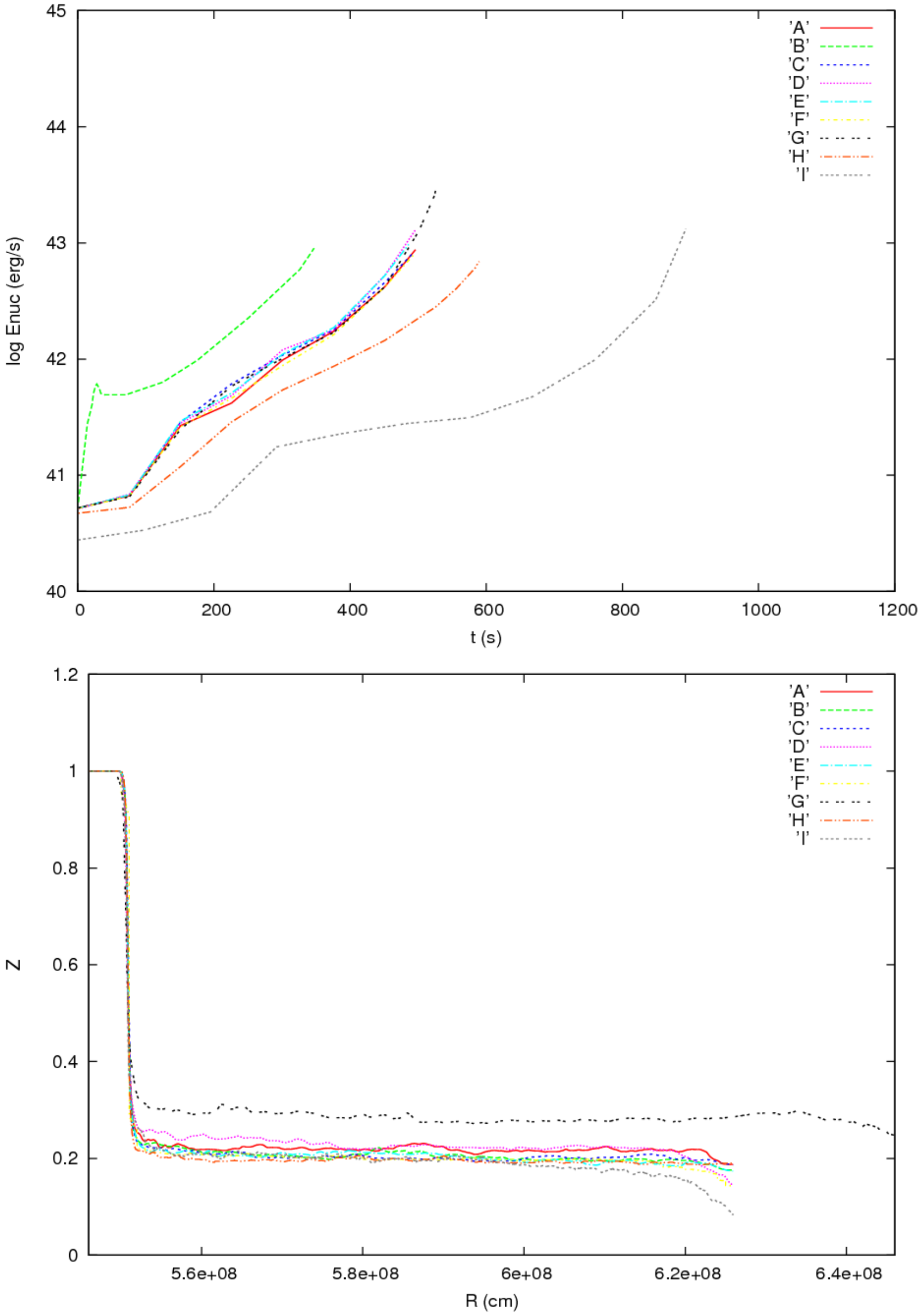

Figure 3.4: Top panel: time evolution of the nuclear energy generation rate (in erg s^{-1}) for the 9 models computed in this chapter. Bottom panel: final CNO mass fraction versus radius.

3.5 Effect of the grid resolution

All simulations discussed so far (e.g., models A to G) were performed with a resolution of 1.56×1.56 km, a value similar to the minimum resolutions adopted in Glasner et al. (1997) which is roughly $\sim 1.4 \times 1.4$ km, and in Kercek et al. (1998), 1×2 km. To quantitatively assess the possible effect of the resolution, two additional test cases were computed with exactly the same input parameters as in model A but with two different resolutions: 1×1 km (model H) and 0.39×0.39 km (model I)[3].

As shown in Table 3.1, the increase in resolution produces a delay in the time required for the first instabilities to develop, $t_{\rm KH}$. This seems to be a numerical artifact. In models with a coarser resolution, the larger size of the blocks artificially generates a larger numerical diffusion compared to models with a finer resolution — a similar resolution dependence is clearly seen as well in the Kercek et al. (1998) simulations. Actually, the ratio of differences in the initial build up times — i.e., (model I-model A)/(model H-model A) — scales approximately as the zone size dimensions to the power of two. This is a purely numerical perturbation that forces the development of instabilities. To test this hypothesis, we computed an additional test case (not included in Table 3.1), identical to model A but without any initial perturbation. The onset of the instabilities in such an extremely low numerical diffusion regime is substantially delayed. The simulations reported by Glasner et al. (1997) also show the early appearance of instabilities in a model with substantial numerical noise: *within a very short time (about 10 s), the numerical noise (round-off) seeds an intense convective flow in the envelope without any artificial perturbations.*

A similar behavior is also found for the time required for the convective front to reach the outer boundary, t_Y, and for the history of the nuclear energy generation rate (Fig. 3.4). As expected, filamentary structures and convective cells are better resolved in the finer resolution model I, compared to those computed with somewhat coarser grids (models A and H; see Fig. 3.5). These minor differences do not, however, show significant variations in the final, mean CNO abundances achieved in the envelope: while $Z \sim 0.224$ in model A, models H and I yield 0.201 and 0.205, by mass, respectively. Similar agreement is found in the peak temperatures achieved and in the overall nuclear energy generation rates (Fig. 3.4).

Thus, the adopted resolution has not a critical effect for the mixing models presented in this chapter. The variation in the final mean CNO abundance in the envelope, under the range of resolutions adopted, is only about 12% (when comparing results for models A, H, and I), a quite reasonable value.

---

[3] For comparison, whereas a maximum number of 5300 blocks are administered in model A, the number of blocks increases up to 83000 in model I. The total CPU time spent in both simulations, using 256 processors of the MareNostrum supercomputer, has been 3 and 110 khr, respectively.

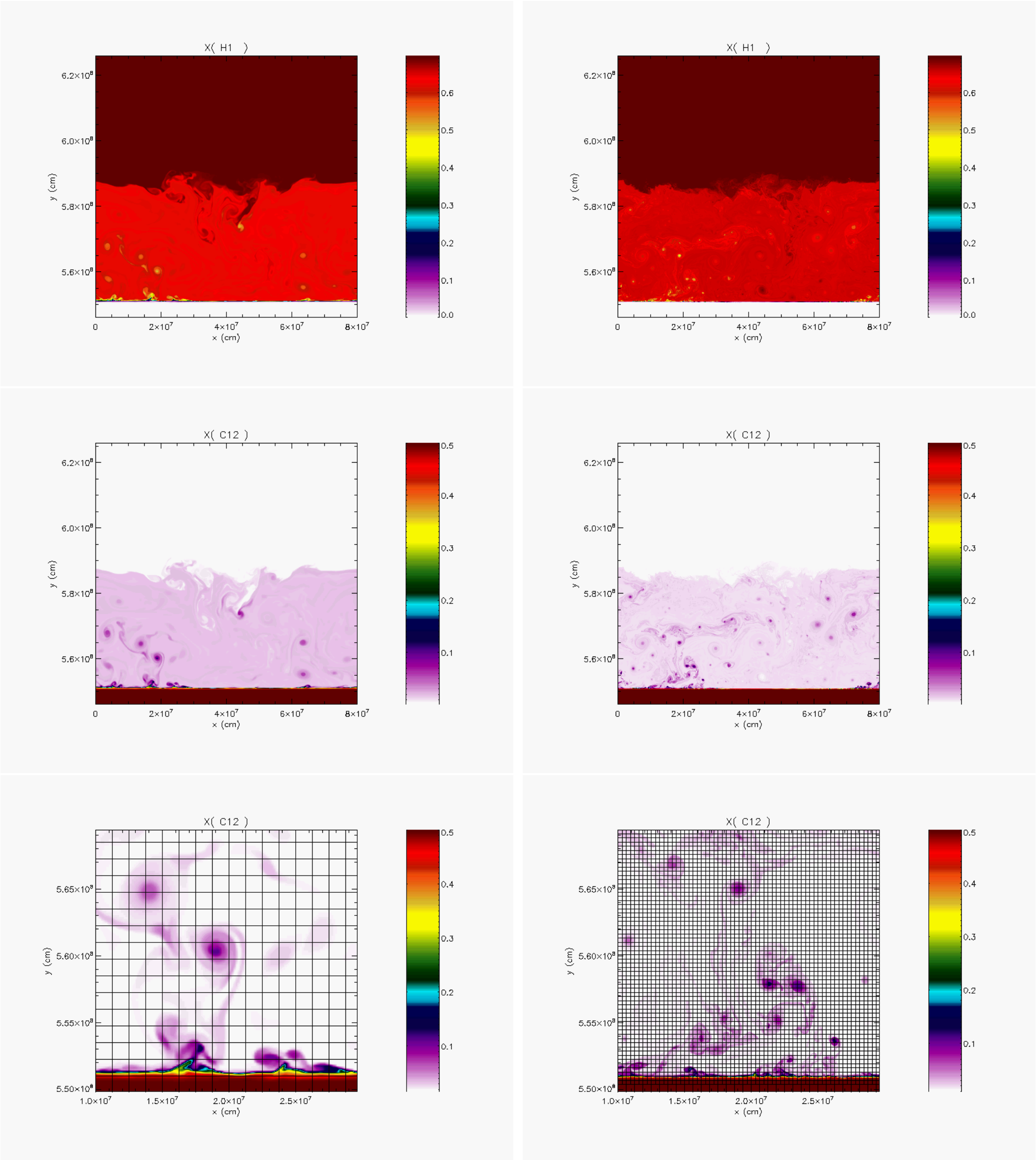

Figure 3.5: Snapshots of the ^{1}H (upper panels) and ^{12}C (middle panels) mass fractions at $t \sim 395$ s (model A; left panels), and 688 s (model I; right panels). Lower panels: the number of blocks administered, at this stage, is 3184 for model A, and 43800 for model I. In both simulations, *FLASH* divides each block in 8 cells. Structures such as vortexs are better resolved in the finer resolution model I.

3.6 Discussion and conclusions

In this chapter we have reported results for a series of nine 2-D numerical simulations that test the influence of the initial perturbation (duration, strength, location, and size), the resolution of the grid, and the size of the computational domain on the results. We have shown that mixing at the core-envelope interface proceeds almost independently of the specific choice of such initial parameters, above threshold values.

The study confirms that the metallicity enhancement inferred from observations of the ejecta of classical novae can be explained by Kelvin-Helmholtz instabilities, powered by an effective *mesoscopic* shearing resulting from the initial buoyancy. Fresh core material is efficiently transported from the outermost layers of the white dwarf core and mixed with the approximately solar composition material of the accreted envelope. As soon as ^{12}C and ^{16}O are dredged up, convection sets in and small convective cells appear, accompanied by an increased nuclear energy generation rate. The size of these convective cells increases in time. Eventually, these cells merge into large convective eddies with a size comparable to the envelope height. The range of mean mass-averaged envelope metallicities obtained in our simulations at the time when the convective front hits the outer boundary, $0.21 - 0.29$, matches the values obtained for classical novae hosting CO white dwarfs.

It is, however, worth noting that the convective pattern is actually produced by the adopted geometry (e.g., 2-D), forcing the fluid motion to behave very differently than 3-D convection (Shore, 2007; Meakin & Arnett, 2007). Nevertheless, the levels of metallicity enhancement found in our 2-D simulations will likely remain unaffected by the limitations imposed by the 2-D geometry (D. Arnett, private communication). Fully 3-D simulations aimed at testing this hypothesis are presented in chapter 4.

Chapter 4

Three-dimensional modeling of mixing in nova explosions

Classical novae (Bode & Evans, 2008; Hernanz & José, 2002) are stellar explosions with an energy release that is only surpassed by supernovae and γ-ray bursts. They eject $10^{-4} - 10^{-5}$ solar masses of nucleosynthetically enriched gas into the interstellar medium. These events are considered the main source (José et al., 2006; José & Hernanz, 2007b; Starrfield et al., 2008) of Galactic ^{15}N, ^{17}O, and ^{13}C, and contribute to the abundances of other species, such as ^{7}Li and ^{26}Al. However, the origin of the inhomogeneous distribution of these species, as observed in the ejecta, is not well-known (José & Shore, 2008) and has puzzled theoreticians for more than 40 yr. In this chapter, we present a three-dimensional (3-D) nuclear-hydrodynamic simulation of mixing at the core-envelope interface during nova outbursts. We show that Kelvin-Helmholtz instabilities lead to self-enrichment of the solar accreted envelopes with material from the outer white dwarf core, at the observed levels without artificial enhancements of the convective mixing length. The evolution proceeds through bursting plumes to a turbulent cascade that retains significant filamentary substructure. The simulations also naturally produce large scale chemical inhomogeneities and yield intrinsic dispersions in the abundances that are consistent with observations. The resulting structures may be the origin of the highly fragmented ejecta detected during many different nova outbursts.

4.1 The source of inhomogeneous mixing in nova explosions

Classical novae are stellar explosions produced on white dwarfs that accumulate gas transferred from a (usually) low-mass, K-M dwarf, main sequence star. Mass transfer episodes in these short period binaries (1–10 hr) result on the formation of an accretion disk surrounding the white dwarf. A fraction of this matter spirals in and ultimately accumulates on its surface (typically at rates $10^{-9} - 10^{-10}\,M_\odot$ yr^{-1}), piling up an envelope under degenerate conditions until a thermonuclear runaway ignites (José et al., 2006; José & Hernanz, 2007b; Starrfield et al., 2008). Unlike type Ia supernovae, nova outbursts are restricted to the outer layers and neither the star nor the binary system are destroyed by the explosion. Thus, classical novae are expected to recur on intervals $\sim 10^4 - 10^5$ yr.

The initiating stages of the outburst are governed by nuclear processes dominated by CNO-cycle reactions, resulting in the synthesis of large amounts of ^{13}N, ^{14,15}O and ^{17}F. The main nuclear path runs close to the valley of stability, driven by proton-captures and β^+-decays (José et al., 2006), with a likely end-point around Ca. Convection sets in as soon as the temperature gradient becomes super-adiabatic, powered by the energy released from nuclear reactions, and plays a critical role in the explosion, transferring a fraction of the abundant, short-lived species ^{13}N, ^{14,15}O and ^{17}F to the outer envelope layers. The energy released when these nuclei decay lifts degeneracy and drives the expansion, and ultimate ejection, of the polluted strata (Starrfield et al., 1972). The nuclear processes that occur during the different stages of a nova explosion leave a characteristic imprint in the ejecta, with non-solar isotopic abundance ratios. High-resolution spectra (Gehrz et al., 1998) of nova shells show that the ejecta is highly enriched in metals, with mass fractions ranging from Z $\sim$ 0.25 by mass, for CO novae, to 0.50, for ONe novae. Emission line profiles, and direct imaging during the free expansion stage, when spatially resolved, also show non-spherical ejecta even in the initial stages of the explosion. Multiple shells, emission knots, and chemical inhomogeneities are typical, yet their origin(s) remain unknown.

Because the peak temperatures reached during the explosion (as constrained by the chemical abundance pattern inferred from the ejecta) do not exceed 4×10^8 K, it is unlikely that the observed metallicity enhancements indicate thermonuclear processes driven by CNO-breakout. Instead, mixing at the core-envelope interface is the more likely explanation. Although several mixing mechanisms (Shore et al., 1994a) have been proposed in the framework of one-dimensional (1-D) hydrodynamic calculations, they have failed to reproduce the required abundance excesses. The reason for this is that mixing in 1-D models is inhibited because convection cannot be modeled accurately. In contrast, two-dimensional (2-D) simulations (Glasner & Livne, 1995; Glasner et al., 1997; Kercek et al., 1998; Glasner et al., 2005, 2007; Casanova et al., 2010, 2011) have shown that large convective eddies appear during the late stages of the thermonuclear runaway that induce shear flows at the core-envelope interface. Despite the promising results obtained in 2-D, a self-consistent 3-D calculation was lacking (Kercek et al., 1999). This is particularly important since it is known that convection develops very differently in 2-D and 3-D (Meakin & Arnett, 2007; Arnett et al., 2009). In this chapter, we present the first 3-D simulation of mixing at the core-envelope interface during a nova outburst.

The initial model (Glasner & Livne, 1995) consists of a $1\,M_\odot$ CO white dwarf

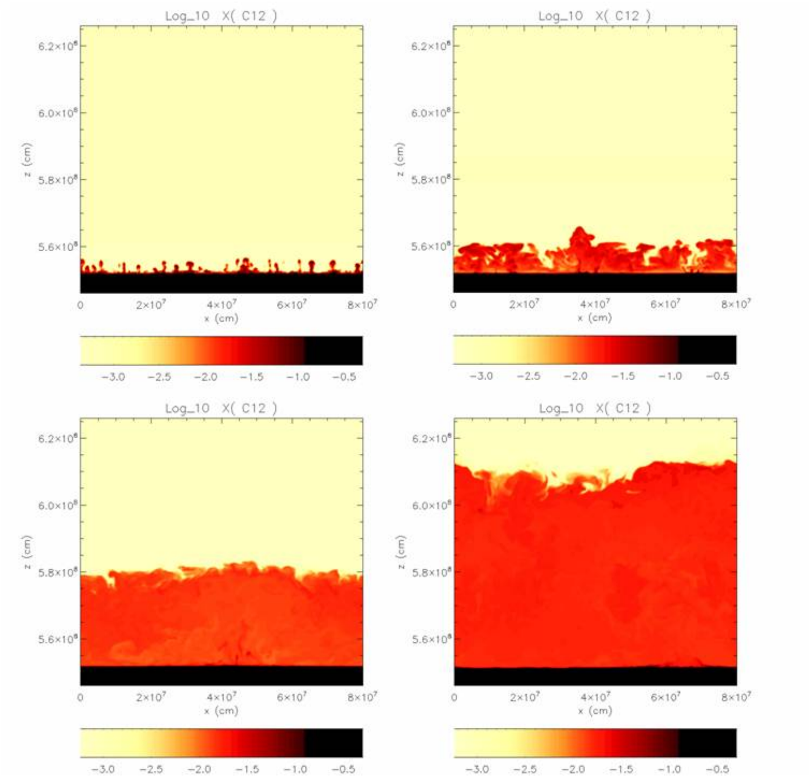

Figure 4.1: Snapshots of the development of Kelvin-Helmholtz instabilities at $t = 151$ s (upper left panel), 193 s (upper right), 296 s (lower left), and 379 s (lower right), shown in terms of the 12C mass fraction. Dredge-up of core material driven by Kelvin-Helmholtz instabilities translates into a mass-averaged abundance of CNO-nuclei in the envelope of 0.118, 0.129, 0.157, and 0.182, respectively. The mean CNO abundance at the end of the simulation reaches 0.20, by mass (see appendix D). Calculations were performed with the *FLASH* code (Fryxell et al., 2000) and run at the MareNostrum supercomputer, requiring 150000 CPU hours with 256 (occasionally, 512) processors. The typical resolution adopted was 3.12×3.12×3.12 km, with a maximum resolution of 1.56×1.56×1.56 km. The 3-D computational domain initially comprised 112 radial layers — including the outermost part of the CO core — and 512 horizontal layers along both horizontal axes. The mass of the accreted envelope was about $2 \times 10^{-5}\, M_\odot$. Nuclear energy generation was handled through a network of 13 species ^{1}H, ^{4}He, ^{12,13}C, ^{13,14,15}N, ^{14,15,16,17}O and ^{17,18}F, connected through 18 nuclear processes. Periodic boundary conditions were imposed at the four vertical sides of the computational domain while hydrostatic equilibrium with an outflow constraint at the top and a reflecting constraint at the bottom has been imposed on the velocity at the horizontal boundaries (Zingale et al., 2002). Other details on the input physics are identical to those adopted in our 2-D simulations — i.e., chapters 2 and 3; see also Casanova et al. (2010, 2011).

that accretes solar composition matter ($Z = 0.02$) at a rate of $5 \times 10^{-9}\, M_\odot$ yr^{-1}. The model has been evolved in 1-D and subsequently mapped onto a 3-D Cartesian grid of 800×800×800 km, when the temperature at the base of the envelope reached 10^8 K (see Fig. 4.1 and appendix D). The model was relaxed to guarantee hydrostatic equilibrium. A top-hat, 2 km wide temperature perturbation (Casanova et al., 2011) (5% amplitude) was imposed close to the core-envelope interface. This perturbation drives a shear flow triggering Kelvin-Helmholtz instabilities about $\sim$ 150 s after the start of the simulation. Small convection cells develop as soon as material is dredged-up into the envelope. The fluid velocity remains below the speed of sound, confirming that a nova outburst is driven by a (subsonic) deflagration rather than a (supersonic) detonation.

In fully developed turbulent convection, eddies are unstable in 3-D and consequently break up, transferring their energy to progressively smaller scales (Kolmogorov, 1991a,b; Pope, 2000; Shore, 2007). These structures, vortices and filaments, undergo a similar fate down to approximately the Kolmogorov scale, $\eta \sim (\nu^3/\epsilon)^{1/4}$, where ν is the kinematic viscosity and ϵ is the energy dissipation rate. This last stage is, however, intermittent and our 3-D simulations appear to resolve at least the upper dissipation range (see appendix D). Thus η provides an estimate of the size of the smallest eddies present in the flow. At this stage, the Reynolds number becomes sufficiently small and molecular viscosity is effective in dissipating the kinetic energy into heat. In sharp contrast, the conservation of vorticity in a 2-D geometry forces the small convective cells to merge into large eddies, with a size comparable to the height of the envelope, while energy flows to the viscous scale with a distribution that deviates from the Kolmogorov spectrum, reinforcing the injection of CO-rich material into the envelope.

At $t = 400$ s, matter crosses the outer computational boundary and we stop the calculations because of the Eulerian nature of the *FLASH* code. At this stage, the envelope base has reached a peak temperature of 1.82×10^8 K, and the mean (mass-averaged) metallicity in the envelope reaches $Z \sim 0.20$. This agrees with observations of CO novae and with previous 2-D modeling (Casanova et al., 2010, 2011), suggesting that the dimensionality of the convective treatment is not crucial to the mean values but is important for the details.

4.2 Inhomogeneous distribution of chemical species

A key feature of multidimensional nova models is their ability to produce different values for the yields of different isotopes. In the simulations, the burning advances along with the development of persistent density contrasts of large size, comparable to the thickness of the layer and much larger than the burning transition zone. These become turbulent, and the models require a fully 3-D treatment to capture the full spectrum of the plumes and vortex structures. The resulting abundances in

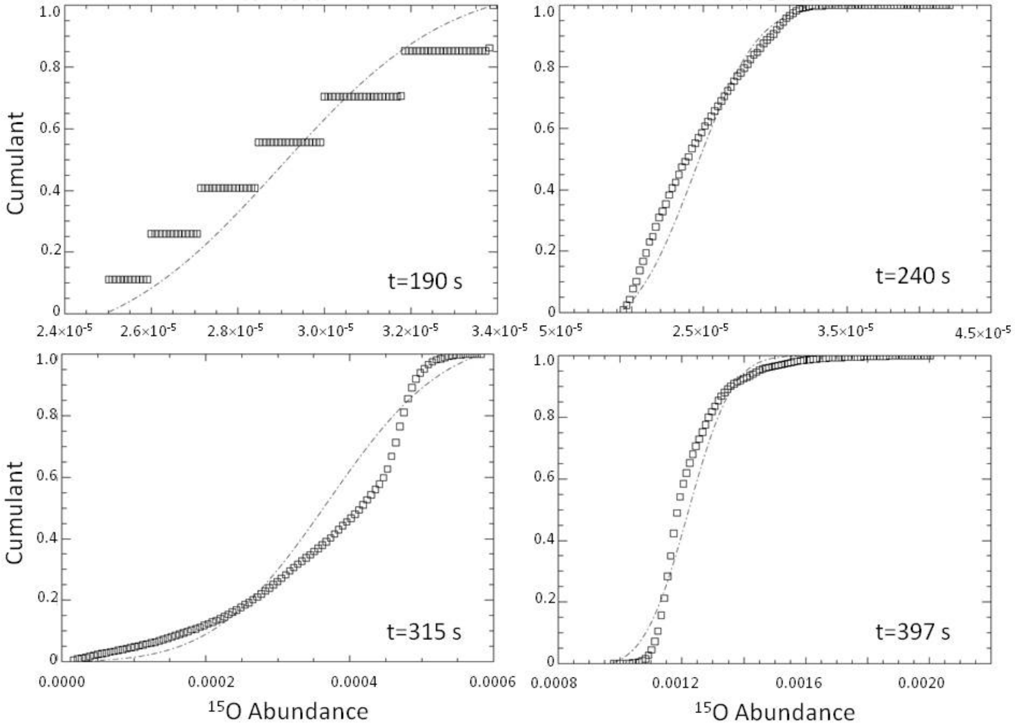

Figure 4.2: Cumulant distribution function for ^{15}O (squares), at $t = 190$, 240, 315 and 397 s, compared with a Gaussian process (dash line) with the same mean and dispersion. The cumulant distribution shows the probability that a variable, x, has a value equal or below a threshold value, a (i.e., $P[x \leq a]$). The cumulant distribution is estimated by means of an arbitrary layer, 100 km thick ($5.75 \times 10^8 - 5.85 \times 10^8$ cm; $\sim$ 27648 data points), a size comparable with the pressure scale height. The evolution shows the effects of the intermittent bursts seen in the accompanying movies (see appendix D).

our simulations have another particular feature that agrees with observations, the structures are inhomogeneous and display large density contrasts. A few high spatial resolution observations of novae taken soon after the optically thin transition in the first months of expansion, before the matter has suffered substantial modifications through interactions with the interstellar medium, reveal large chemical inhomogeneities. For example, although an ONe nova, V1974 Cyg showed a large C/He difference, more than a factor of 3, between two knots resolved in the spectrum a few years after outburst that substantiated inferences drawn from integrated spectra (Shore et al., 1996). The ejecta are always highly fragmented as soon as individual features can be discerned in the line profiles. Comparison of infrared with ultraviolet spectra for the same ions at stages when the former, then the latter, turn optically thin shows the same structures to be present even during the optically opaque stage

(Gehrz, 2008; Shore, 2008).

This has been explained as a relic of a Rayleigh-Taylor instability during the initial stage of the ejection. We have shown that such structures do indeed appear within the burning zone, the initial plumes, and that these develop a secondary Kelvin-Helmholtz vortex cascade that induces the onset of turbulent motions. In this very high Reynolds number regime, the structures are concentrated as vortices and filaments. These are more evident in the 2-D simulations, but cascade rapidly into smaller eddies and filaments, subject to recombination and extension, as the burning continues. Such dissipation is intermittent, leading to coherent, persisting structures that advect with the expanding layer. Since the nuclear reaction rates are density sensitive, higher density knots have a different nuclear history than the background and this is best characterized by the abundance distribution function behind the deflagration.

We show a sample of the time evolution of the cumulant function in Fig. 4.2. The initial abundance for ^{15}O, our trace species (whose abundance is increased by the deep non-uniform mixing after the onset of thermal buoyant turbulence) is a narrow initial distribution that evolves into a stable form with a lower cut-off and a power law tail toward high abundances. Unlike the single value from 1-D models, we find a 30% dispersion in the main component, fitted by a Gaussian (the dashed line in Fig. 4.2), and containing $\sim$ 10% of the total volume an extended, non-Gaussian “fat tail” whose maximum abundance (at the 1% level) extends up to 13σ from the mean ^{15}O for the volume. One of the results often found from multiwavelength abundance analyses during the nebular stage, that there is a large dispersion from line to line in the abundance ratios of the principal species, may actually be a signature of the turbulence generated during the thermonuclear runaway.

The contrast between these residual structures will be further amplified by the supersonic motions that follow the stage shown here. Such fluctuations in abundance, opacity and density will leave imprints not only in the ejecta but any initial outflows and even the formation of dust and effect estimates of the maximum achievable luminosities during the explosion such as the extent to which classical nova explosions can exceed the Eddington luminosity and where this occurs.

Chapter 5

Conclusions and future work

5.1 Conclusions

In this thesis we have analyzed the mixing mechanisms that operate at the core-envelope interface during classical nova explosions by means of the explicit, Eulerian, parallelized, hydrodynamical *FLASH* code. The set of two- and three-dimensional simulations have been performed on the MareNostrum Supercomputer of the Barcelona Supercomputing Center, requiring a total amount of 1000 kh.

The two-dimensional simulations demonstrate that Kelvin-Helmholtz instabilities can account for self-enrichment of the accreted material with matter from the outermost layers of the white dwarf core, at levels that agree with observations (metallicities above 0.20). To break the initial hydrostatic equilibrium, a temperature perturbation was imposed at the initial time step. This translates into a myriad of instabilities that arise, later on, right at the interface. These first instabilities are buoyancy-driven, and resemble Rayleigh-Taylor instabilities (Shankar et al., 1992; Shankar & Arnett, 1994). The first plummes rise and expand as they dissipate. The general behavior is in agreement with the results reported by Glasner & Livne (1995), Glasner et al. (1997) and Glasner et al. (2007). The onset of the first fluctuations, is followed by the formation of small convective cells in the innermost envelope layers powering an efficient shear, which in turn spawns the formation of Kelvin-Helmholtz instabilities. These instabilities efficiently dredge-up core material into the envelope, while the convective cells grow in size. The convective front progressively moves upwards and eventually reaches the top of the computational domain. The two-dimensional geometry imposed forces conservation of vorticity, which translates into convective cells recombining and merging into large cells that occupy half of the envelope. Similar features were found in Glasner et al. (1997), and clearly contradict the formation of small eddies as suggested by Kercek et al. (1998). Despite two-dimensional simulations of reactive flows do not describe accurately the way convection develops (Meakin, 2006; Meakin & Arnett, 2007; Arnett et al., 2009), this study proved Kelvin-Helmholtz instabilities as a very efficient mixing mechanism that can account for the required CNO enrichment in classical novae.

In the second part of this thesis, we have presented the results of a sensitivity study, aimed at analyzing the possible influence of the location, size and intensity of the temperature perturbation on the results. The study proved that neither any of these parameters, nor the shape adopted for the perturbation (top-hat or Gaussian) have any effect in the results. We have also tested the possible impact of the duration of the initial perturbation. Usually we have implemented it only at the initial time, lasting for one timestep ($\sim 10^{-10}$ s). Longer initial perturbations shorten the onset of the initial instabilities, but the main results (i.e., metallicty) remain unaffected. We have also investigated the influence of the size of the computational domain: increasing the width of the domain has no noticeable effect. A similar behavior is found when the height of the envelope is increased, although larger metallicities ($Z \sim 0.29$) are found, because the convective front needs more time to reach the top of the domain, and therefore, Kelvin-Helmholtz instabilities operate and pump up ^{12}C for a longer time. Finally, we have also tested the influence of the level of refinement adopted. Most of our simulations have been performed with a reasonably accurate level of refinement, 1.56 km, similar to those adopted in Kercek et al. (1998) and Glasner et al. (2007). We have proven that increasing the refinement of the simulation to 0.39 km, translates into somewhat longer timescales (such as the time needed by the convective front to reach the outer boundary), as also reported in Kercek et al. (1998). This might be caused by the more limited numerical diffusion that accompanies the simulations performed with high refinement. Nevertheless, the most relevant results of the simulation (metallicity, temperatures, velocities…) are not affected by the adopted resolution, as also reported in Glasner et al. (2007). In all these simulations, the velocities achieved in the envelope are always below the speed of sound, thus proving that nova outbursts propagate through deflagrations rather than through detonations. As also found by Glasner et al. (1997), we conclude that the thermonuclear runaway starts as a suite of irregular temperature fluctuations, spreading laterally to finally undergo a global thermonuclear runaway that propagates with almost spherical symmetry.

It is also worth stressing that numerical diffusion introduces limitations on the simulations. One of the characteristic problems that arise from Eulerian codes is their difficulty to describe interfaces. Numerical diffusion will tend to broaden the interface, leading to numerical mixing, which acts as an artificial perturbation. Part of the core material will be artificially injected into the envelope, thus contributing to the final mixing (Kercek et al., 1998; Glasner et al., 2007). Even if we cannot control the effect of numerical mixing, we can reduce its effects by adopting a good resolution. Furthermore, we have shown that the final amount of mixing is not influenced by the level of refinement and hence, despite the presence of numerical diffusion, *FLASH* is able to describe accurately the mixing episodes during classical novae, despite microphysical processes operating at the interface cannot be captured as they operate at scales much below the adopted refinements.

Complementing the two-dimensional studies mentioned above, we have also performed the first three-dimensional simulation of mixing at the core-envelope interface during nova explosions. Despite two-dimensional models can be used to describe these mixing episodes, the imposed geometry induces a very specific convective pattern that differs from the predicted Kolmogorov theory. Our three-dimensional simulation shows also the genesis of the same initial temperature fluctuations arising at the interface and the onset of convection. However, small eddies do not merge as in the two-dimensional case; instead, they break up, transferring their energy to progressively smaller scales. These structures, vortices and filaments, undergo a similar fate down to approximately the Kolmogorov scale. Although turbulence does not reach a relaxed state in our simulations, we can reproduce part of this behavior. We have shown that the envelope enters a turbulent stage, where large filaments and plumes are formed, and through which mixing finds a way to proceed. The convective eddies are engulfed at the upper zones of the convective front. This bursting behavior becomes stronger at the late stages of the simulation, powering robust Kelvin-Helmholtz instabilities and hence, driving a very effective deep mixing. An important result obtained in this three-dimensional simulations is that the presence of inhomogeneities in chemical species reside in the intermittent pattern inferred from turbulence. Intermittency is a characteristic of fully developed turbulence (Meakin & Arnett, 2007; Arnett et al., 2009; Arnett & Meakin, 2010). These intermittent and filamentary features induce large density contrasts that translate into inhomogeneous patterns, which in turn may influence subsequent phases during and after the expansion, such as dust formation. This may be the source of the inhomogeneous distribution of chemical species seen in the spectra from novae, the origin of which has remained unknown for 40 years.

It is worth noting that, despite the different convective profile encountered in three dimensions, as compared with the two-dimensional case, the global quantities do not depend on the dimensionality. For instance, the overall envelope metallicity reaches 0.20 in the three-dimensional case, a value which is in concordance with the values reported in our two-dimensional simulations. Other physical quantities, such as the maximum temperatures achieved or the rates of nuclear energy generation obtained, are also similar, proving that two-dimensional calculations can reproduce quantitatively the gross picture of mixing in classical novae, although they cannot account for an accurate description of convection, turbulence and their implications.

5.2 Future work

One of the limitations we have encountered in our simulations is the reduced computational domain that can be modeled. As we move outwards, towards the top of the envelope, densities and the pressure scale height become smaller. In our simulations, when the radius is $\sim 6.46 \times 10^8$ cm, density drops below 1 g cm^{-3}. Under hydrostatic equilibrium conditions, density would underflow breaking the stability of the calculation. At least there are two possibilities to work around this problem:

1. To model only a small portion of the envelope before density drops off (Zingale et al., 2002). This is understood as if we were removing the outermost accreted layers from above the domain. Therefore, a hydrostatic boundary condition can be adopted at the top of the domain. This is the technique adopted in the calculations reported in this thesis (the largest domain we have used is 1000 km — simulation L, see chapter 3). The simulations thus performed introduce an important constraint, since matter will flow off the grid and will not contribute to the dynamics anymore.

2. To extend the domain by putting the initial model into hydrostatic equilibrium until an arbitray cutoff is reached (Zingale et al., 2002), much before the values underflow. All layers above the cutoff will have a constant density, equal to the cuttoff value. This will allow to increase the size of the domain avoiding the underflows. Usually the density cuttoff is taken small enough to be dynamically unimportant (Zingale, 2000; Zingale et al., 2001). The zone with constant density, the so-called “fluff”, is not in hydrostatic equilibrium and hence, matter will fall. This fact has little effect on the dynamics of the simulation (Zingale, 2000; Zingale et al., 2001, 2002). Nevertheless, the use of the fluff would allow to track the outburst and thus, follow the expansion to some extent.

Both methods are able to support a hydrostatic envelope (Zingale et al., 2002). The implementation of a version of the “fluff” condition, which would allow to follow the expansion stage, is among our future priorities.

An alternative is to rely on an expanding grid that detaches from the original Eulerian grid. Glasner & Livne (1995), Glasner et al. (1997) and Glasner et al. (2007) used the ALE (Arbitrarily Lagrangian Eulerian) code *VULCAN*, which describes the interface by means of an Eulerian frame and tracks the expansion switching to a Lagrangian approach. Glasner et al. (2005) constructed a mass conserving grid such that the outer boundary expands with time while allowing to track the ejecta and to study the important role played by the unstable isotopes ^{13}N,^{14}O,^{15}O and ^{17}F in the outermost layers (Glasner et al., 1997). We are planning to implement an ALE code on top of *FLASH*, based on the method described in Glasner et al. (2005).

Once Kelvin-Helmholtz instabilities have been proven to account for the CNO enhancement in CO novae, we want to extend this work to the following related scenarios:

- Neon novae: these type of novae host an ONe white dwarf and reach higher peak temperatures, as a consequence of the small amount of ^{12}C injected from the outer core layers. The importance of these calculations resides on the fact that the metallicity inferred from the ejecta of ONe novae reaches higher values than in CO novae, with $Z \sim 0.30 - 0.50$ and up to 0.80 in some cases (Gehrz et al., 1998; José & Hernanz, 1998; José & Shore, 2008). The thermonuclear runaway operates in the same way as in CO novae and therefore, ONe novae provide a good scenario to test the efficiency of Kelvin-Helmholtz instabilities in reproducing the observed metallicities in different scenarios. To this end, the nuclear network should be extended to include heavier isotopes (i.e., the NeNa and MgAl mass regions).

- Primordial novae: these novae undergo explosions driven by accretion of extremely metal-defficient matter on top of the compact object. The outburst is more energetic than in classical nova ones, with an extension of the nucleosynthetic endpoint towards Cu-Zn (José et al., 2007). Multi-dimensional studies could also shed light on the competition between the reactions ^{14}N(p,γ)^{15}O and ^{12}C(p,γ)^{13}N as the main triggers of the explosion (Shen & Bildsten, 2009).
- Recurrent novae: this subclass has recurrence times < 100 years. The outburst takes place after accreting matter at high rates onto a very massive white dwarf, close to the Chandrasekhar limit. The outburst is less energetic than that of a classical nova, and the metallicity enhancement is believed to be lower, scarcely reaching above solar values. The extend of mixing through the core-envelope interface is yet a matter of debate. Actually, recurrent novae seem to be a perfect scenario to test different mixing mechanisms, since it is not clear whether convective overshoot would have time to operate. Therefore, other mixing mechanisms, such as diffusion, would be at the forefront of possible explanations.

We have initiated multi-dimensional calculations of ONe, recurrent and primordial novae through the project “Three-dimensional Models of Novae: ONe, Primordial and Recurrent Novae” (code *AECT-2011-2-0007*), for which 450 kh have been allocated by the Barcelona Supercomputer Center. These calculations rely on initial models computed with *SHIVA*, a one-dimensional, Lagrangian, implicit hydrodynamic code (José & Hernanz, 1998).

It is also worth noting that the final amount of mixing can result from a combination of different mechanisms (including diffusion, shear mixing, Kelvin-Helmholtz instabilities…). Hence, as future work, we plan to investigate early mixing episodes by mapping the initial model at earlier times, when $T \sim 10^7$ K (Glasner et al., 2007). In a second stage, we plan to study a possible mixing mechanism driven by the presence of magnetic fields. The possibility of extra-mixing in Asymptotic Giant Branch (hereafter, AGB) stars by magnetic buoyancy has been recently studied by Busso et al. (2007), Nordhaus et al. (2008) and Palmerini & Busso (2008). The *FLASH* code can solve the fluid dynamics equations in the presence of magnetic fields, allowing the possibility of porting the hypothesis of extramixing in AGB stars to classical novae.

Finally, we are also interested in the application of the methodology described in this thesis to type I X-ray bursts. In this scenario, accretion proceeds on top of a neutron star until the explosion ensues. These stellar explosions have basically been analyzed with one-dimensional calculations, while multi-dimensional studies have been scarce to date. Zingale et al. (2001) approached this scenario with the *FLASH* code, but studying He detonations (rather than deflagrations) on neutron stars. A more realistic attempt has been recently reported by Malone et al. (2011). This two-dimensional study, performed with the low-Mach number code *MAESTRO*, focuses on the development of convection prior to the thermonuclear runaway in He-accreting neutron stars. In line with the multi-dimensional nova explosions presented in this thesis, we have started a suite of simulations to investigate multi-dimensional effects in type I X-ray bursts. We have mapped a one-dimensional model computed with the *SHIVA* code onto the grid of *FLASH*, when the temperature at the innermost envelope layers reaches $\sim 6 \times 10^8$ K. So far, we have implemented a reduced nuclear network with 17 isotopes (^{1}H, ^{3,4}He, ^{12}C, ^{14}N, ^{16}O, ^{20}Ne, ^{24}Mg, ^{28}Si, ^{32}S, ^{36}Ar, ^{40}Ca, ^{44}Ti, ^{48}Cr, ^{52,54}Fe, and ^{56}Ni) and 86 nuclear reactions to account for the energetics of the explosion. This study should shed light into how combustion starts and spreads over the accreted envelope under the challenging physical conditions that characterize neutron stars.

Appendix A

The *FLASH* code

The *FLASH* code is a parallelized, multi-dimensional hydrodynamical code built at the FLASH Center for Astrophysical Thermonuclear Flashes of the University of Chicago to study explosive stellar regimes such as Type Ia supernovae, Type I X-ray bursts and classical nova explosions. It is an Eulerian grid-based code that implements an adaptive mesh refinement method and uses the Message-Passing Interface libray for computer communications. The routines are written in Fortran 90 and C. The *FLASH* code also uses the Hierarchical Data Format (HDF) for the output and needs specific visualization tools, such as Interactive Data Language (IDL) or VISIT.

A.1 Hydrodynamics

The *FLASH* code describes the dynamics of a compressible fluid using Euler's equations:

$$\frac{\partial \rho}{\partial t} + \nabla \cdot (\rho \mathbf{v}) = 0 \tag{A.1}$$

$$\frac{\partial \rho \mathbf{v}}{\partial t} + \nabla \cdot (\rho \mathbf{v}\mathbf{v}) + \nabla P = \rho \mathbf{g} \tag{A.2}$$

$$\frac{\partial \rho E}{\partial t} + \nabla \cdot (\rho E + P)\mathbf{v} = \rho \mathbf{v} \cdot \mathbf{g} \tag{A.3}$$

where $\mathbf{g}$ is the gravitational acceleration, ρ and $\mathbf{v}$ are, respectively, the density and velocity of the fluid, P is the pressure and E is the thermokinetic energy per unit mass:

$$E = \epsilon + \frac{1}{2}|v|^2 \tag{A.4}$$

where ϵ is the internal energy. These equations express the conservation of mass, momentum and energy, but need to be closed with the equation of state (see Sect. A.3). Furthermore, in reactive flows, each species l with a mass fraction X_l should fulfill the following advection equation:

$$\frac{\partial \rho X_l}{\partial t} + \nabla \cdot (\rho X_l \mathbf{v}) = 0 \tag{A.5}$$

satisfying the closure requirement

$$\sum_l X_l = 1. \tag{A.6}$$

Numerical mixing or diffusion may arise from the fact that the code does not track the interfaces explicitly.

The *FLASH* code uses an explicit, directionally split piece-wise parabolic method (hereafter, PPM), which was first introduced by Colella & Woodward (1984) and Woodward & Colella (1984). To be specific, to describe the dynamics of the fluid the code uses the direct Eulerian implementation described in Colella & Woodward (1984), whichs consists in solving the Euler equations directly. The version of PPM implemented in *FLASH* is an algorithm derived from the method described in the *PROMETHEUS* code (Fryxell et al., 1989). The basis of PPM can be found in Godunov's schemes (Godunov, 1959; Godunov et al., 1961). A Godunov's scheme is a finite volume method that splits the domain into a series of zones, where each of the conserved quantities is processed as constant values (that is, piecewise-constant). Then, at each cell interface, the Riemann problem is solved, and the solutions are used to evaluate the fluxes at the boundaries. After this reconstruction step, quantities can be advanced in time taking the previous fluxes into account. Godunov's schemes are accurate only to first order both in space and time. PPM is a high-order scheme that implements the method used by Godunov's schemes. However, the improvement comes from using piecewise-parabolic functions (instead of piecewise-constant) to represent the conserved quantities in each cell. Godunov's schemes and PPM give good performances when dealing with contact discontinuities and sharp shocks and do not introduce important numerical oscillations. Actually, PPM methods achieve these accuracies by introducing monotonicity criteria. That is, the interpolant function in each cell takes values between the averaged values of the adjacent cells. The monotonicity constraint, already introduced in the *MUSCL* scheme (van Leer, 1979), is a very effective mechanism to control non-physical oscillations, becoming a good alternative to classical dissipation methods.

To complement the monotonicity restriction, *FLASH* also implements a flattening method. When shock features are too narrow, post-shock oscillations may arise behind the shock. Instead of applying an explicit amount of dissipation, the code flattens the structure of the shocks that are too narrow (that is, steep and strong shocks). The result is a structure which is flatter, reducing the formation of oscillations. The flattening procedure will be applied when the structure is indeed a shock (a pressure jump above a given shock parameter and a fluid compression). However, PPM suffers from numerical diffusion and hence, contact discontinuities become broader as time goes on. However, a steepening procedure can be used to keep contact discontinuities as sharp as posible, preventing them to diffuse infinitely. This steepening mechanism is applied on density and chemical species. The method is generalized to use all sort of equations of state (Colella & Glaz, 1985) and to prevent overshoots in abundances (Plewa & Müller, 1999). To solve multi-dimensional problems, *FLASH* uses a splitting technique (Strang, 1968), based on alternating sweeps along each direction. Although, as mentioned earlier, the PPM scheme uses techniques such as monotonicity and flattening, instead of direct dissipative methods, to ensure accuracy when using the splitting technique, a small artificial viscosity is added (Lapidus, 1967). Moreover, an additional analytical artificial viscosity may also be added to prevent oscillations within shocks (Colella & Woodward, 1984).

Finally, the *FLASH* code uses explicit methods and therefore, the hydrodynamical timestep is limited by the Courant-Friedrichs-Lewy condition:

$$dt = K \cdot \min\left\{ \frac{d_x}{c_\mathrm{s} + |v_x|}, \frac{d_y}{c_\mathrm{s} + |v_y|}, \frac{d_z}{c_\mathrm{s} + |v_z|} \right\} \tag{A.7}$$

where c_s is the speed of sound and d_x, d_y and d_z are the cell sizes. The constant K in this equation should be set to a value below 1 to ensure stability, preventing information to travel more than one cell over a timestep. Typically, in our simulations when a resolution of 1.56 km is adopted, $dt \sim 10^{-4}$ s.

A.2 Adaptive Mesh Refinement

FLASH is an Eulerian code that uses blocks to cover the computational domain. An initial number of parent blocks along each direction is given at the beginning. Each block is surrounded by a frame of guard cells (4 guard cells when using explicit PPM) that are used to update the interior cells of a block with information from a neighbouring block data and/or imposed boundary conditions. Each block is also divided in `nxb`, `nyb` and `nzb` cells along each direction (usually 8 interior cells by default). Since using an equally spaced grid is computationally expensive, the code uses the Adaptive Mesh Refinement (AMR) method that allows to refine or derefine when needed. The AMR package used by *FLASH* is based on the *PARAMESH* library (MacNeice et al., 2000). The criterion used to refine and derefine blocks is based on Lohner's error indicator (Lohner, 1987), which uses the following second-derivative condition (in a multi-dimensional form):

$$E_{i_1,i_2,i_3} = \left[\frac{\sum_{pq} \left(\frac{\partial^2 u}{\partial x_p \partial x_q} \Delta x_p \Delta x_q \right)^2}{\sum_{pq} \left[\left(\left| \frac{\partial u}{\partial x_p} \right|_{i_p+1/2} + \left| \frac{\partial u}{\partial x_p} \right|_{i_p-1/2} \right) \Delta x_p + \epsilon \frac{\partial^2 |u|}{\partial x_p \partial x_q} \Delta x_p \Delta x_q \right]^2} \right]^{1/2} \tag{A.8}$$

The expression is applied to a given variable u in the $i_1 i_2 i_3$-th cell. Lohner's estimator appears to be a good prescription for refining the correct zones such as sharp contact discontinuities or smoothed profiles (and not refining the formation of wiggles that may appear as a consequence of noise). The value ϵ is set to 10^{-2} by default. The error estimated in this way is compared to the values of the refine cutoff and derefine cutoff, which are set to 0.8 and 0.2 respectively by default. *FLASH* will refine if $E_{i_1 i_2 i_3}$ is greater than the refine cutoff and derefine if it is smaller than the corresponding cuttof. These values can be adjusted if the user wants to constrain the refinement criterion. The refinement criterion is checked every two timesteps by default through the parameter `nrefs`, which can be changed if the user needs a different frequency of refinement.

Because *FLASH* uses the AMR method, the mesh structure will appear as a hierarchical tree structure that fulfills the following rules:

- A new child block has to have half size of the parent block.
- The child block has to be nested inside the parent block.
- Adjacent blocks cannot differ by more than one level of refinement.

FLASH will start the simulation with `nblockx` × `nblocky` × `nblockz` top level blocks and with an initial level of refinement `Nref`, which is defined as the number of divisions along each direction that an arbitrary block may suffer during a simulation. Therefore, the number of blocks that will cover the domain at the maximum refinement will be $2^{\texttt{Nref}-1}$. The maximum level of refinement, as well as the minimum level (in case we want a minimum refined mesh), can be set as initial parameters. Usually our simulations started with 4 parent top blocks along each direction and with 5 levels of refinement that translates into a resolution of 1.56 km.

In case that the refinement criterion should be more accurate, complementary methods can be used. For instance, *FLASH* enables the possibility to refine specific zones within the computational domain that need special refinement or to refine a specific variable above or below a given threshold.

A.3 Equation of State

As mentioned in Sect. A.1, the physical description of a fluid needs to be closed with the equation of state, which relates the different thermodynamic variables. *FLASH* uses the *Helmholtz* equation of state, which is suitable for degenerate stellar matter (Timmes & Arnett, 1999; Timmes & Swesty, 2000). Given and isotope i with Z_i protons, A_i nucleons, mass density ρ_i and number density n_i, we define the mass fraction as:

$$X_i = \frac{\rho_i}{\rho} = \frac{n_i A_i}{\rho N_A}, \tag{A.9}$$

and the molar abundance as:

$$Y_i = \frac{X_i}{A_i} = \frac{n_i}{\rho N_\mathrm{A}} \tag{A.10}$$

where N_A is Avogadro's number. We also define the mean number of nucleons per isotope:

$$\bar{A} = \frac{1}{\sum_i \frac{X_i}{A_i}}, \tag{A.11}$$

the mean charge per isotope:

$$\bar{Z} = \bar{A} \sum_i \frac{Z_i X_i}{A_i} \tag{A.12}$$

and the number of electrons per baryon:

$$Y_\mathrm{e} = \frac{\bar{Z}}{\bar{A}} \tag{A.13}$$

FLASH takes the temperature, density, mean number of nucleons per isotope, mean charge per isotope and composition as input and evaluates the pressure, entropy and internal energy, the specific heats and the adiabatic indices needed by the hydrodynamic module (Colella & Glaz, 1985). In order to check thermodynamic consistency, the following derivaties are also returned after calling the equation of state:

$$\left(\frac{\partial P}{\partial T}\right)_\rho, \quad \left(\frac{\partial P}{\partial \rho}\right)_T, \quad \left(\frac{\partial \epsilon}{\partial T}\right)_\rho, \quad \left(\frac{\partial \epsilon}{\partial \rho}\right)_T, \quad \left(\frac{\partial S}{\partial T}\right)_\rho, \quad \left(\frac{\partial S}{\partial \rho}\right)_T.$$

The equation of state implemented should evaluate the previous quantities as quick as posible and with good accuracy, since in a multi-dimensional simulation one may call the equation of state at least 10^{10} times. It has been proven that the *Helmholtz* equation of state executes faster than other equations of state (Timmes & Swesty, 2000).

The *Helmholtz* equation of state comprises contributions from ions, radiation and degenerate electrons and positrons. Coulomb corrections are also taken into account. Hence, the final pressure, energy and entropy will contain the following contributions:

$$P = P_{\rm rad} + P_{\rm ion} + P_{\rm e^-} + P_{\rm e^+} + P_{\rm Coul}, \tag{A.14}$$

$$S = S_{\rm rad} + S_{\rm ion} + S_{\rm e^-} + S_{\rm e^+} + S_{\rm Coul}, \tag{A.15}$$

and:

$$\epsilon = \epsilon_{\rm rad} + \epsilon_{\rm ion} + \epsilon_{\rm e^-} + \epsilon_{\rm e^+} + \epsilon_{\rm Coul} \tag{A.16}$$

The ion contribution is computed as an ideal gas:

$$P_{\rm ion} = \frac{N_{\rm A} k_{\rm B}}{\bar{A}} \rho T \tag{A.17}$$

where $k_{\rm B}$ is Boltzmann's constant.

$$\epsilon_{\rm ion} = \frac{1}{\gamma - 1} \frac{N_{\rm A} k_{\rm B}}{\bar{A}} T \tag{A.18}$$

where γ is the adiabatic index. The entropy is provided by the Sackur-Tetrode relation:

$$S_{\rm ion} = \frac{P_{\rm ion}/\rho + \epsilon_{\rm ion}}{T} + \frac{N_{\rm A} k_{\rm B}}{\bar{A}} \log \left[\frac{\bar{A}^{5/2}}{N_{\rm A} \rho} \left(\frac{2\pi m_{\rm p} k_{\rm B} T}{h^2} \right)^{3/2} \right] \tag{A.19}$$

where $m_{\rm p}$ is the proton rest mass and h is Planck's constant.

Radiation is treated as a blackbody and therefore, its contribution is as follows:

$$P_{\rm rad} = \frac{a T^4}{3} \tag{A.20}$$

$$\epsilon_{\rm rad} = \frac{3 P_{\rm rad}}{\rho} \tag{A.21}$$

$$S_{\rm rad} = \frac{P/\rho + \epsilon}{T} \tag{A.22}$$

where $a = \frac{4\sigma}{c}$, being σ and c the Stephan-Boltzmann's constant and the speed of light, respectively.

Electrons and positrons are described with a non-interacting Fermi gas with an arbitrary degree of degeneracy and relativity. This formalism involves the evaluation of tedious calculations, such as the Fermi-Dirac integrals, to finally find the pressure, specific internal energy and entropy contributions. A state of the art look-up table method is implemented to obtain these thermodynamic quantities by means of the evaluation of the Helmholtz free energy, F, and its derivatives:

$$F = \epsilon - TS, \qquad dF = -SdT + \frac{P}{\rho^2} d\rho \tag{A.23}$$

$$P = \rho^2 \left(\frac{\partial F}{\partial \rho} \right)_T \tag{A.24}$$

$$S = - \left(\frac{\partial F}{\partial T} \right)_\rho \tag{A.25}$$

Starting from the first law of thermodynamics:

$$d\epsilon = TdS + \frac{P}{\rho^2} d\rho \tag{A.26}$$

the following Maxwell relations need to be satisfied, such that the previous equation is an exact differential:

$$P = \rho^2 \left(\frac{\partial \epsilon}{\partial \rho} \right)_T + T \left(\frac{\partial P}{\partial T} \right)_\rho \tag{A.27}$$

$$\left(\frac{\partial \epsilon}{\partial T} \right)_\rho = T \left(\frac{\partial S}{\partial T} \right)_\rho \tag{A.28}$$

$$- \left(\frac{\partial S}{\partial \rho} \right)_T = \frac{1}{\rho^2} \left(\frac{\partial P}{\partial T} \right)_\rho \tag{A.29}$$

An equation of state that fulfills these relations will be thermodynamically consistent. The relations derived from the Helmholtz free energy, such as the pressure and the entropy, satisfy the first two Maxwell relations. The third Maxwell relation is satisfied if F satisfies:

$$\frac{\partial^2 F}{\partial T \partial \rho} = \frac{\partial^2 F}{\partial \rho \partial T} \tag{A.30}$$

In the *Helmholtz* equation of state, a table of the Helmholtz free energy $F(\rho, T)$ is provided and an interpolating function that satisfies the above mentioned relations to guarantee thermodynamical consistency is constructed. Given the values of $F(\rho, T)$, the internal energy, the pressure and the entropy are evaluated (the two last quantities are evaluated by means of the first derivative of F). The derivatives of the pressure, entropy and internal energy are required to be continuous, which in turn, imposes a restriction on the second derivatives of the interpolant function. At the end, these requirements impose 6 restrictions and therefore, at least a quintic order polynomial will be needed. Since the Helmholtz free energy is tabulated for both density and temperature, a biquintic Hermite polynomial is used. The coefficients of this interpolant function $H_5(\rho, T)$ are evaluated with the values of the Helmoltz free energy F and the following eight partial derivatives:

$$\left(\frac{\partial F}{\partial T}\right), \quad \left(\frac{\partial F}{\partial \rho}\right), \quad \left(\frac{\partial^2 F}{\partial T^2}\right) \quad , \left(\frac{\partial^2 F}{\partial \rho^2}\right), \quad \left(\frac{\partial^2 F}{\partial T \partial \rho}\right),$$
$$\left(\frac{\partial^3 F}{\partial T^2 \partial \rho}\right), \quad \left(\frac{\partial^3 F}{\partial \rho^2 \partial T}\right), \quad \left(\frac{\partial^4 F}{\partial T^2 \partial \rho^2}\right).$$

A look-up table and an interpolant function constructed like this will be thermodynamically consistent. The input table is formed with the Timmes equation of state (Timmes & Arnett, 1999) with values stored with 16 figures, spanning the following range of values for density and temperature: $10^{-10} < \rho < 10^{11}$ g cm^{-3} and $10^4 < T < 10^{11}$ K. The table is constructed with 211 density points and 71 temperature points. These values are chosen to guarantee maximum accuracy. The table is constructed with $Y_{\rm e} = 1$ — that is, pure hydrogen — but it can be used for any composition, since the final values can be scaled to $Y_{\rm e}$ by multiplying or dividing in the final expressions.

Finally, Coulomb corrections are computed based on the work of Yakovlev & Shalybkov (1989) and added to the final pressure, entropy and specific internal energy. These corrections are aimed to include the interactions between ions and the electron gas.

A.4 Thermal Diffusion

Thermal diffusion is implemented in *FLASH* by adding the heat flux in the energy equation:

$$\frac{\partial \rho E}{\partial t} + \nabla \cdot (\rho E + P)\mathbf{v} = \rho \mathbf{v} \cdot \mathbf{g} + \nabla \cdot \mathbf{F}_{\rm heat} \tag{A.31}$$

where $\mathbf{F}_{\rm heat} = -\sigma(X_i, \rho, T)\nabla T$ is the heat flux and σ is the thermal conductivity. The procedure used to calculate the conductivity and its corresponding diffusion coefficient is based on the method described and tested by Timmes (2000). To get the thermal conductivity, a total opacity with the radiative and conductive contributions is first calculated as follows:

$$\frac{1}{\kappa} = \frac{1}{\kappa_{\rm rad}} + \frac{1}{\kappa_{\rm cond}} \tag{A.32}$$

The total opacity thus calculated is converted to conductivity using the expression

$$\sigma = \frac{4acT^3}{3\rho\kappa}, \tag{A.33}$$

which, in turn, will be converted to the corresponding diffusion coefficient

$$D = \frac{\sigma}{\rho c_P}, \tag{A.34}$$

where c_P is the specific heat at constant pressure.

The conductive opacity evaluates the degenerate region contribution separately from the non-degenerate one, and applies a blending of both expressions in the intermediate regions. This method uses analytical fits from Iben (1975) for the non-degenerate contribution, and from Yakovlev & Urpin (1980) and Potekhin et al. (1997) for degenerate regions. Contributions from both ion-electron and electron-electron collisions are included. The radiative opacity is evaluated from analytical fits based on those found in Christy (1966) and Iben (1975) depending upon the composition, temperature and density. Furthermore, the Compton scattering opacity contribution is taken into account as in Weaver et al. (1978).

A.5 Nuclear reactions

The *FLASH* code includes a burn unit to implement nuclear networks and, therefore, to include the energy release by nuclear processes. *FLASH* implements the tested method described in Timmes (1999). The network we have used consists of 13 isotopes: ^{1}H, ^{4}He, ^{12,13}C, ^{13,14,15}N, ^{14,15,16,17}O, and ^{17,18}F, linked through 18 nuclear reactions. In fact, this is a "hardwired" nuclear network since all the sequences are entered by hand in the code. The network is connected through p-captures and β^{+}-decays that will supply the energy release during the thermonuclear runaway episode. The reaction rates are those described in Angulo et al. (1999), José et al. (2006) and José & Shore (2008).

$$
\begin{aligned}
{}^{12}\mathrm{C} + \mathrm{p} &\longrightarrow {}^{13}\mathrm{N} + \gamma \ + 1.944 \ \mathrm{MeV} \\
{}^{13}\mathrm{C} + \mathrm{p} &\longrightarrow {}^{14}\mathrm{N} + \gamma \ + 7.551 \ \mathrm{MeV} \\
{}^{13}\mathrm{N} + \mathrm{p} &\longrightarrow {}^{14}\mathrm{O} + \gamma \ + 4.628 \ \mathrm{MeV} \\
{}^{13}\mathrm{N} + \gamma &\longrightarrow {}^{12}\mathrm{C} + \mathrm{p} \ - 1.944 \ \mathrm{MeV} \\
{}^{13}\mathrm{N} &\longrightarrow {}^{13}\mathrm{C} + \mathrm{e}^{+} + \nu_{\mathrm{e}} \ + 1.508 \ \mathrm{MeV} \\
{}^{14}\mathrm{N} + \mathrm{p} &\longrightarrow {}^{15}\mathrm{O} + \gamma \ + 7.297 \ \mathrm{MeV} \\
{}^{14}\mathrm{O} &\longrightarrow {}^{14}\mathrm{N} + \mathrm{e}^{+} + \nu_{\mathrm{e}} \ + 4.234 \ \mathrm{MeV}
\end{aligned}
$$

$$
\begin{array}{rcl}
{}^{14}\mathrm{O}+\gamma & \longrightarrow & {}^{13}\mathrm{N}+\mathrm{p}\ \ -4.628\ \mathrm{MeV}\\
{}^{15}\mathrm{N}+\mathrm{p} & \longrightarrow & {}^{12}\mathrm{C}+\alpha\ \ +4.966\ \mathrm{MeV}\\
{}^{15}\mathrm{N}+\mathrm{p} & \longrightarrow & {}^{16}\mathrm{O}+\gamma\ \ +12.128\ \mathrm{MeV}\\
{}^{15}\mathrm{O} & \longrightarrow & {}^{15}\mathrm{N}+\mathrm{e}^{+}+\nu_{\mathrm{e}}\ \ +1.757\ \mathrm{MeV}\\
{}^{16}\mathrm{O}+\mathrm{p} & \longrightarrow & {}^{17}\mathrm{F}+\gamma\ \ +0.600\ \mathrm{MeV}\\
{}^{17}\mathrm{O}+\mathrm{p} & \longrightarrow & {}^{18}\mathrm{F}+\gamma\ \ +5.607\ \mathrm{MeV}\\
{}^{17}\mathrm{O}+\mathrm{p} & \longrightarrow & {}^{14}\mathrm{N}+\alpha\ \ +1.191\ \mathrm{MeV}\\
{}^{17}\mathrm{F}+\mathrm{p} & \longrightarrow & {}^{14}\mathrm{O}+\alpha\ \ -1.193\ \mathrm{MeV}\\
{}^{17}\mathrm{F}+\gamma & \longrightarrow & {}^{16}\mathrm{O}+\mathrm{p}\ \ -0.600\ \mathrm{MeV}\\
{}^{17}\mathrm{F} & \longrightarrow & {}^{17}\mathrm{O}+\mathrm{e}^{+}+\nu_{\mathrm{e}}\ \ +1.892\ \mathrm{MeV}\\
{}^{18}\mathrm{F}+\mathrm{p} & \longrightarrow & {}^{15}\mathrm{O}+\alpha\ \ +2.877\ \mathrm{MeV}
\end{array}
$$

For each isotope i, the mass fraction X_i and the molar abundance Y_i are computed. At every timestep the code checks mass conservation:

$$\sum_{i=1}^{N} X_i = 1, \tag{A.35}$$

whereas the continuity equation for a given isotope fulfills the following expression:

$$\frac{dY_i}{dt} + \nabla \cdot (Y_i \mathbf{v_i}) = \sum_{j,k} Y_l Y_k \lambda_{kj}(l) - Y_i Y_j \lambda_{jk}(i) \tag{A.36}$$

The second term on the left-hand side represents the mass diffusion contribution. Mass diffusivity can be neglected, when compared to other processes, in regimes of small Prandlt number and large Lewis number. The Prandlt number measures the ratio of the viscous diffusion to the thermal diffusion contribution, while the Lewis number measures the ratio of thermal diffusion to mass diffusion. Taking this approximation into account, the mass-diffusivity term can be removed from the continuity equation, and only local processes contribute to composition changes:

$$\frac{dY_i}{dt} = \sum_{j,k} Y_l Y_k \lambda_{kj}(l) - Y_i Y_j \lambda_{jk}(i) \tag{A.37}$$

The term on the right-hand side of this equation represents the reaction rate contribution. We are taking into account the contribution of binary reactions, where $\lambda_{kj}(l)$ and $\lambda_{jk}(i)$ are the reverse and forward rates. To solve this set of differential ordinary equations, we first construct the jacobian matrix $\mathbf{J} = \partial \mathbf{f}/\partial \mathbf{y}$. This matrix is usually a sparse matrix, since most of the elements are zero. However, the coefficients in this matrix vary rapidly and significantly over a small timescale because of the strong dependence to temperature and density, and therefore, we have to solve a stiff set of ordinary differential equations. Because of this, one needs an accurate method to deal with this behavior, such as implicit or semi-implicit time integration methods. *FLASH* adopts the method described in Timmes (1999) to solve this system of ordinary differential equations. Specifically, the *GIFT* package is used, which works well with small nuclear networks (less than 30 isotopes) coupled to the variable order Bader-Deuflhard method (Bader & Deuflhard, 1983; Press et al., 1996). *GIFT* solves the system of equations ($\mathbf{Z} \cdot \mathbf{x} = \mathbf{y}$) using a Gaussian method of reduction to end up with an upper triangular matrix. Then the solution is found by back-substitution.

The variable order Bader-Deuflhard method will evolve the network ($\dot{\mathbf{y}} = \mathbf{f}(\mathbf{y})$) to find the next value $\mathbf{y}_{n+1}$, advancing the stage $\mathbf{y}_n$ over a large time step H (which is splitted in m sub-time steps) as follows:

$$h = H/m \tag{A.38}$$

$$(\mathbf{1} - \mathbf{J}) \cdot \Delta_0 = h \ \mathbf{f}(\mathbf{y}_n) \tag{A.39}$$

$$\mathbf{y}_1 = \mathbf{y}_n + \Delta_0 \tag{A.40}$$

and for $k = 1, 2, ..., m - 1$,

$$(\mathbf{1} - \mathbf{J}) \cdot \mathbf{x} = h \ \mathbf{f}(\mathbf{y}_k) - \Delta_{k-1} \tag{A.41}$$

$$\Delta_k = \Delta_{k-1} + 2\mathbf{x} \tag{A.42}$$

$$\mathbf{y}_{k+1} = \mathbf{y}_k + \Delta_k \tag{A.43}$$

obtaining in the last stage,

$$(\mathbf{1} - \mathbf{J}) \cdot \Delta_m = h \ \mathbf{f}(\mathbf{y}_m) - \Delta_{m-1} \tag{A.44}$$

$$\mathbf{y}_{n+1} = \mathbf{y}_m + \Delta_m \tag{A.45}$$

This sequence is repeated at least twice with different values for the sub-time step m until sufficient accuracy is found. This method is expensive, but also very accurate, and since it allows to step over a large time step, its usage is efficient. Very precise time integration methods will keep its accuracy below hydrodynamical algorithm accuracy, so that numerical errors that arise from network algorithms are not dominant (Fryxell et al., 2000). Finally, over every timestep, the code will update the abundances and evaluate the contribution of the energy release as follows:

$$\dot{\epsilon}_{\mathrm{nuc}} = N_{\mathrm{A}} \sum_i B_i \frac{\Delta Y_i}{\Delta t} \tag{A.46}$$

where B_i is the nuclear binding energy. Then, the nuclear energy contribution $\epsilon_{\rm nuc}$ can be incorporated into the equation of energy conservation, to obtain:

$$\frac{\partial \rho E}{\partial t} + \nabla \cdot (\rho E + P)\mathbf{v} = \rho \mathbf{v} \cdot \mathbf{g} + \nabla \cdot \mathbf{F}_{\rm heat} + \epsilon_{\rm nuc}(X_i, \rho, T) \tag{A.47}$$

The following expression gives an estimate of the nuclear burning timescale:

$$\tau_{\rm burn} \propto \frac{\epsilon_{\rm int}}{\dot{\epsilon}_{\rm nuc}} \tag{A.48}$$

This timescale is $\sim 10^{\ 4}$ s when the temperature is $\sim 7\times\ 10^7$ K, but it drops to a few seconds when the temperature is $\sim 10^8$ K (Glasner & Livne, 2002; Glasner et al., 1997). In our simulations, this timescale is about 10^3 s at the beginning of the simulation and decreases to ~ 5 s — a value much larger than the hydrodynamical timestep — during the fully developed burning stage at the end of the simulation.

A.6 Gravitational field

The *FLASH* code can implement either externally applied gravitational fields (constant gravitational field, plane-parallel gravitational field and point-mass gravitational field) or self-gravity algorithms that solve the Poisson equation. Since the computed slice is not very large we have adopted a constant gravitational field in our simulations. The typical adopted domain is 800 × 800 km for most of the simulations in 2-D and 800 × 800 × 800 km for the 3-D simulation. Finally, the adopted domain for model G (see Chapter 3) is 800 × 1000 km, which is still not very large. The gravitational field is applied along the radial direction and its value is set to $g = -6.32 \times 10^8$ cm s^{-2}.

Appendix B

Hydrodynamical tests

FLASH is a sophisticated code that has been already verified and validated (Fryxell et al., 2000; Calder et al., 2002b). In particular, it has been developed to study several astrophysical phenomena in the context of stellar explosion, such as type Ia supernovae, type I X-ray bursts or classical novae. It proved useful to tackle complex fluid dynamics phenomena, when convection, shocks or dynamical instabilities are involved. We have tested the code to get familiar with its capabilities and limitations, solving several fluid dynamics problems, and comparing the results with the analytical solutions, if existing, or with other simulations performed with different codes. The suite of hydrodynamical tests performed allow us to test specific units within *FLASH*, such as the adopted equation of state, gravity, or the combustion unit.

B.1 The advect problem

Advection tests show the ability of a code to handle both narrow and sharp structures such as contact discontinuities. Advection problems have been analyzed by Boris & Book (1997), Forester (1977) and Zalesak (1978), among others. This test consists in creating a pulse which is advected through the computational domain. The code has to keep the pulse shape as it moves. We have assumed both a square and a gaussian pulse. In both cases, the adopted pulse width is 0.1 cm and the computational domain consists of a box of 8 units length (that is, 8×8 cm). The pressure is 1 dyn cm^{-2} everywhere and the pulse is advected at a speed of 10 cm s^{-1}. We have analyzed the results after 0.4 s, that is, when the pulse is in the middle of the box. For the square pulse, the density is set to 1 g cm^{-3} within the pulse. For the gaussian pulse, the density within the pulse decays as $1 \cdot \exp(-x^2)$, where x is the distance to the center of the pulse, but scaled to its width. We have performed the test by using the perfect gas equation of state with $\gamma = 1.4$. The exact solution is a pulse that does not change in shape as it moves along the domain.

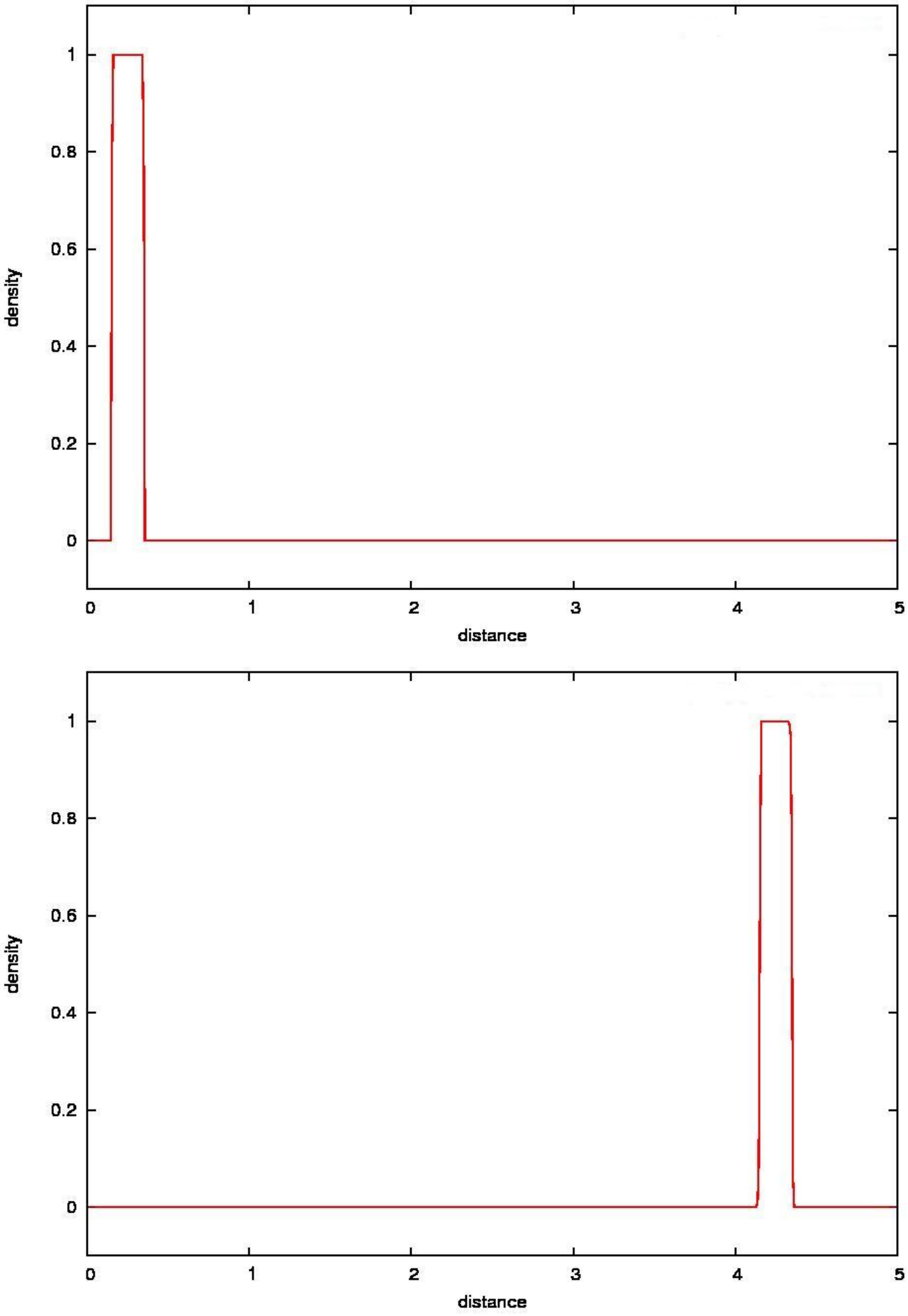

Figure B.1: Square pulse at $t = 0$ s (upper panel) and $t = 0.4$ s (lower panel) with 8 levels of refinement. The code is able to reproduce fairly well the sharp discontinuities and the pulse strength as time goes on.

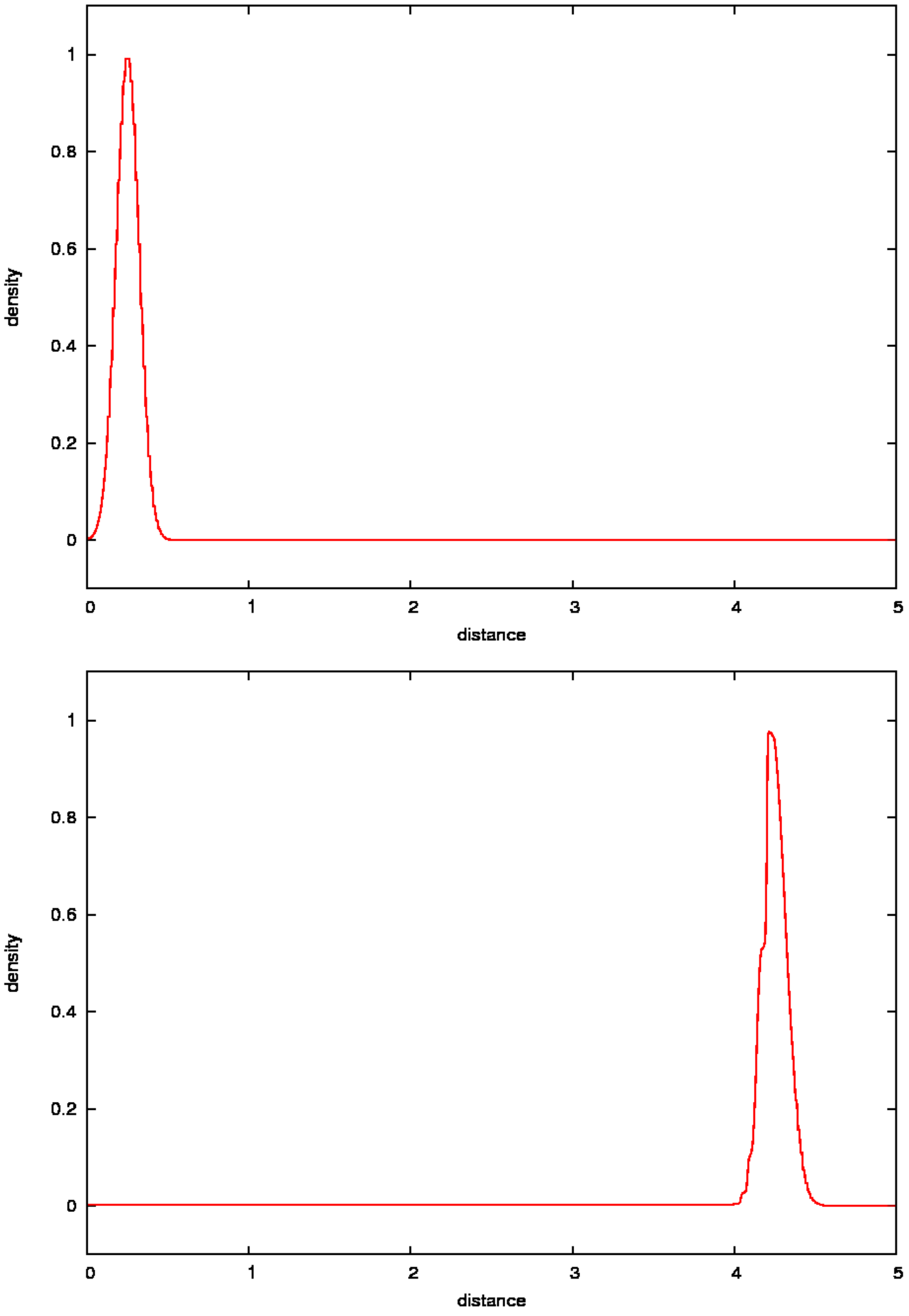

Figure B.2: Gaussian pulse at $t = 0$ s (upper panel) and $t = 0.4$ s (lower panel) with 8 levels of refinement. Although the code is able to reproduce fairly well the pulse shape at the beginning of the simulation, it fails as the pulse advances since the amplitude of the pulse is somewhat lower at the end. At this time, the code starts having difficulties to describe the gaussian profile in the trailing edge. Nevertheless, the code captures the narrow profile quite well.

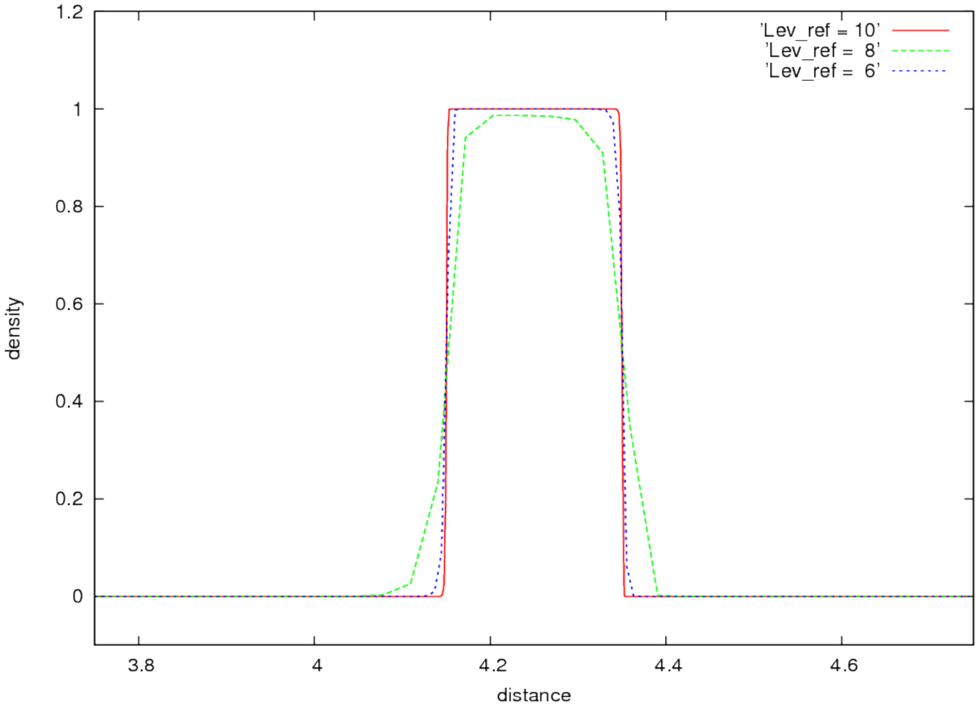

Figure B.3: Square pulse solution for the advect problem at $t = 0.4$ s for different levels of refinement (6, 8 and 10). The snapshot of the density profile shows clearly how decreasing the level of refinement results in a very coarse shape. For low refinements, the code tends to broaden the borders, flatten the shape and clip the pulse.

For the square pulse, the simulation has used 8 levels of refinement, and therefore the resolution is 0.0078 cm. At this level of refinement the code can capture the sharp discontinuities all along the domain and resproduce fairly well the planar geometry as time passes (see Fig. B.1). For the gaussian pulse, we have adopted the same pulse width and used 8 levels of refinement that also translates into a resolution of 0.0078 cm. As can be seen in Fig. B.2, the shape and height is mantained, but a small amount of diffusion appears and accumulates behind the pulse at the end.

In order to understand how good is the code at dealing with numerical diffusion, we have performed two additional simulations for the square pulse but with 10 and 6 levels of refinement. As shown in Fig. B.3, using less levels of refinement translates into an inaccurate shape of the pulse. Numerical difussion tends to broaden the discontinuities as they move and produces numerical noise at the front and the back of the pulse. When the resolution is not high enough, the code tends to deform the structure, smooth the corners and reduce the intensity of the pulse. However, a good choice of the level of refinement (i.e., 10) will give a good treatment of contact discontinuities and narrow features. It is worth noting that the *FLASH* code can

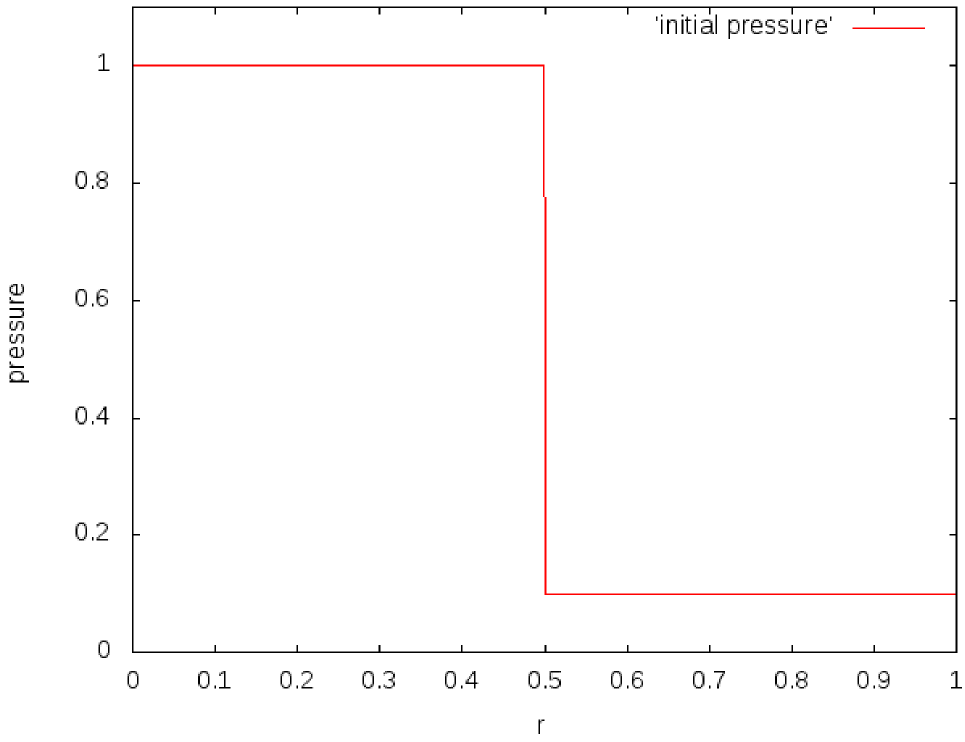

Figure B.4: Initial setup for the Sod shock tube test. The density profile looks very similar.

implement a procedure that steepens the contact discontinuities and does not allow them to spread in more than 1 or 2 zones.

B.2 The Sod shock tube

The Sod shock tube problem (Sod, 1978) is designed to test the ability of the code to handle strong shocks and contact discontinuities. The Sod test involves shock structures such as detonation and rarefaction waves, which a hydrodynamical code should be able to capture. The Sod shock problem is an example of a Riemann problem. For this test, we adopted a fluid at rest in a box 1×1 cm, that is initialized with a pressure and density jump in the middle of the domain ($x = 0.5$ cm). The pressure is set to 1 dyn cm^{-2} and the density to 1 g cm^{-3} at the left-hand side, and to 0.1 dyn cm^{-2} and 0.125 g cm^{-3}, respectively, at the right-hand side (see Fig. B.4). We have performed the simulation with 6 levels of refinement and 7 blocks per axis, with a resolution of 0.00056 cm. We have used a perfect gas equation of state with $\gamma = 1.4$. The simulation is performed in two dimensions and the boundary conditions are set to outflow at all sides, so that the shock wave will flow off the domain once

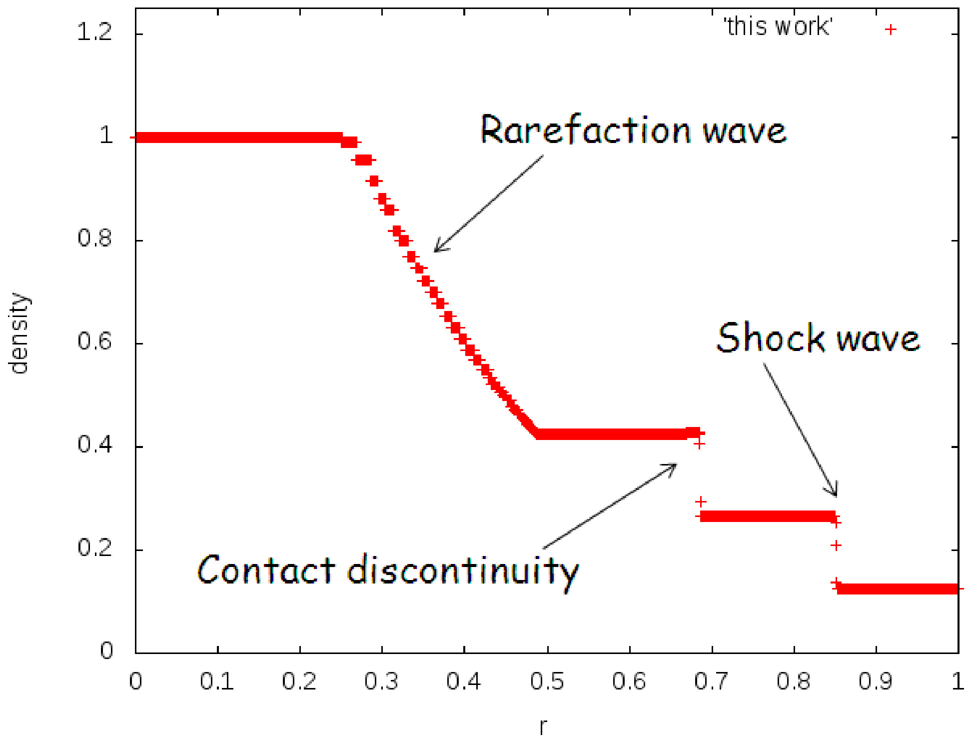

Figure B.5: Density profile at $t = 0.2$ s for the shock tube test. The initial conditions evolve into a complicated structure formed by a shock wave, a contact discontinuty and a rarefaction wave. In this figure it can be seen how the code is able to capture these 3 regions without introducing much oscillations behind the shocks.

it hits the wall. The problem has an analytical solution, which is given by solving the corresponding Riemann problem. As time passes, we follow the evolution of the fluid. The initial conditions result in a formation of a shock wave (at $x \sim 0.86$ cm) that moves to the right, and a rarefaction wave ($0.27 < x < 0.49$) that moves backwards. Between these shock structures, we notice the presence of a contact discontinuity at $x \sim 0.69$ cm. Therefore, as also found in the analytical solution, in our simulation (see Figs. B.5 and B.6) we can clearly distinguish 3 regions. In the contact discontinuity, the pressure and the normal velocity are continuous, but at the positions of the shocks all the magnitudes present discontinuities. The analytical solution relies on the Runkine-Hugoniot conditions near the shock wave, and hence, we are also testing the ability of the code to reproduce these conditions properly.

As shown in Figs. B.5 and B.6, the code is able to correctly reproduce the shock, the rarefaction waves and the contact discontinuity, while keeping these discontinuities sharp and decomposing the initial structure into the mentioned resolved

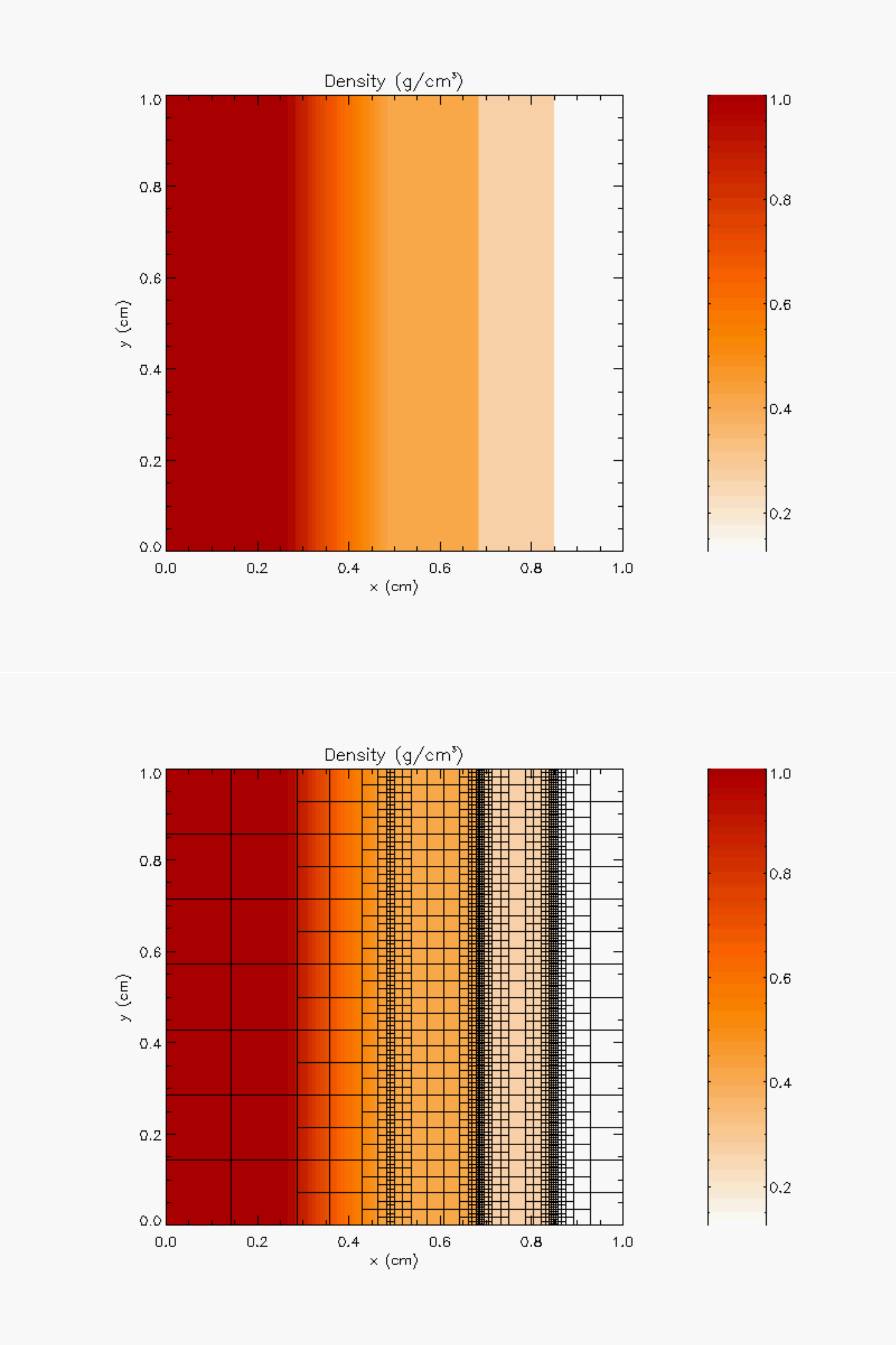

Figure B.6: Snapshots of the density at $t = 0.2$ s for the shock tube test, clearly showing the regions predicted theoretically. In the lower panel it is shown how the code administers more blocks around the discontinuities to capture them properly.

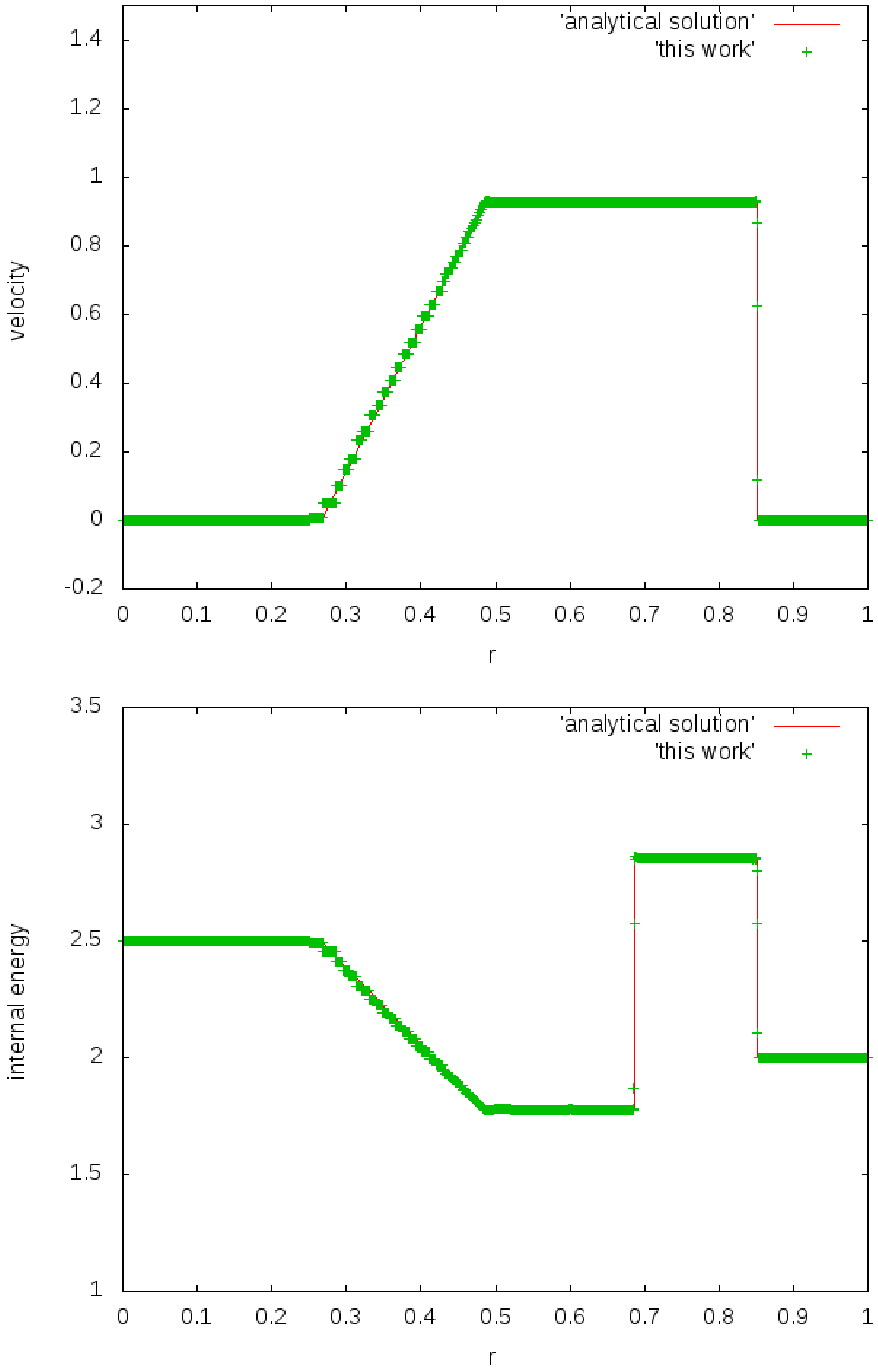

Figure B.7: Comparison of the velocity (upper panel) and the pressure (lower panel) at $t = 0.2$ s with the analytical solution for the shock tube problem. The code can reproduce the detailed structures, keeping them sharp and correctly reproducing its evolution.

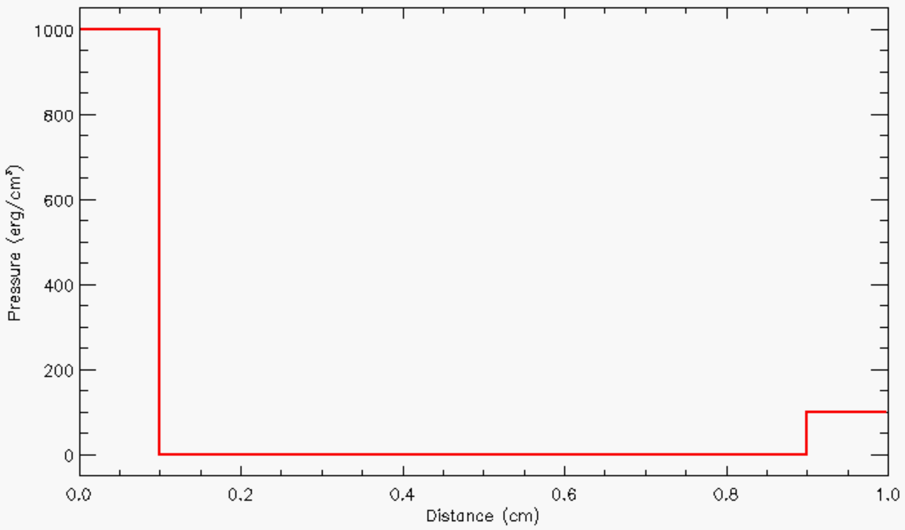

Figure B.8: Initialization pressure setup for the two blast problem.

regions. The code is also able to capture the structures and describe properly the regions behind the shocks, since we cannot appreciate postshock oscillations. Near the positions of the shock and the contact discontinuity the adaptive mesh refinement procedure acts, refining the regions that need special attention (bottom panel of Fig. B.6). Results obtained with the *FLASH* code fit well the analytical solution (see Fig. B.7, for the velocity and the internal energy), capturing correctly the sharp discontinuities and the postshock regions, so we conclude that the code can describe the Sod shock tube accurately.

B.3 The two-blast wave problem

The Woodward-Colella blast-wave problem tests the ability of the code to capture very strong shocks and complex structures, such as those formed when two blast waves collide. This test was first performed by Woodward & Colella (1984) and it is based on the Sod shock tube test. For this test, two strong pressure jumps were generated at $x = 0.1$ cm and $x = 0.9$ cm. We have run the test in one dimension, with a computational domain of 1 cm. The density is set to 1 g cm^{-3}

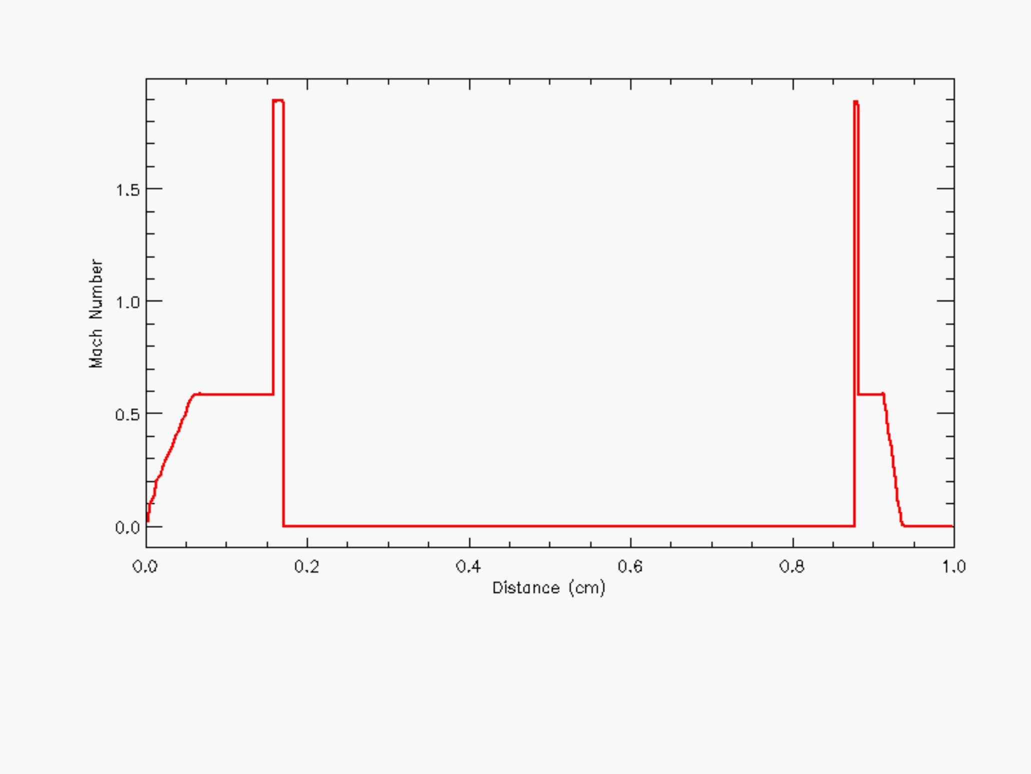

Figure B.9: Snapshot of the Mach number at $t = 0.003$ s showing the formation of two blast waves that propagate supersonically.

everywhere. The pressure at both sides of the interval are set to 1000 dyn cm^{-2} (left) and 100 dyn cm^{-2} (right). Between these two pressure jumps, the adopted pressure is 0.01 dyn cm^{-2} (see Fig. B.8). We use the equation of state of a perfect gas to model the two blast problem, with $\gamma = 1.4$, and reflect boundary conditions at both sides. We have used 12 levels of refinement with a resolution of 6.1 $\times 10^{-5}$ cm.

Once the simulation starts, two strong shock waves that move supersonically immediately form (see Fig. B.9). These two shocks move towards the center of the grid, while two rarefaction waves are born behind and head to the walls. Between each shock wave and its corresponding rarefaction wave, a contact discontinuity at both sides ($x_1 \sim 0.29$ cm and $x_2 \sim 0.84$ cm for $t = 0.01$ s) — see the lower panel of Fig. B.10 — is found. The rarefaction wave born in the left side of the computational domain travels faster and is reflected after hitting the wall. In turn, this reflected wave follows and catches the initial blast wave, distorting and smoothing its structure (see the bottom panel of Fig. B.10 and the top panel of Fig. B.11). A similar behavior is found for the rarefaction wave born in the right side, but catching the

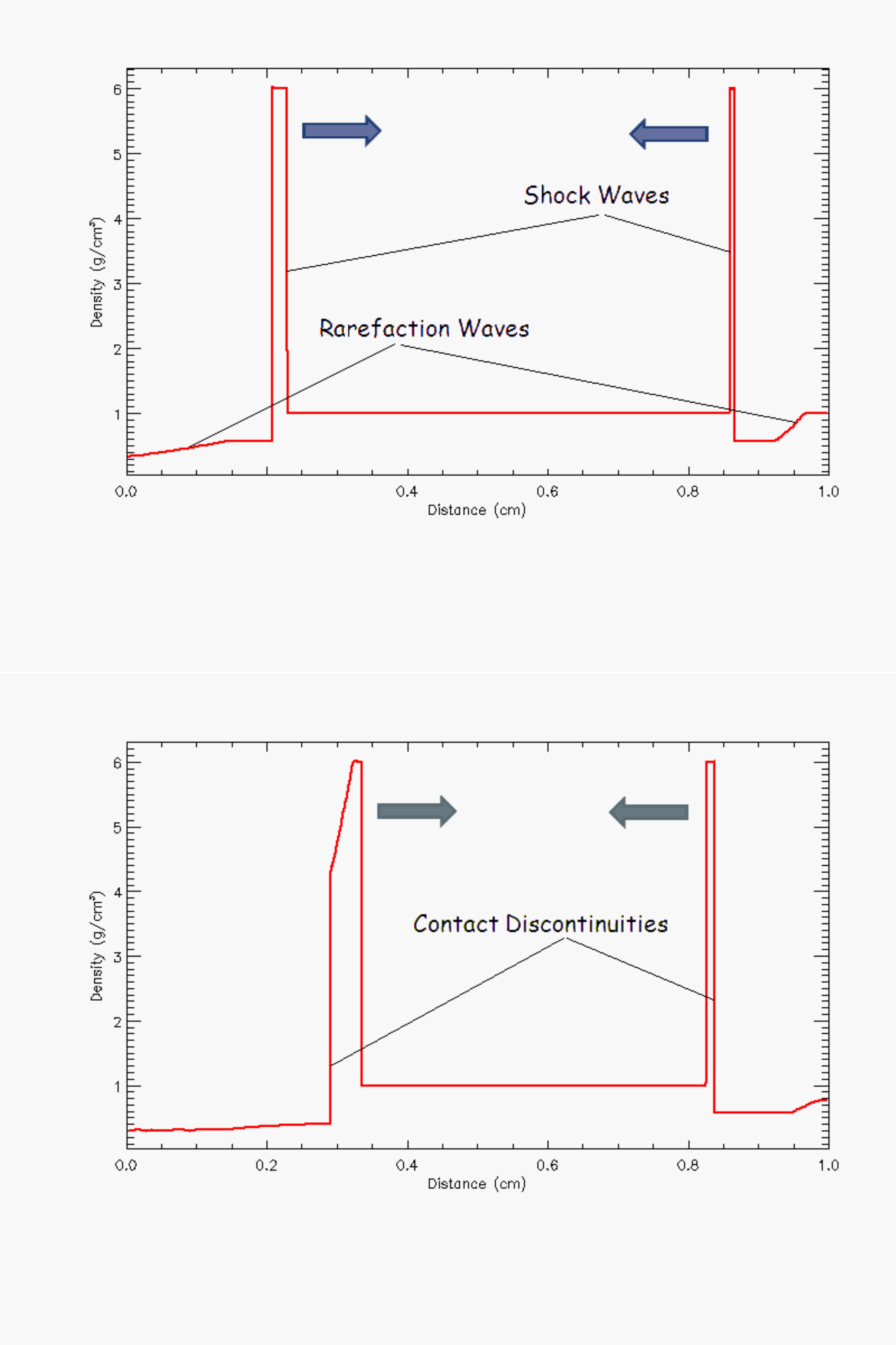

Figure B.10: Evolution of the two blasts at $t = 0.006$ s (upper panel) and $t = 0.010$ s (lower panel).

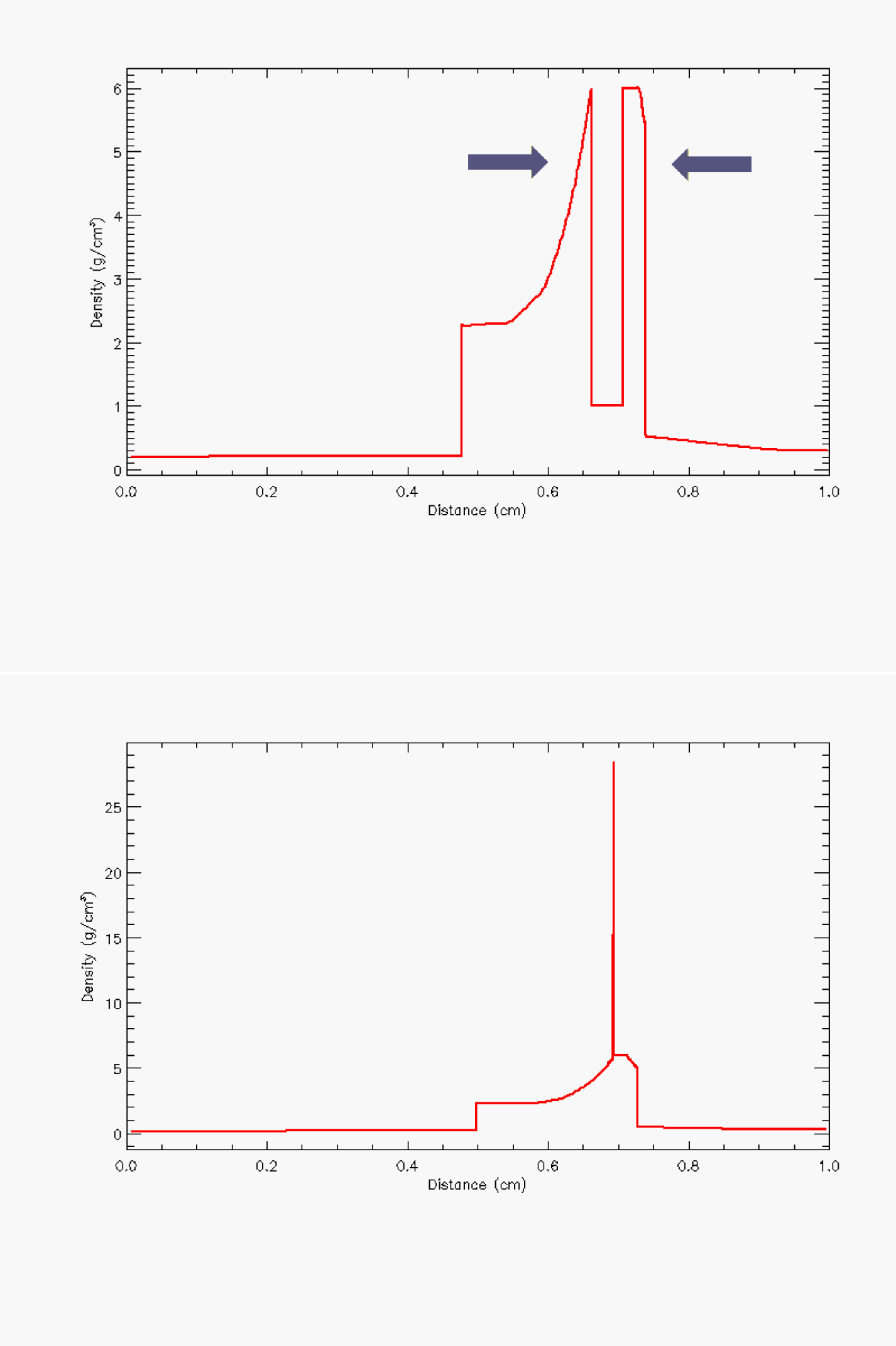

Figure B.11: Same as Fig. B.10, but for $t = 0.026$ s (upper panel) and $t = 0.028$ s (lower panel). The snapshots show now the two blasts colliding and producing a density peak.

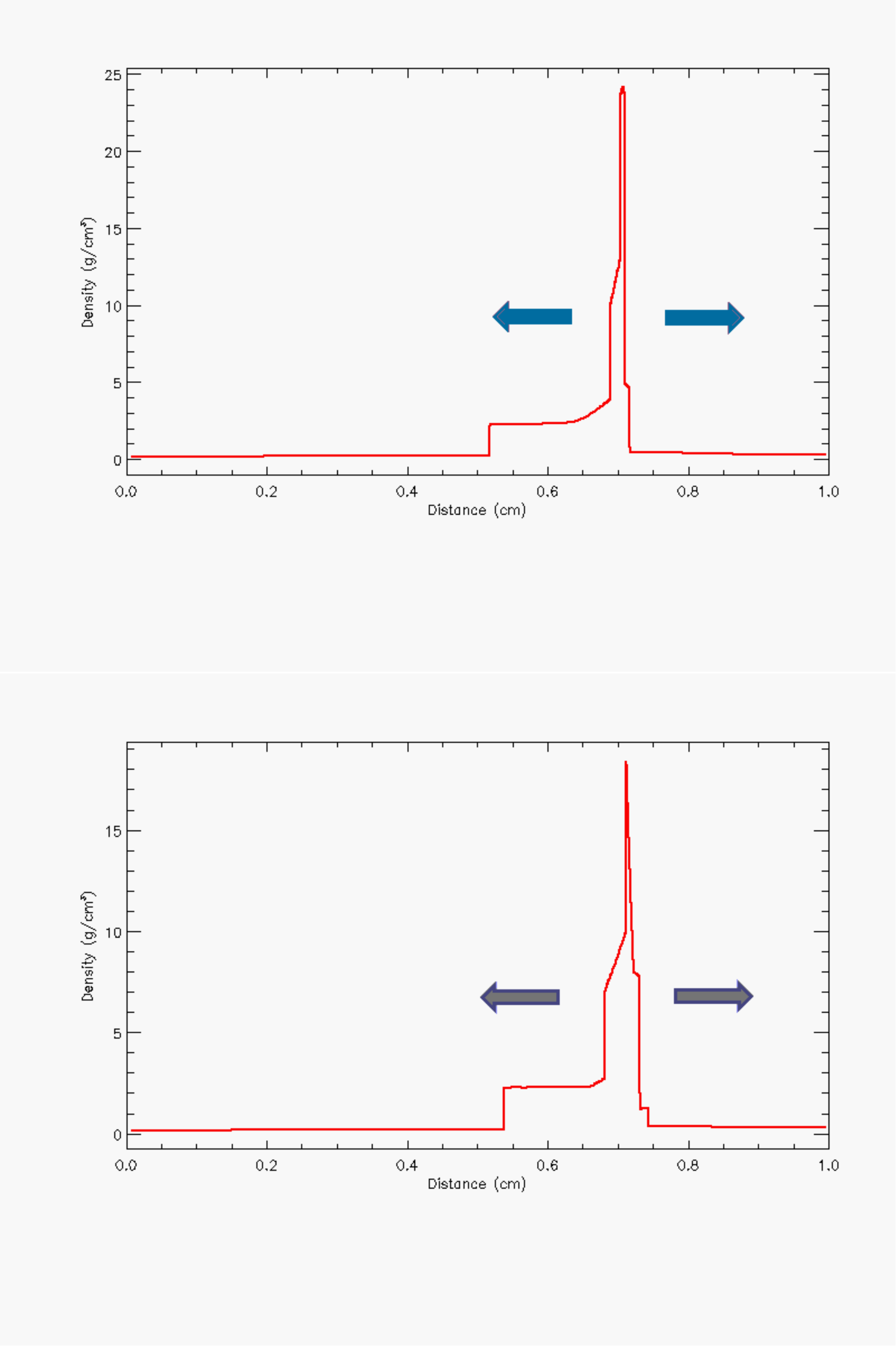

Figure B.12: Same as Fig. B.10, but for $t = 0.030$ s (upper panel) and $t = 0.032$ s (lower panel).

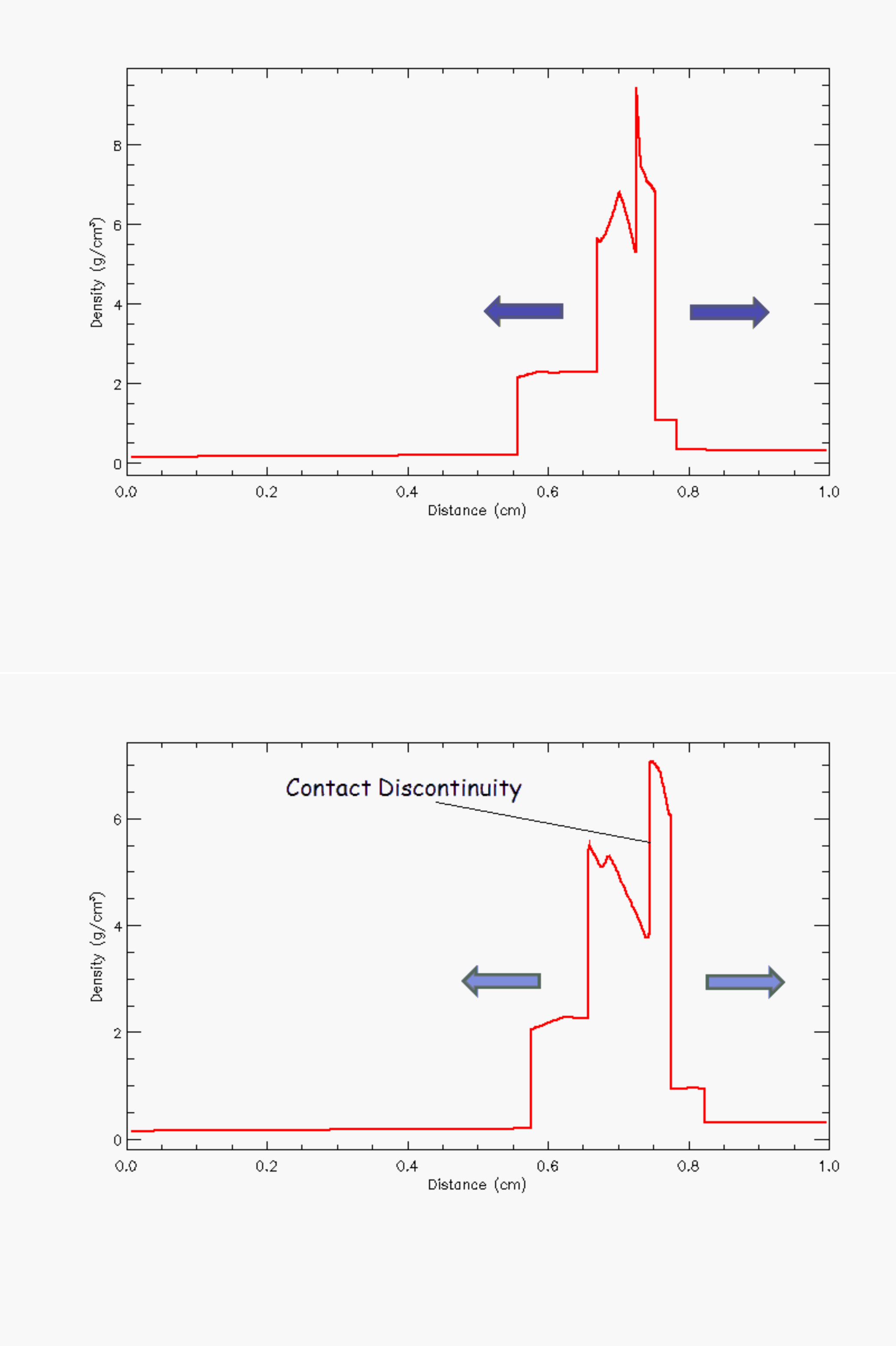

Figure B.13: Same as Fig. B.10, but for $t = 0.034$ s (upper panel) and $t = 0.036$ s (lower panel). The snapshots show the two reflected shock waves from the collision heading back to the walls.

corresponding blast wave at a later time, $t = 0.026$ s, because the softer pressure jump creates a weaker rarefaction wave (upper panel of Fig. B.11). At $t = 0.028s$ the two blasts collide at $x \sim 0.68$ cm. The collision produces a density peak that reaches 29 dyn cm^{-2} (see Fig. B.11 — lower panel). After the collision, at $t = 0.034$ s, the two shock waves are reflected and start moving to the left and right (Figs. B.12 and B.13). Where the two waves collide, a contact discontinuity is formed (Fig. B.13).

The two blast-wave problem does not have an analytical solution, but our results can be compared with the ones obtained by Woodward & Colella (1984), with a PPM scheme. The collision is produced at the same time ($t = 0.028$ s) and the peak density approximately reaches the same value in both simulations. The evolution of all the structures involved (contact discontinuities, rarefaction and shock waves) agree with those found in Woodward & Colella (1984). Therefore, the *FLASH* code is able to reproduce situations that involve strong shocks or narrow and complex structures, such as the ones presented in this test.

B.4 The Shu-Osher problem

The Shu-Osher problem tests the ability to capture subtle flow patterns and to handle problems that involve shock waves. Shock-capturing schemes need to treat shock waves accurately, since oscillations can appear just behind the shock. Introducing numerical dissipation can prevent these oscillations to form. Therefore, the Shu-Osher problem is also testing the dissipation method that the *FLASH* code is using. This problem was initially studied by Shu & Osher (1989) and consists of a fluid which is initially at rest, with an initial pressure $p = 1$ dyn cm^{-2} and a sinusoidal density flow given by

$$\rho = \rho_0 \left(1 + a_0 \cdot \sin\left(f_0 \cdot x\right)\right), \tag{B.1}$$

where $\rho_0 = 1$ g cm^{-3}, $a_0 = 0.2$ cm and $f_0 = 5$ cm^{-1}. The wavelength ($\lambda = \frac{2\pi}{f_0}$)is ~ 1.25 cm. We use an ideal gas with $\gamma = 1.4$ and the simulation is performed in one dimension with a uniform grid. The size of the computational domain is $-4.5 < x < 4.5$. At $x < -4$ cm, we introduce a shock wave by setting the density, pressure and velocity to the following values: $\rho = 3.86$ g cm^{-3}, $p = 10.33$ dyn cm^{-2} and $v = 2.63$ cm s^{-1} — see Figs. B.14 and B.15. At the left side, we fix the values exactly to the initial ones (boundary condition), but we set an outflow condition at the right side instead (that is, the shock would flow off the grid). The number of cells administered is 16 000, with a resolution of 5.625×10^{-4} cm. After setting the initial values, a shock wave is formed, moving to the right and entering the sinusoidal density field. As it was found by Shu & Osher (1989), behind the shock wave density starts oscillating, but with the appearance of higher frequency pulsations right behind the incident front — see the upper panel of Fig. B.16. These oscillations do not arise from the noise that appears behind sharp shocks, but result

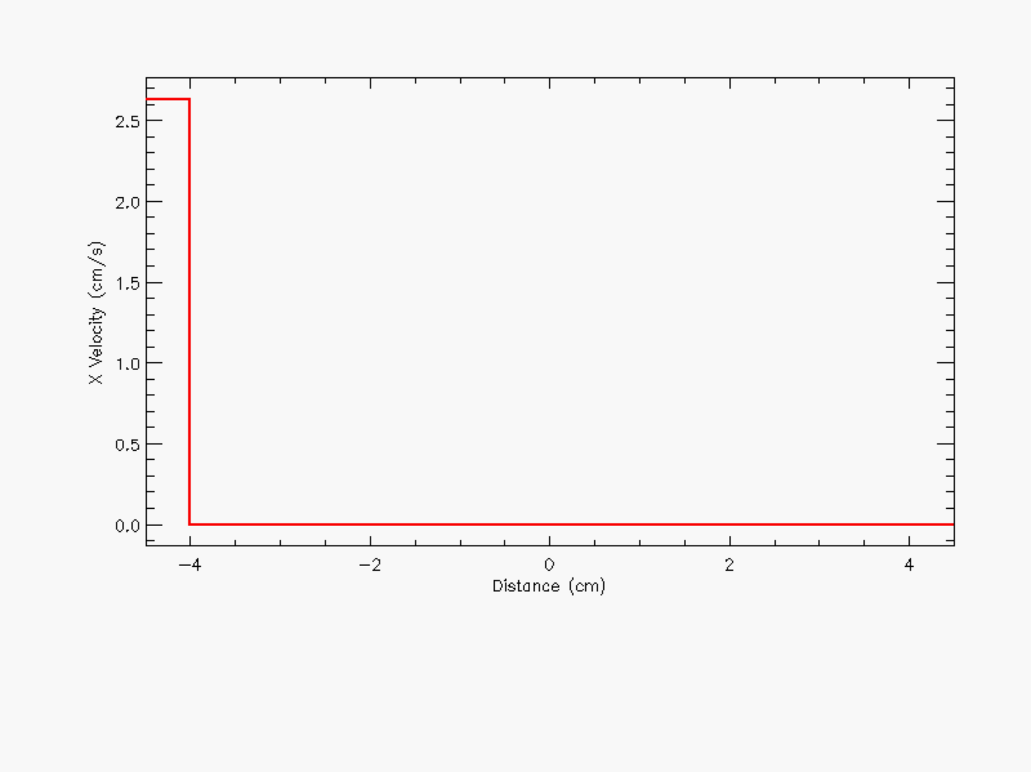

Figure B.14: Initial velocity along the x-axis for the Shu-Osher problem. The shock wave will sweep the domain with Ma$\sim$ 1.36.

from the dynamics of the problem. The *FLASH* code is able to reproduce the same solution found by Shu & Osher (1989), since it can describe accurately the post-shock oscillations, specially when the resolution is high enough — see the upper panel of Fig. B.16. For coarser resolutions, the code is not able to capture the exact density profile. To prove this, we have also performed the same simulation, but with only 160 cells and a resolution of 5.625×10^{-2} cm. When the accuracy is not good, the code cannot resolve the subtle oscillations behind the shock, since it underestimates their intensity and shape (lower panel of Fig. B.16). Thus, with this test we have corroborated that the *FLASH* code is able to resolve subtle flow patterns when resolution is high enough and to handle detailed structures behind shocks.

B.5 The wind tunnel problem

The wind tunnel problem was first introduced by Emery (1968) and tests the ability of the code to deal with strong shocks and complex structures. It consists of imposing

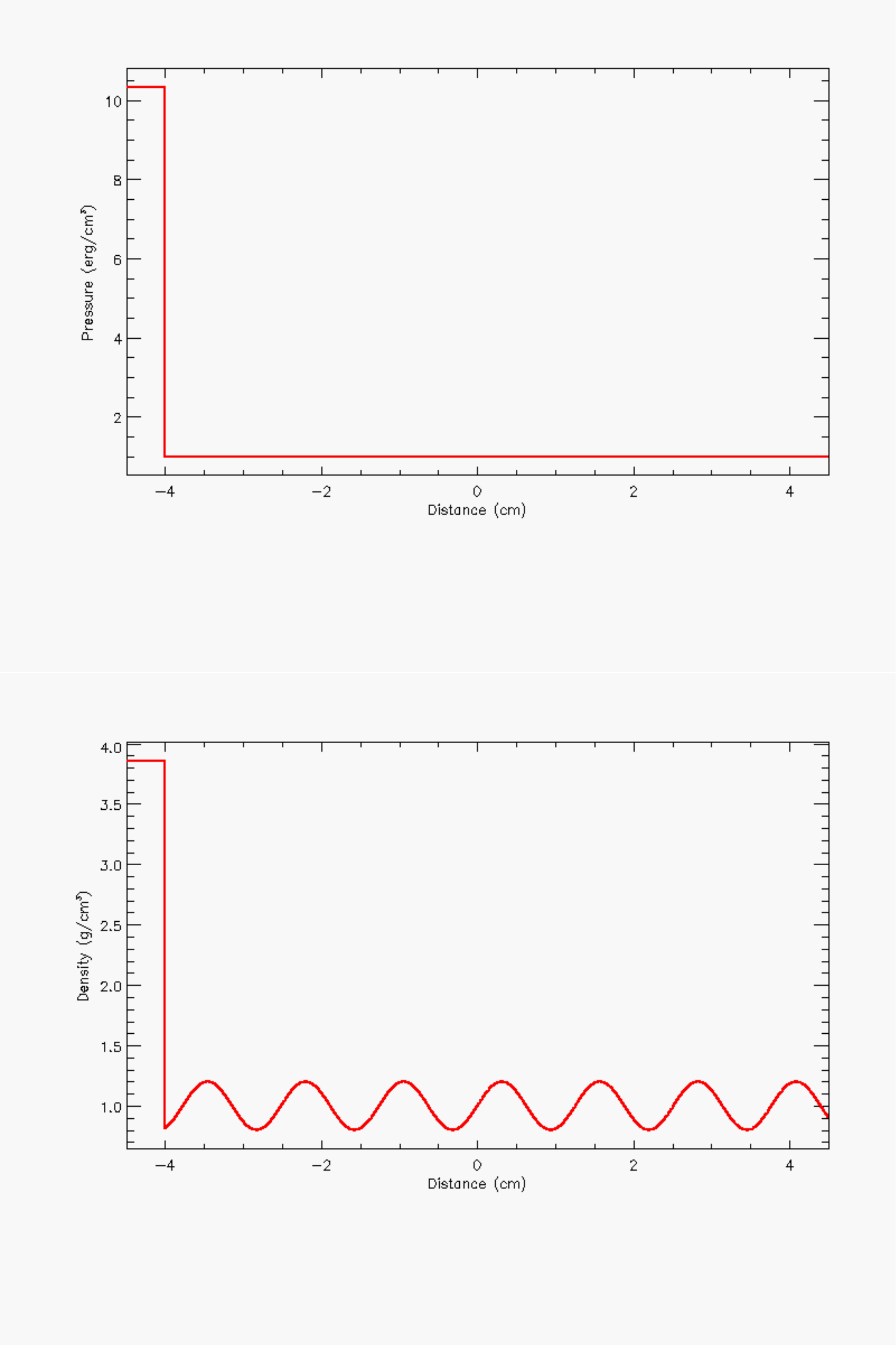

Figure B.15: Initial values for pressure (upper panel) and density (lower panel) for the Shu-Osher problem. The shock wave will enter an imposed sinusoidal density field at $x > -4$ cm.

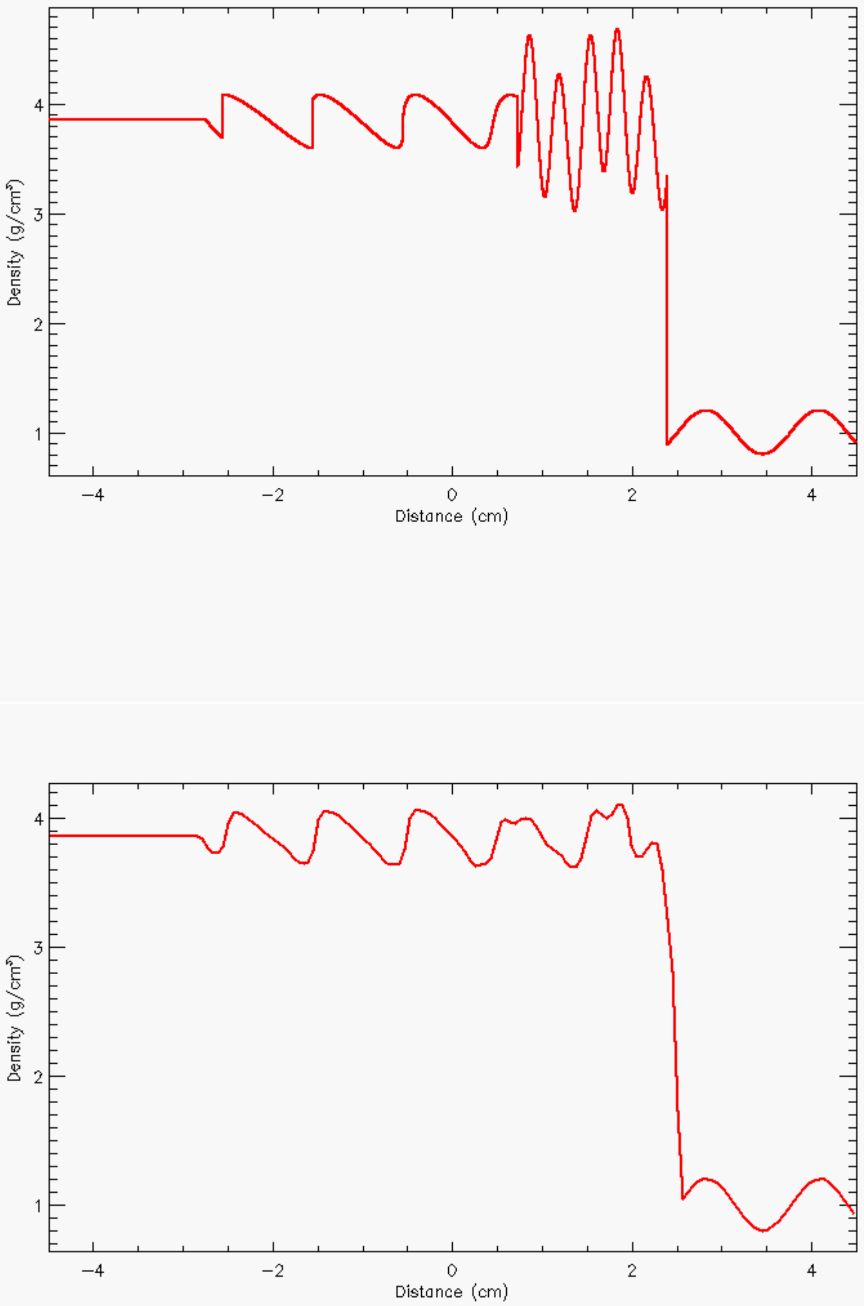

Figure B.16: Density profiles for the Shu-Osher problem at $t = 1.8$ s. The upper panel corresponds to the simulation with higher resolution, where postshock oscillations are resolved. The lower panel corresponds to a coarser resolution that makes the code underestimate the strength and shape of the oscillations.

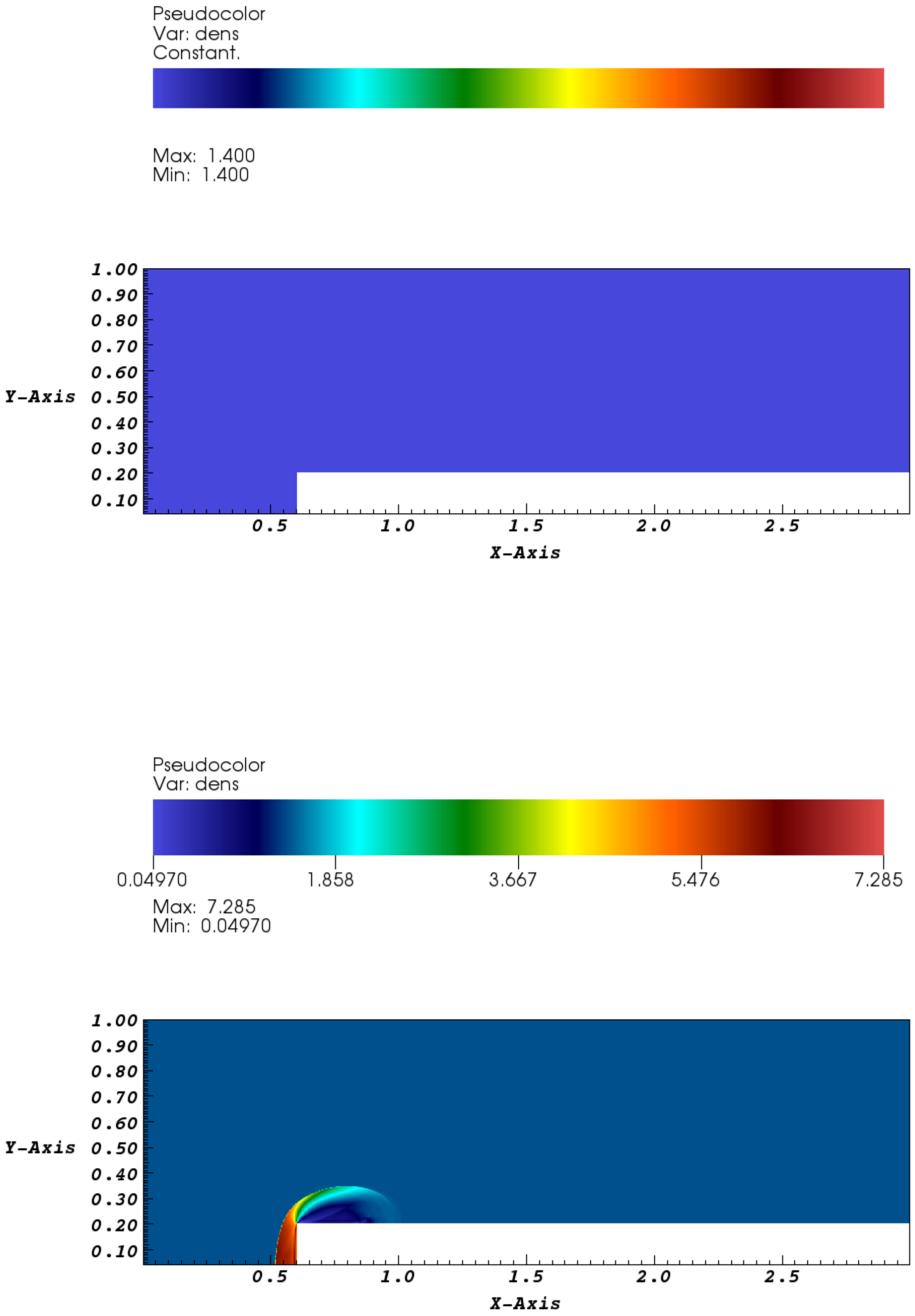

Figure B.17: Evolution of the wind profile (density field) at $t = 0$ s (upper panel) and $t = 0.1$s (lower panel), for the wind tunnel test.

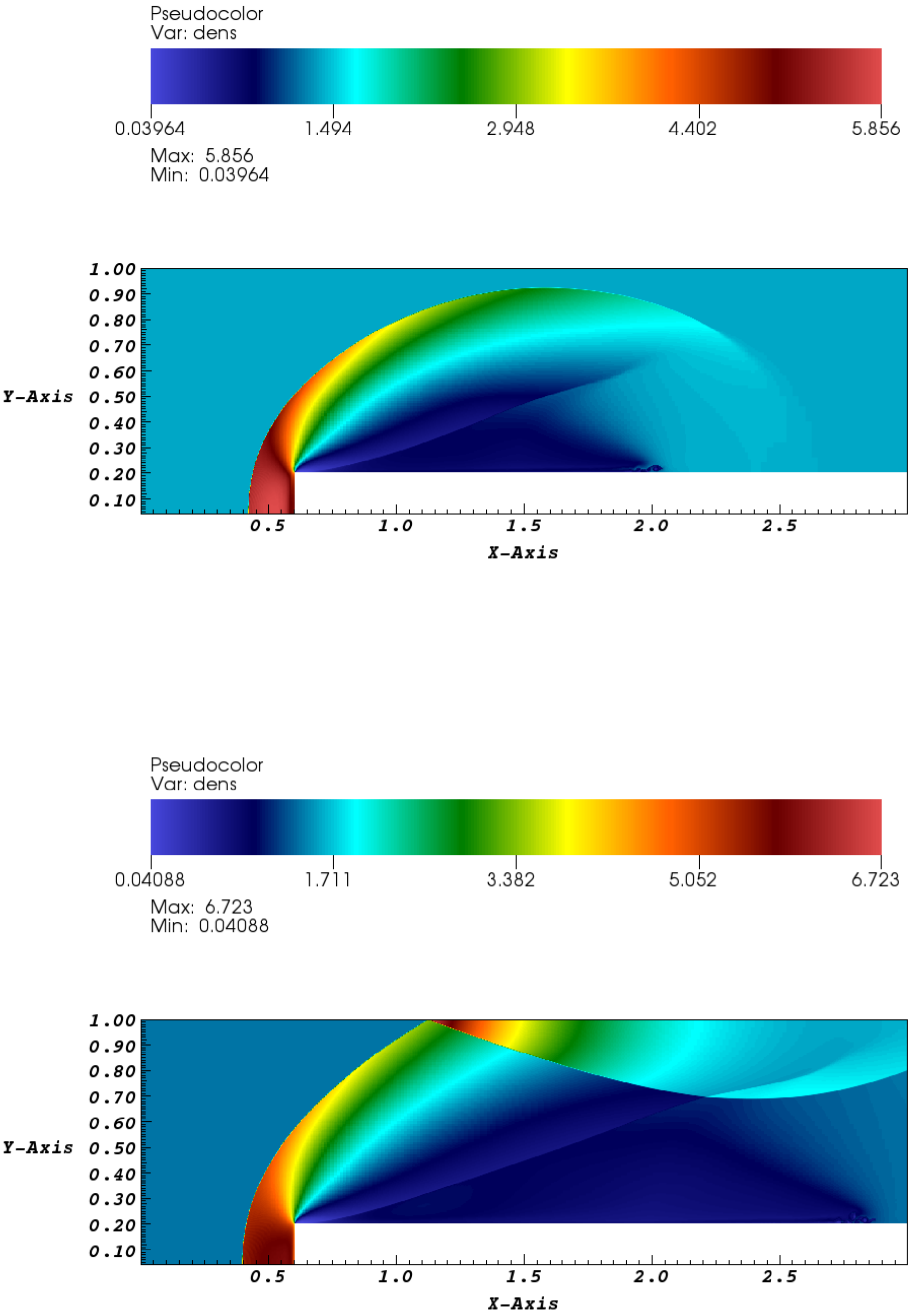

Figure B.18: Same as Fig. B.17, but at $t = 0.5$ s (upper panel) and $t = 0.8$ s (lower panel). In the lower panel the first reflection point can be seen at the top of the panel.

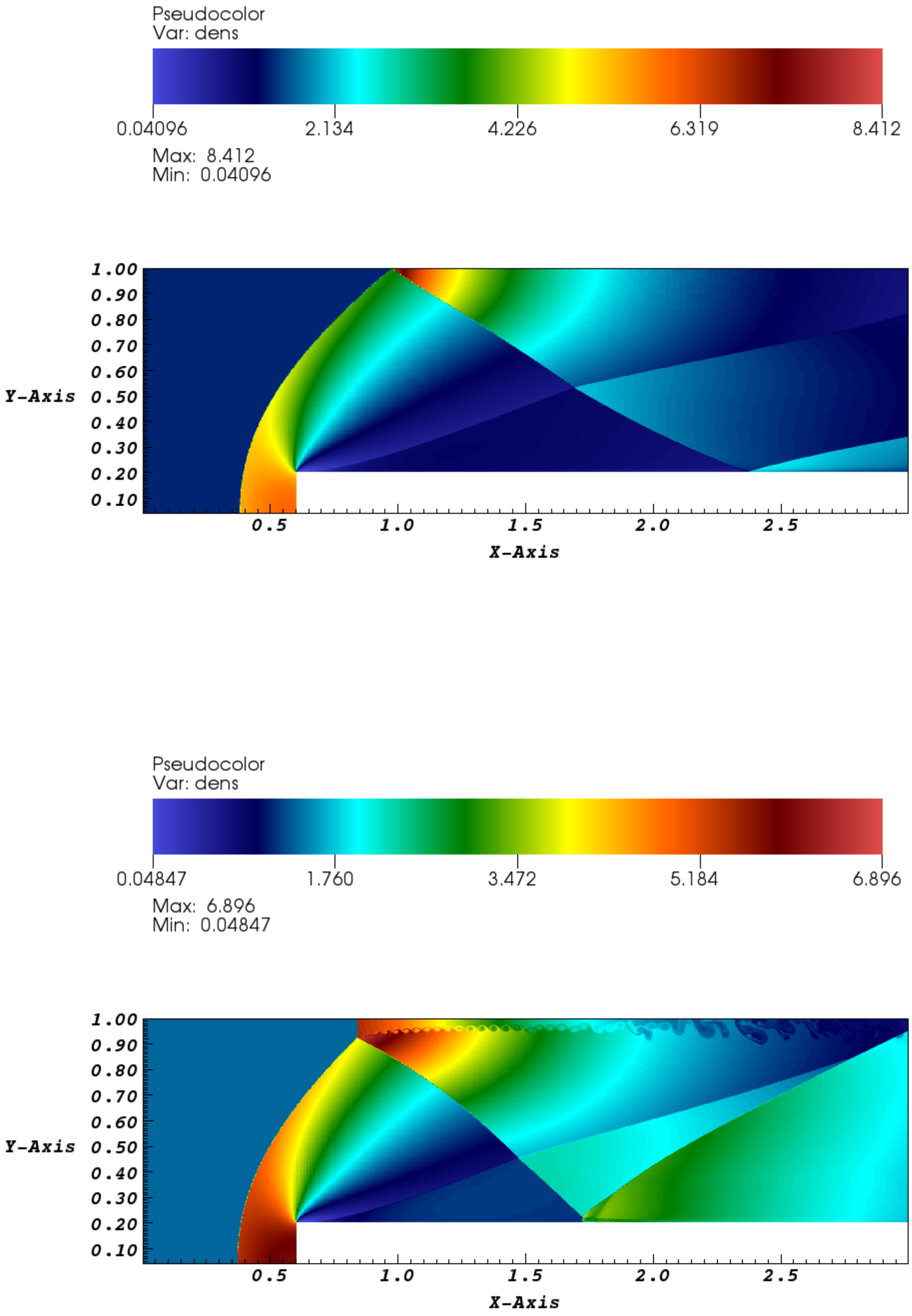

Figure B.19: Same as Fig. B.17, but at $t = 1.3$ s (upper panel) and $t = 2.6$ s (lower panel). The upper panel shows the second reflection point at the step, while the lower panel shows the formation of the Kelvin-Helmholtz instabilities at the Mach stem.

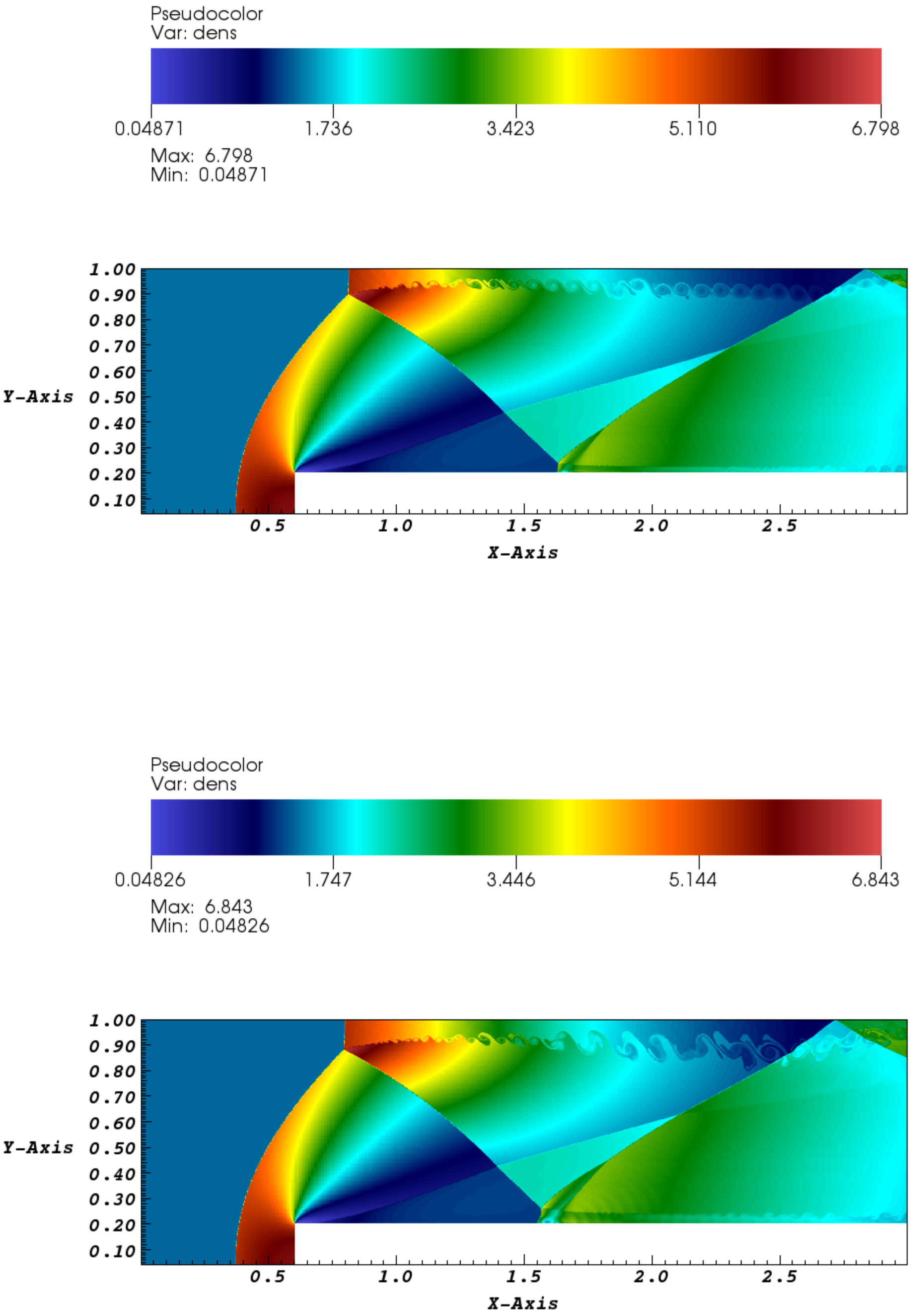

Figure B.20: Same as Fig. B.17, but at $t = 3.3$ s (upper panel) and $t = 4$ s (lower panel). Both panels show the layer formed over the step surface that might accelerate the formation of the second Mach stem. Furthermore, Kelvin-Helmholtz instabilities can be appreciated at the end of the step in both snapshots.

a wind profile in the domain. We have performed the test in two dimensions, using a rectangular box of dimensions 3 × 1 cm. From $x = 0.6$ cm to the end of the grid we impose a 0.2 cm high step. We have administered 15 blocks along the x axis and 5 along the y axis to impose the same resolution in both directions. Furthermore, we have used 5 levels of refinement and, therefore, a resolution of 0.0016 cm. At the left-hand wall, and as a boundary condition, we impose a horizontal wind profile, which moves towards the step at a speed of 3 cm s^{-1}. Since the fluid density is set to 1.4 g cm^{-3}, the fluid pressure to 1 dyn cm^{-2} and $\gamma = 1.4$, a Ma= 3 shock is originated ($c_\mathrm{s} = (\gamma p/\rho)^{1/2} = 1$ cm s^{-1}; $v_\mathrm{wind} = 3$ cm s^{-1}). We set the boundary conditions to outflow at the right-hand and reflect both at the top and bottom. Furthermore, we impose a reflecting condition in the region in front of the step, so that the wind will hit the step and be reflected.

From the very beginning the wind hits the step border and a shock wave is formed — see the lower panel of Fig. B.17. Also at this corner (the singular point), a rarefaction wave is born. The corner will introduce numerical errors that will be present all along the evolution of the simulation. From this point, small numerical fluctuations are born and spread over the horizontal step surface, causing the formation of a subtle structure or layer. Just right after the simulation starts, at $t = 0.1$ s, the shock formed in front of the step will start moving upwards as it curves — see the lower panel of Fig. B.17. At $t = 0.5$ s — upper panel of Fig. B.18 — the shock has already expanded, and at $t = 0.7$ s, this structure reaches the upper boundary and is reflected — see the bottom panel of Fig. B.18. As it continues moving downstream, the reflected wave merges with the incident shock. The first reflected shock will experience two more reflections: the first, on the step surface at $t = 1.2$ s — the upper panel of Fig. B.19 — and, the second, at the top of the domain again at $t = 3.3$ s — see Fig. B.20, upper panel. After the first reflection the formation of a Mach stem at $t = 1.8$ s — lower panel of Fig. B.19 — can be clearly seen. From $t = 2$ s on, the development of Kelvin-Helmholtz instabilities at the first Mach stem can be appreciated — see the bottom panel of Fig. B.19 and Fig. B.20. This point, the intersection of the incident and reflected shock, is responsible for the numerical instabilities that keep growing in size as time goes on. That is, these numerical errors suffer from an amplification phenomenon that does not decrease with increasing refinement. Around $t \sim 3$ s, we see the formation of a second Mach stem at the second reflection point ($x \sim 1.65$ cm), that might be induced by the numerical noise created at the corner of the step. At the edge of the surface step, small subtle structures appear, resembling Kelvin-Helmholtz instabilities — see Fig. B.20.

This problem has no analytical solution. However we can compare our results to the ones obtained by Woodward & Colella (1984). They performed this test to compare the efficiency of different codes[1] — as Emery (1968) previously did. Our

---

[1] They presented simulations performed with different schemes (such as Godunov's scheme,

results reproduce the same structures, the multiple reflections at similar times and positions and the formation of Kelvin-Helmholtz instabilitites. It is worth noting that the Kelvin-Helmholtz instabilities are better resolved and fully appreciated in our simulations because of the high resolution used. Therefore, we conclude that the *FLASH* code has the ability of handling strong shocks. It can also describe unsteady flows that suffer multiple reflections and that tend to converge to a particular flow pattern with time.

B.6 The Sedov explosion

The Sedov explosion (Sedov, 1959; Landau & Lifshitz, 1987) consists of a detonation wave created by introducing an instantaneous amount of energy in a small area of the domain. This translates into an over-pressure that drives a wave and sweeps the domain preserving its spherical symmetry. With this problem we are testing the ability of the code to handle strong explosions and to keep spherical geometries. The problem has an analytical solution (Sedov, 1959).

To model the Sedov explosion we assume a fluid at rest in a computational domain of 1 unit length, 1×1 cm. The density is set to 1 g cm^{-3} and the pressure to 1×10^{-5} dyn cm^{-2} everywhere. At the initial time we introduce an energy perturbation ($E = 0.85$ erg) in an area of size $r \sim 0.0136$ cm, centered in the domain ($x = y = 0.5$ cm). Since we have used 6 levels of refinement (a resolution of 0.0039 cm), we are increasing the energy in a very reduced area, and the over-pressure resembles a Dirac delta. We solve the problem adopting an ideal gas equation of state with $\gamma = 1.4$. The initial pressure will be $p_0 \sim (\gamma - 1)E/r^2$. This over-pressure generates a detonation that spreads over the domain, preserving the spherical geometry, as can be seen in Fig. B.21.

The immediate postshock velocity, density and pressure are given, respectively, by:

$$v \simeq \frac{2u}{(\gamma+1)} \tag{B.2}$$

$$\rho \simeq \frac{(\gamma+1)\rho_0}{(\gamma-1)} \tag{B.3}$$

$$p \simeq \frac{2\rho_0 u^2}{(\gamma+1)} \tag{B.4}$$

where u is the speed of the shock, that depends on its geometry and parameters such as the time, E and ρ_0. We have stopped the simulation at $t = 0.27$ s, the time at which the explosion is reaching the borders of the domain (the boundary conditions

---

MUSCL scheme or PPM) and also discussed techniques to reduce the numerical noise

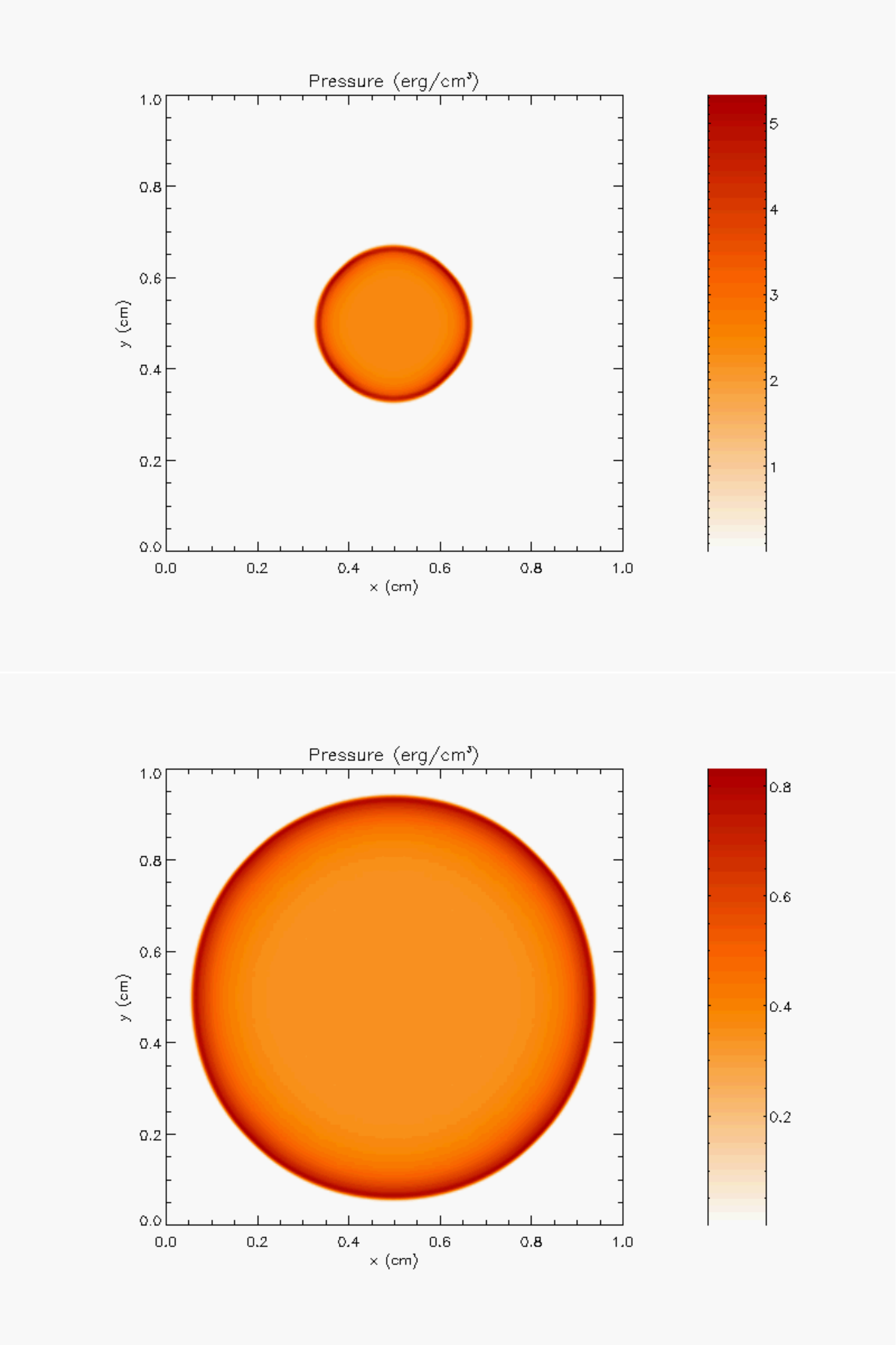

Figure B.21: Snapshots of the pressure at $t = 0.03$ s (upper panel) and $t = 0.21$ s (lower panel) for the Sedov test. As time goes on, the explosion spreads over the domain, while the pressure drops. The spherical geometry is preserved as the detonation sweeps the domain.

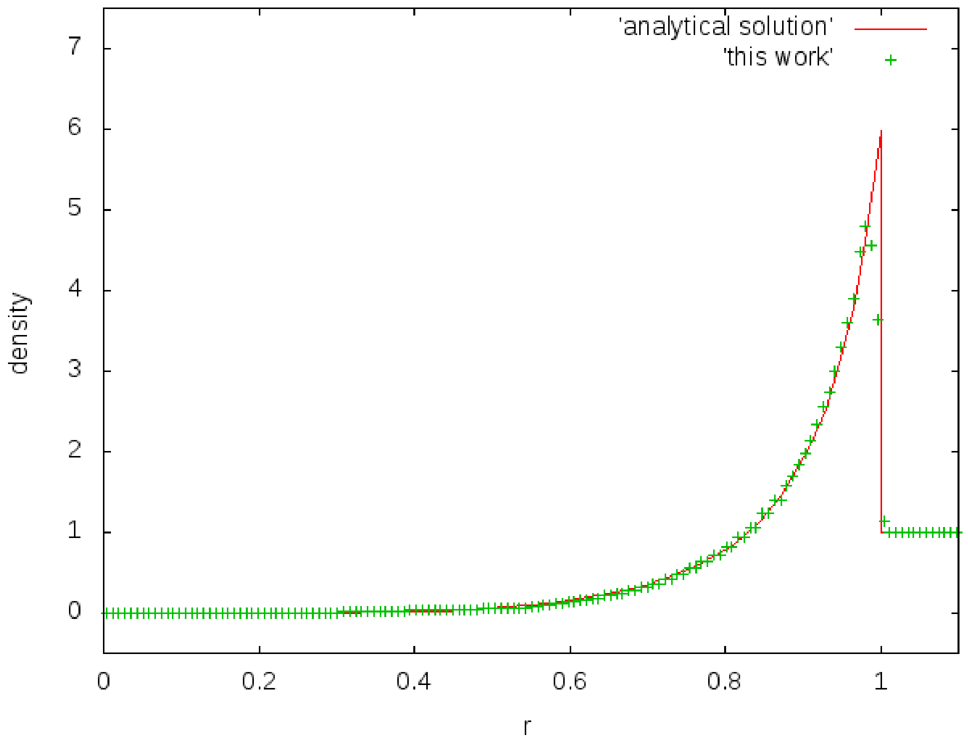

Figure B.22: Comparison of the analytical solution with the density values obtained using the *FLASH* code at $t = 0.27$ s for the Sedov test. Our results match the analytical solution behind the shock, but the code fails to capture the shock discontinuity. The height of the peak is reduced 20.2% in the numerical solution, although the shock profile is indeed captured. Using a coarse grid will result in clipping and rounding the peak profile.

are set to outflow at all the sides). We have compared our numerical results with the analytical solution in Figs. B.22, B.23, and B.24. A quick look at these figures allows to conclude that the *FLASH* code, with 6 levels of refinement, is able to reproduce the analytical results quite well. The shock structure is captured with 3 grid points as can be seen in all three figures. For the pressure and the density — Figs. B.23 and B.22, respectively — our numerical solution fits well the analytical solution behind the shock. The shock discontinuity is far from being perfectly resolved, since the code at this resolution is not able to reproduce the peak intensities for both, the density and the pressure. For the pressure, the peak is reduced $\sim 13.4\%$ and for the density the peak is $\sim 20.2\%$ lower than the analytical solution. The code, instead, performs better at describing the velocity around the shock discontinuity and the postshock behavior, since the velocity peak is just $\sim 4.2\%$ lower than the analytical solution. However, the code shows oscillations in the area near the center of the grid — see Fig. B.24. However, in general, we conclude that the code can track the

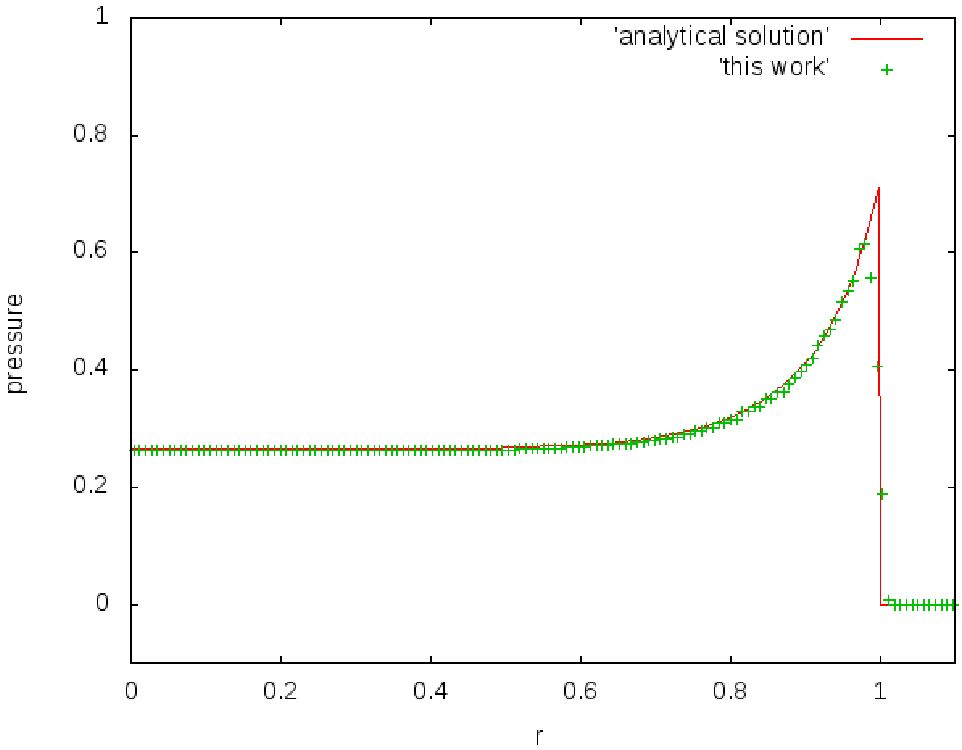

Figure B.23: Same as Fig. B.22, but for the pressure. Behind the detonation wave, our results fit the analytical solution. The code does not resolve the shock discontinuity perfectly, since the peak is now 13.4% lower than the analytical result. The discontinuity is captured with only 3 cell points (as it happens with the density and the velocity).

evolution of the explosion properly. We nevertheless note that using a good level of resolution would improve the description of the shock discontinuity and the behavior of the region behind the shock.

B.7 The homologous dust collapse problem

The dust collapse problem consists of a homogeneous sphere that collapses (Colgate & White, 1966; Monchmeyer & Muller, 1989), hence allowing to test the ability of the code to keep the spherical geometry and the density constant in the interior while the implosion takes place. This is a self-gravitating problem and the gravitational field is calculated solving the Poisson equation. We use the multipole solver included in *FLASH*, which is suitable for problems that involve spherical symmetry. Hence, we are also testing the *FLASH* code gravity module. With the approximation that the pressure is null, this problem has an analytical solution (Colgate & White, 1966),

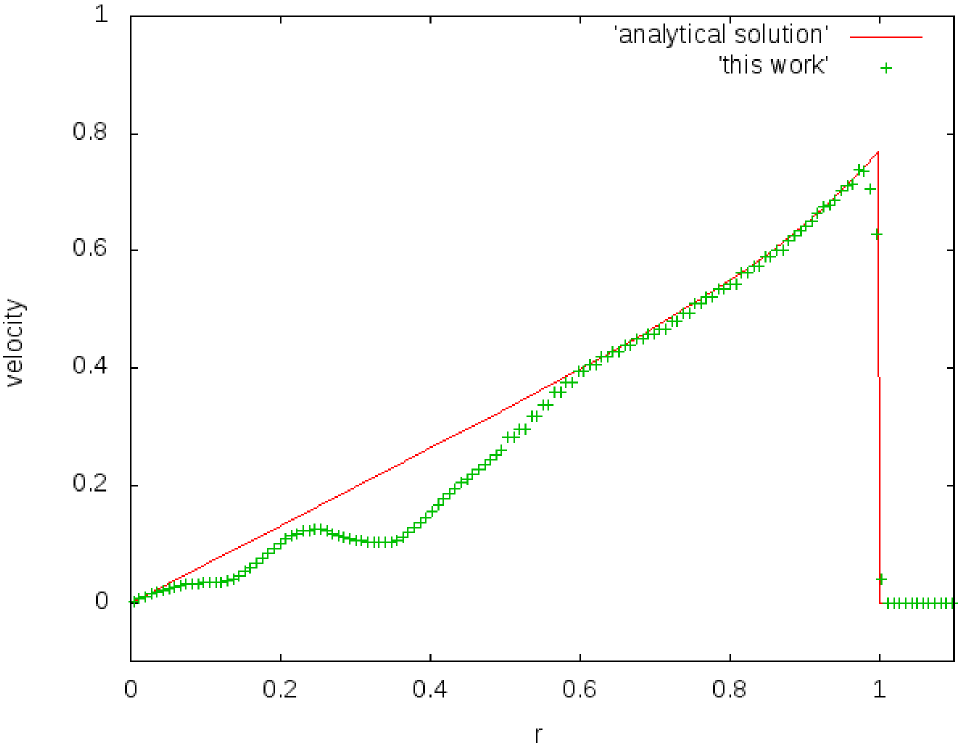

Figure B.24: Same as Fig. B.22, but for the velocity. This time, the code can resolve the shock front structure fairly well, since now the peak is reduced only by 4.2%. Although the detonation wave is better reproduced, now we find a worse fit in the region near the center of the domain.

where the radius follows the following equation:

$$\sqrt{\frac{8\pi G\rho_0}{3}}t = \sqrt{1-\frac{r(t)}{r_0}}\sqrt{\frac{r(t)}{r_0}} + \sin^{-1}\sqrt{1-\frac{r(t)}{r_0}} \tag{B.5}$$

We construct a homogeneous sphere of r = 6.5×10^8 cm in the center of the grid (7×10^8 cm, 7×10^8 cm, 7×10^8 cm) by setting the density to 1×10^9 g cm^{-3}. The sphere is initially at rest and, since the gravitational force is the only force acting on the sphere, it will start collapsing immediately. We have performed the simulation in three dimensions and used cartesian coordinates. The domain is a three-dimensional cube of 1.4×10^9 cm and the boundary conditions are set to outflow at all sides. We used an ideal gas with $\gamma = 1.67$. The calculation has administered 4 blocks per axis and 4 levels of refinement that translates into a resolution of 5.5×10^6 cm.

Our numerical results show that the code is able to mantain correctly the spherical symmetry when collapsing — see Figs. B.25 and B.26, for the evolution of the

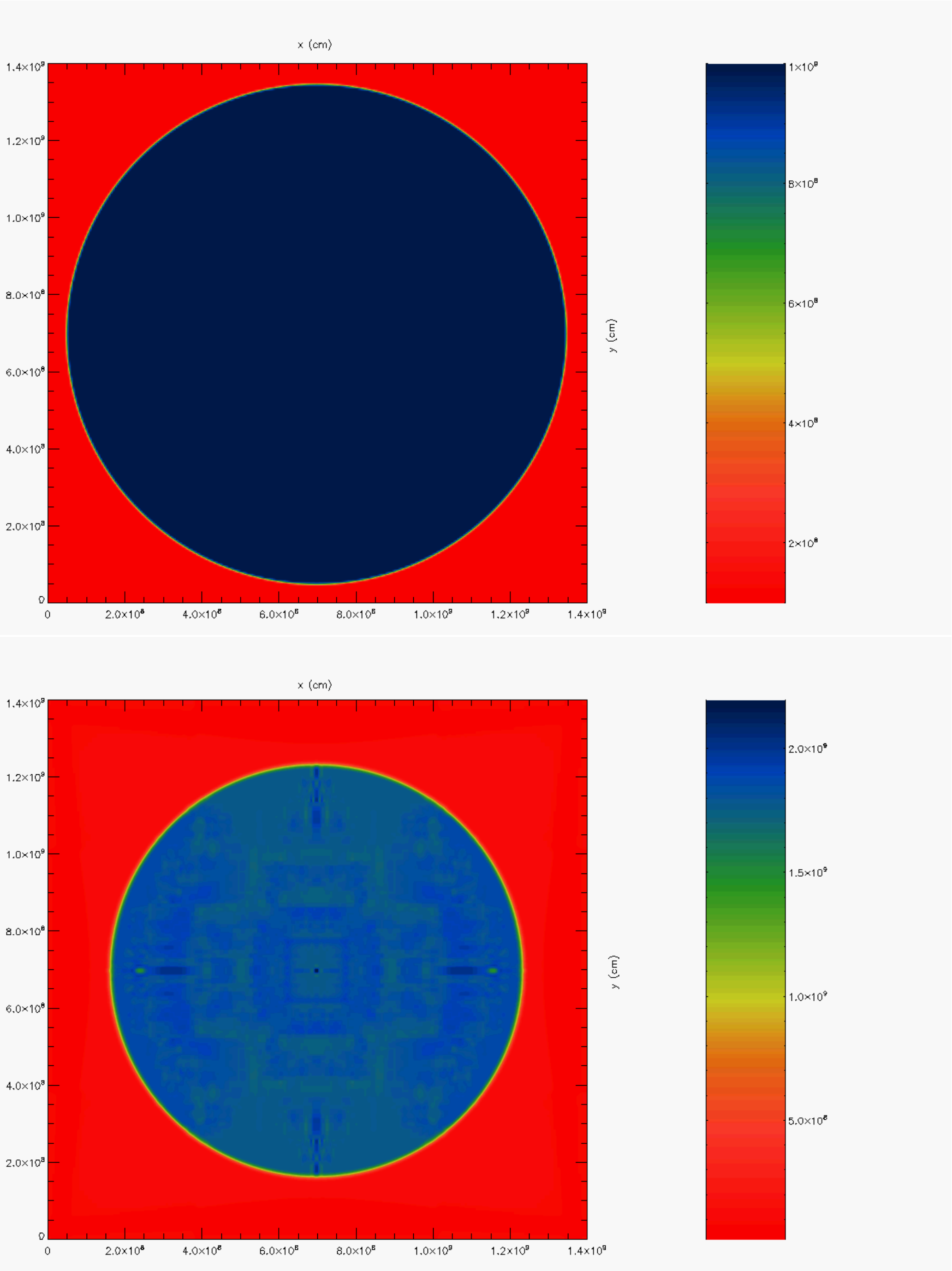

Figure B.25: The density field is plotted at $t = 0$ s (upper panel) and $t = 0.034$ s (lower panel) for the homologous dust sphere problem. The boundaries of the sphere are quite sharp.

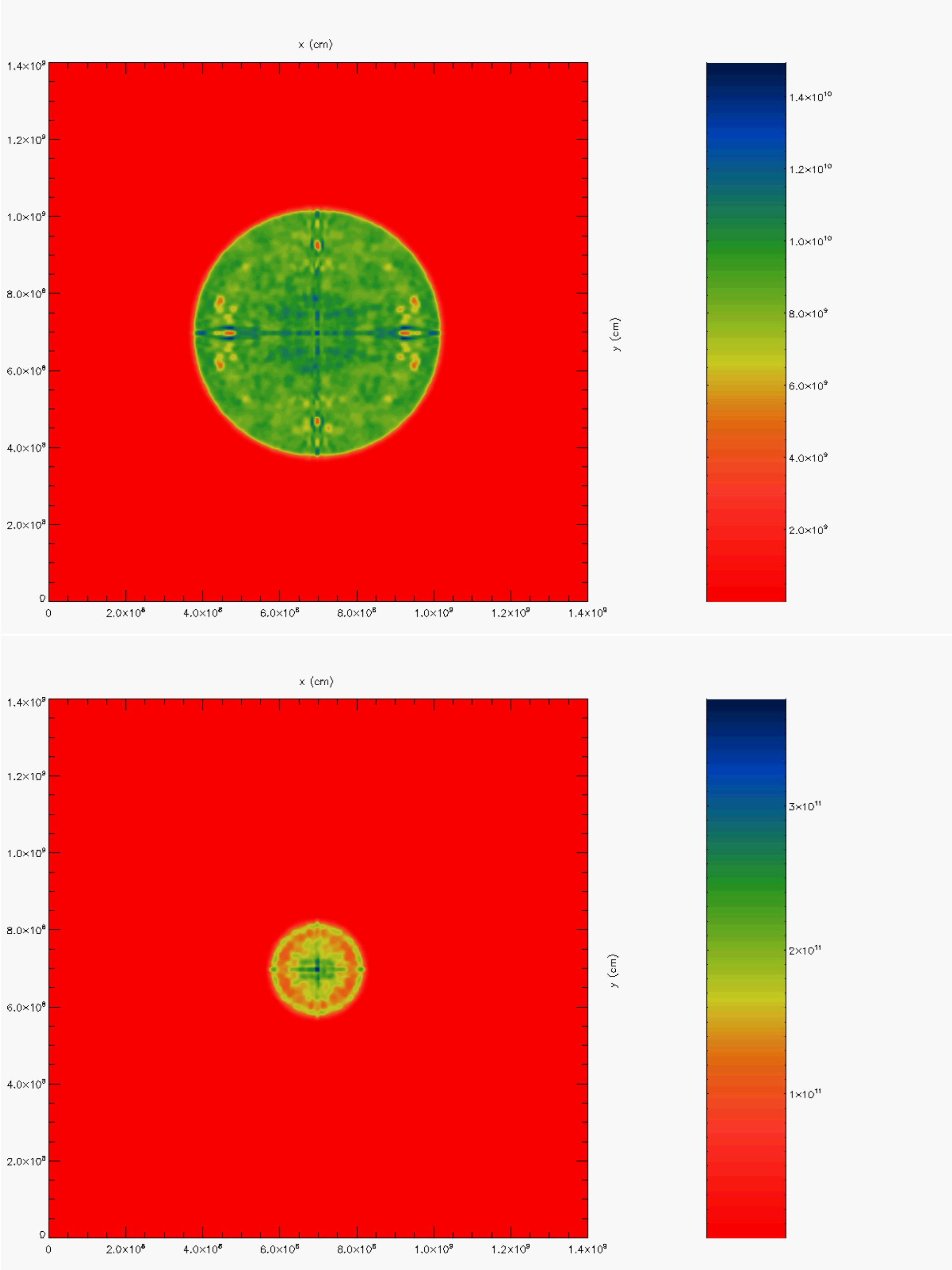

Figure B.26: Same as Fig. B.25, but for $t = 0.054$ s (upper panel) and at $t = 0.064$ s (lower panel).

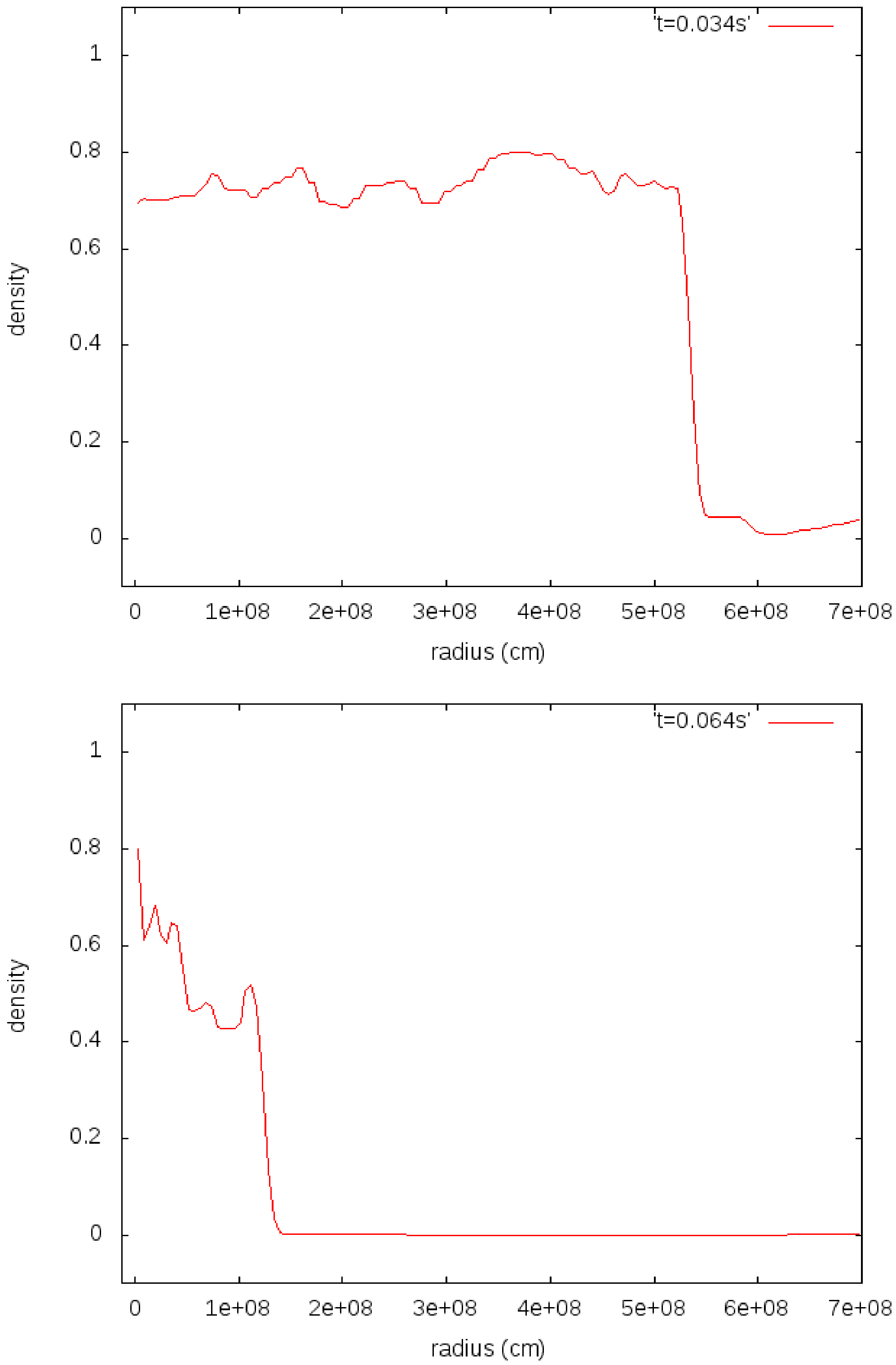

Figure B.27: Density profiles at $t = 0.034$ s (upper panel) and $t = 0.064$ s (lower panel) for the three-dimensional homologous dust sphere problem. Fluctuations appear and isotropy breaks at late times, specially at the center of the computational domain.

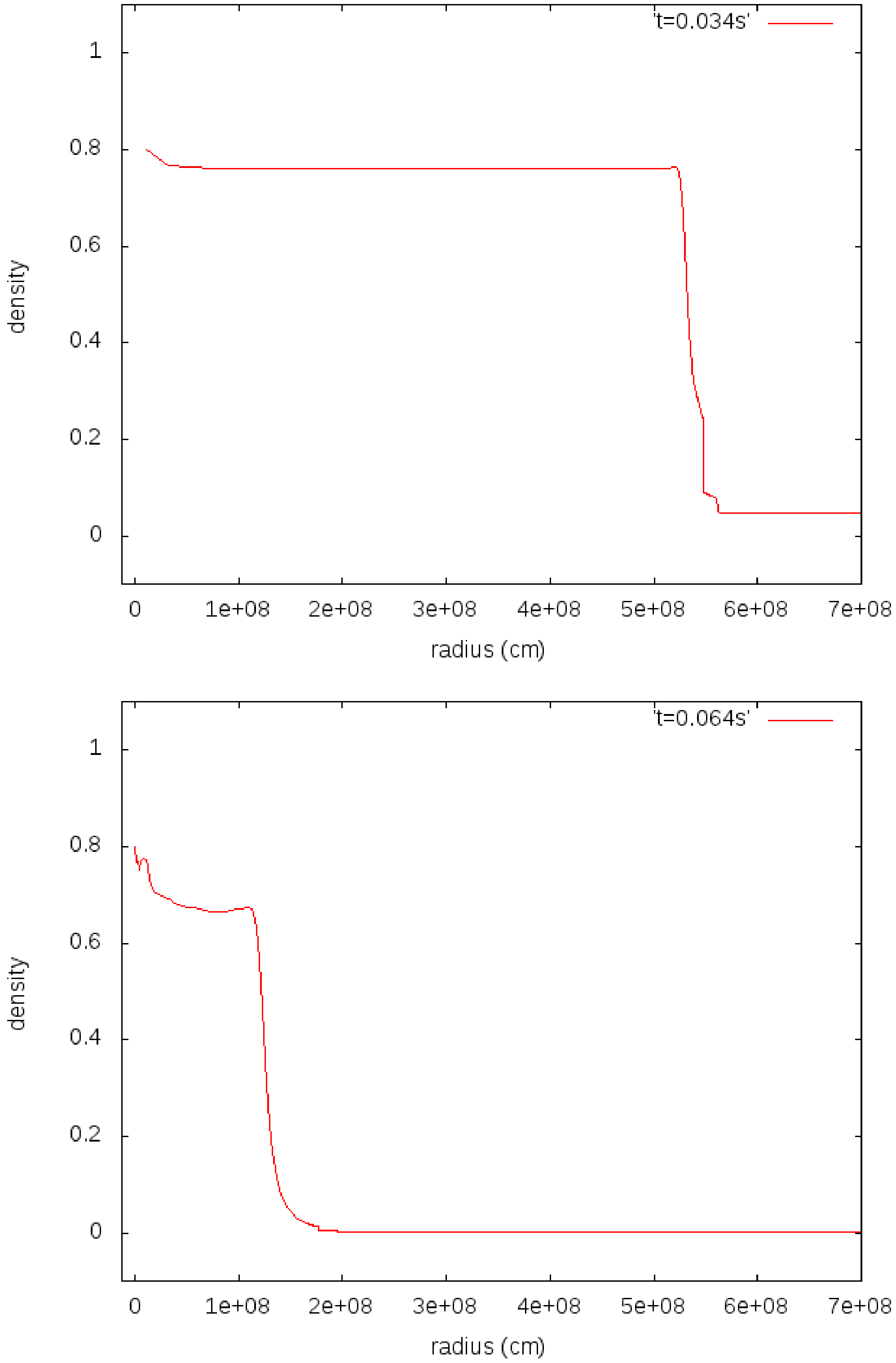

Figure B.28: Same as Fig. B.27, but for the one-dimensional simulation. The density remains constant, except for small numerical oscillations at $r = 0$ cm at the end of the simulation.

collapsing sphere projected onto the xy plane. In Fig. B.27 we show the density profiles to see how well this simulation reproduces the expected results. To analyze the results the density has been scaled by 2.53×10^{9} g cm^{-3} when $t = 0.034$ s and by 3.22×10^{11} g cm^{-3} when $t = 0.064$ s. As can be seen the numerical solution departs from the analytical one, and this is even more apparent at late times. At $t = 0.034$ s, the density remains almost constant in the interior of the sphere, although there are oscillations about 8.7% at most. At $t = 0.064$ s, the density does not remain constant in the entire interior and strong oscillations appear. We conclude that at this level of refinement, the code does not describe the interior density profile correctly. Nevertheless, it is worth noting that the radius of the collapsing sphere, $r(t)$, at both times ($t = 0.034$ s and $t = 0.064$ s, respectively), satisfies Eq. (B.5). Therefore, the code is able to predict the right collapse time evolution.

Performing three-dimensional simulations requires large amounts of computational resources, specially when high level of refinements are used. We have performed the same simulation in one dimension, this time using 8 levels of refinement, to prove that the code can improve the results when the refinement is increased. The results are shown in Fig. B.28. The density profile has been scaled by 2.32×10^{9} g cm^{-3} for $t = 0.034$ s (upper panel) and by 1.83×10^{11} g cm^{-3} for $t = 0.064$ s (lower panel). This time, the code is able to reproduce correctly the constant density profile at short times (upper panel) and also at late stages (lower panel), although numerical errors appear at the origin in the latter case. The analytical solution of the dust sphere collapse predicts that the density should remain constant during the implosion. Our results show that when a high level of refinement is used, the density profile remains isotropic in the interior of the sphere, although fluctuations appear at the center of the grid. The isotropy seems to break at $r = 0$ — the density grows abruptly near the origin, see the lower panel of Fig. B.28 — especially at late times. This effect results from the difficulty of maintaining the spherical symmetry with a cartesian grid. This problem can be solved using a refinement marking routine that comes within the *FLASH* package, which refines specific small regions of the domain (such as the center of the sphere) and, hence, improves the results at the center of the grid. It is worth noting that oscillations also appear in the border of the collapsing sphere, specially at initial times — see the upper panels of both Figs. B.27 and B.28. Nevertheless, the code is able to keep sharp boundaries and spherical symmetry during most of the time (see Figs. B.25 and B.26). Our results are very similar to those obtained by Monchmeyer & Muller (1989).

B.8 The cellular problem

The cellular problem reproduces a two-dimensional carbon detonation, and hence it is a good test for the *FLASH* burn unit. Detonation problems rely on Chapman-Jouguet and Zeldovich-Neumann-Doring detonation theories (William, 1985). However, multi-dimensional detonation simulations help showing the complex time-dependent detonation structure that appears behind the shock wave which the theory does not predict. The thin shock wave, that leaves the ashes behind, in fact comes with subtle physics hidden within the multi-dimensionality. Historically, this test has also been performed in order to explore the detonation regime in degenerate matter, such as in type Ia supernovae (Gamezo et al., 1999; Boisseau et al., 1996).

The problem consists of a gas, whose composition is pure ^{12}C. The fluid is initially at rest and the density is 1×10^7 g cm^{-3}, while the temperature is 2×10^8 K. We set reflect boundary conditions at both sides and periodic boundary conditions at the top and bottom of the domain. The size of the two-dimensional computational domain is 256×25.6 cm. The area within the domain ($0 < x < 25.6$ cm) is perturbed by setting the density to 4.236×10^7 g cm^{-3}, the temperature to 4.423×10^9 K and the post-shock material velocity to 2.877×10^8 cm s^{-1}. These values will cause an over-driven detonation that propagates to the right. As the shock front reaches supersonic velocities, it compresses the material and burns the ^{12}C fuel along the x-axis (see Fig. B.29). We use an equation of state suitable for degenerate matter (Timmes & Swesty, 2000) and a nuclear network which consists of an α chain of 13 isotopes connected via (α, γ) and (γ, α) reactions (^{4}He, ^{12}C, ^{16}O, ^{20}Ne, ^{24}Mg, ^{28}Si, ^{32}S, ^{36}Ar, ^{40}Ca, ^{44}Ti, ^{48}Cr, ^{52}Fe and ^{56}Ni) plus 8 isotopes (^{27}Al, ^{31}P, ^{35}Cl, ^{39}K, ^{43}Sc, ^{47}V, ^{51}Mn and ^{55}Co) for $(\alpha, p)(p, \gamma)$ and $(\gamma, p)(p, \alpha)$ links, to mimic correctly the energy when the temperature is above 2.5×10^9 K. We use 8 levels of refinement that translates into a resolution of 0.025 cm.

The initial detonation is damped to a relaxed state. When $t = 45$ ns, the detonation becomes unstable since density perturbations show up, in such a way that the initial planar detonation wave is substituted by a complex cell structure which will continue driving the detonation — see Fig. B.30. These cell structures consist of:

- Incident shocks that move forward.
- Triple points, corresponding to small hot spots that act as small detonations and where transverse waves are born.
- Transverse waves, corresponding to new shock waves that move backwards, which continue alive by colliding against another waves and creating new triple points.

As a result, the detonation will step forward moving backwards and colliding with other transverse waves. As the detonation wave advances, it burns material.

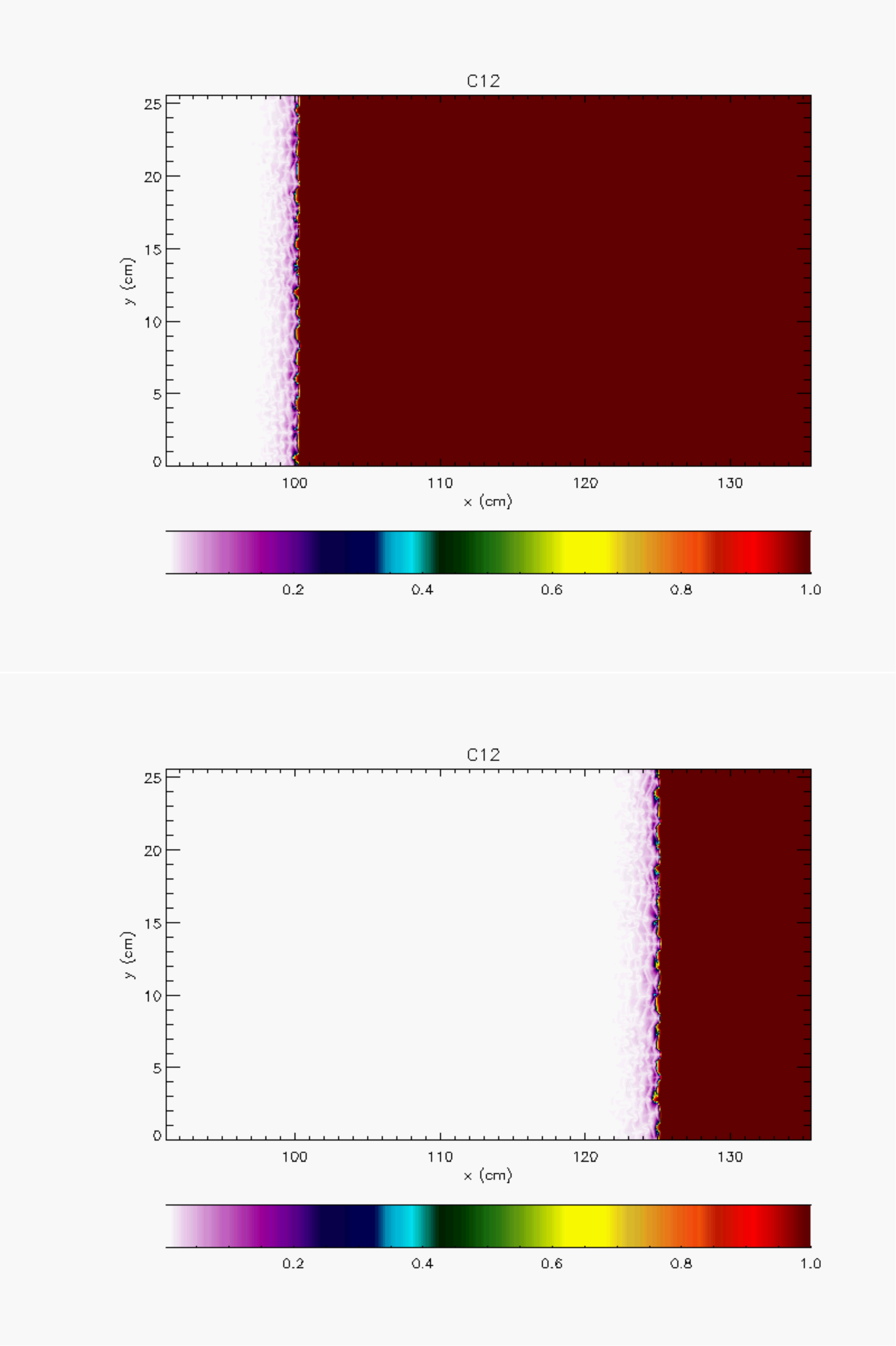

Figure B.29: Snapshots of the ^{12}C distribution at $t = 62.510$ ns (upper panel) and $t = 82.503$ ns (lower panel) for the cellular problem.

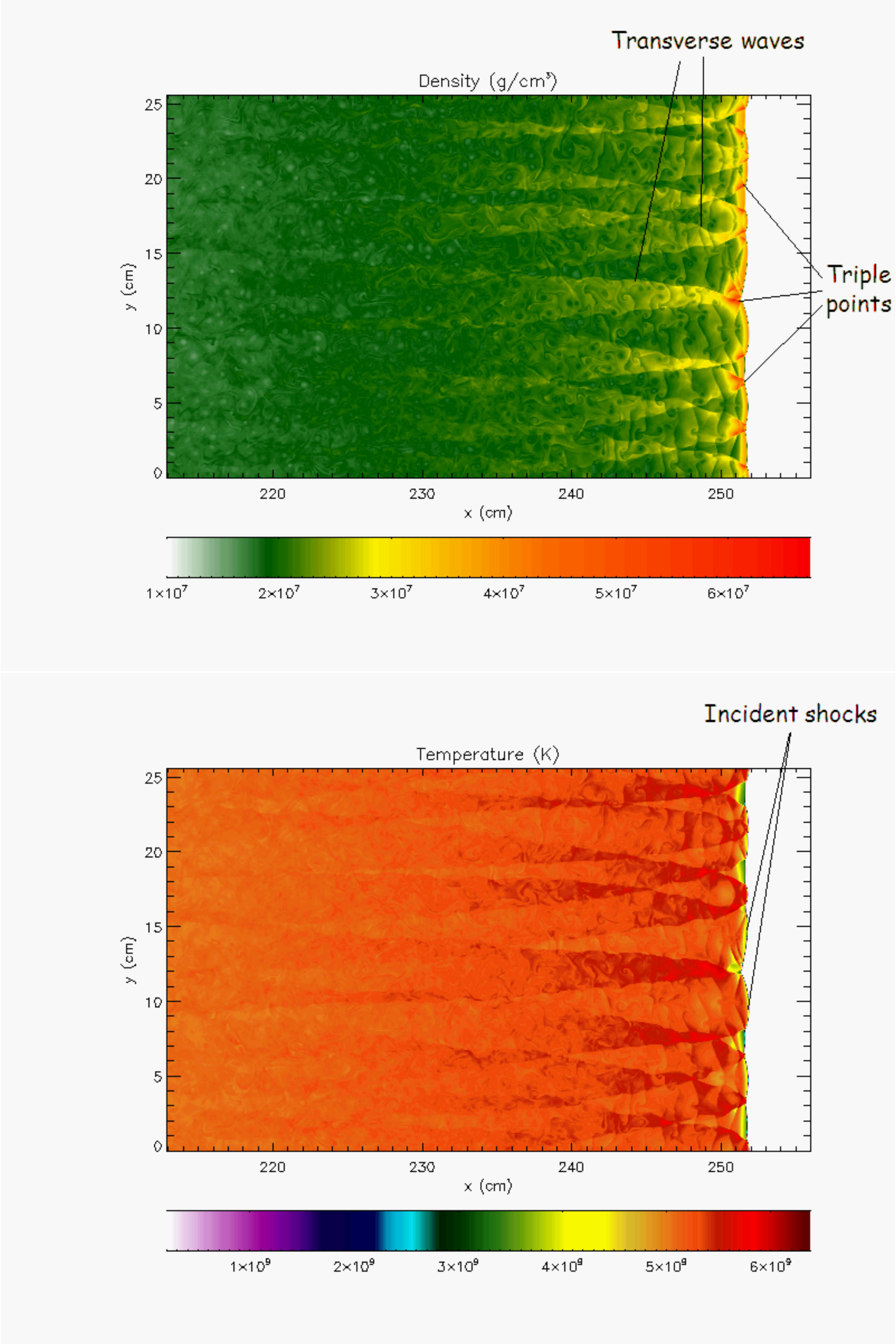

Figure B.30: Snapshots of the detonation front moving to the right at supersonic velocities. The density (upper panel) and temperature (lower panel) are shown for $t = 185.016$ ns, showing the complex multi-dimensional cell structure: incident wave, triple points and transverse waves. Notice that the post-shock structure extends about 20 cm behind the front.

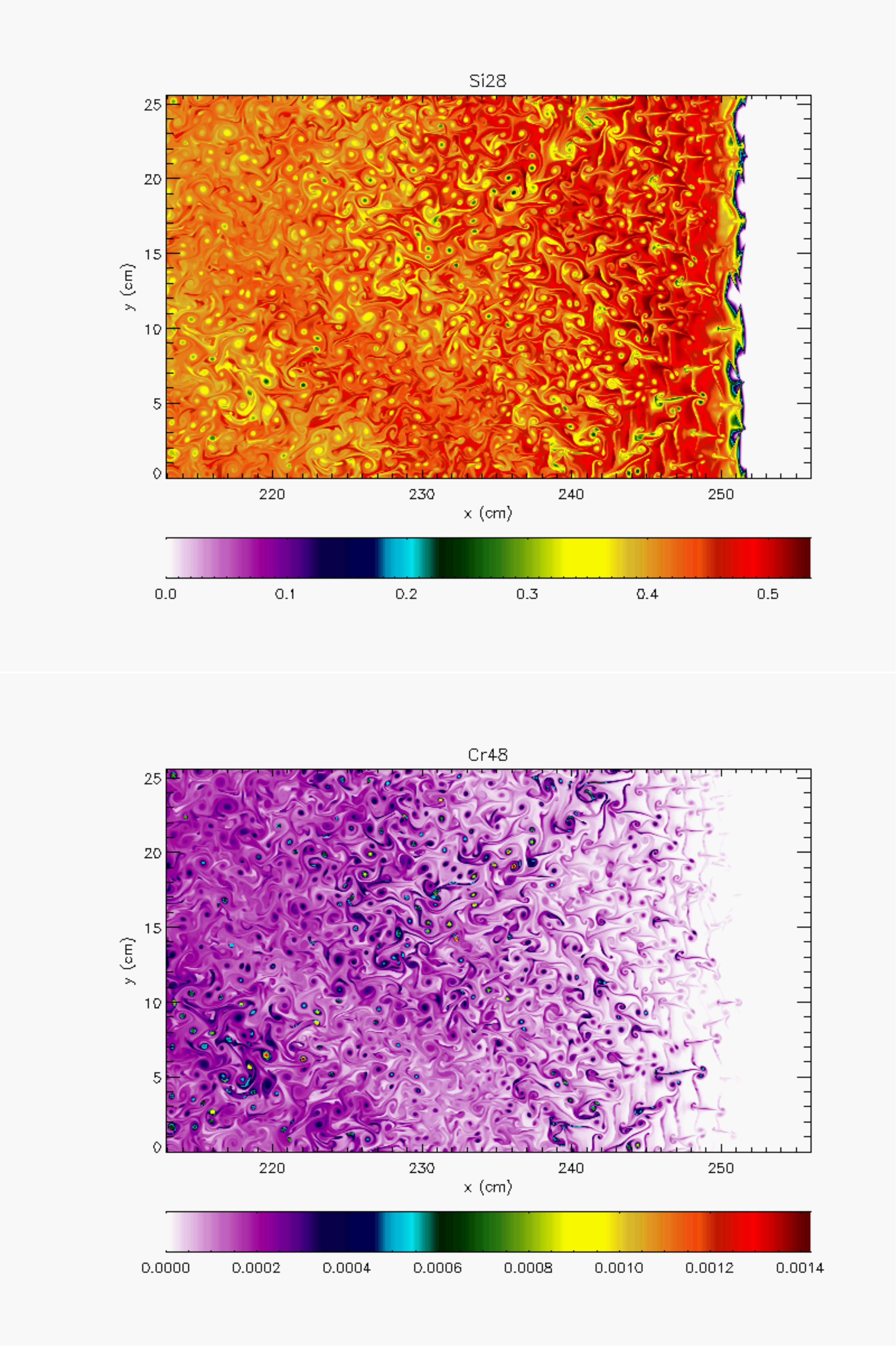

Figure B.31: Snapshots of the distribution of ^{28}Si (upper panel) and ^{48}Cr (lower panel) at t = 185.015 ns, for the cellular problem, showing the formation of Kelvin-Helmholtz instabilities.

As a result, ^{12}C is exhausted and behind the wave the ashes of combustion remain. In figure B.31, the distributions of the ashes left behind by the detonation, such as ^{28}Si and ^{48}Cr, are depicted. In these panels Kelvin-Helmholtz instabilities can be better appreciated, although these instabilities can also be seen in the distribution of densities — see Fig. B.30, upper panel. Obviously, the better the resolution, the more detailed the structures are.

The simulations presented here match the results obtained by Timmes et al. (2000), since we get the same multi-dimensional detonation structure (triple points, transverse waves...). The results also agree with the results of Gamezo et al. (1999) and Boisseau et al. (1996), although these studies were performed with carbon-oxygen degenerate matter. Therefore, we conclude that the *FLASH* code is able to handle problems in very extreme conditions such as detonations in degenerate matter and solve scenarios where combustion should be coupled to hydrodynamics. For instance, the cellular problem reproduces correctly the evolution of a detonation in a very short time (the duration of the simulation is 186 ns), using very small timesteps ($\delta t = 9 \times 10^{-12}$ s). Furthermore, the code is able to resolve the subtle structures involved such as Kelvin-Helmholtz instabilities, when the resolution is high enough.

Appendix C

Mapping a one-dimensional model onto a PPM scheme

A classical nova event, which may last 10^5 years, is characterized by very different timescales: a long timescale regime during the accretion stage and a short timescale phase (lasting only a few minutes) during the explosive stage. Due to the stability condition that explicit codes like *FLASH* must fulfill (see appendix A), the accretion phase cannot be followed with this code. These initial stages need to be described with a completely different type of code, and preferably by implicit codes, while the short timescales faced when the thermonuclear runaway sets are better suited for explicit codes. For the calculations reported in this Thesis, we have adopted the same initial model than Glasner et al. (1997), which was computed with a one-dimensional implicit code. Therefore, the difficulty resides in mapping the original simulation onto the grid of a new code (Shankar et al., 1992; Shankar & Arnett, 1994; Glasner & Livne, 1995; Glasner et al., 1997, 2007; Kercek et al., 1998, 1999; Zingale et al., 2001).

The mapping procedure can introduce errors since we are following the evolution of the nova event with two different codes, and hence, the coupling has to be as accurate as possible. The aim of the mapping is to port a hydrostatic one-dimensional model to a multi-dimensional frame, which should remain in hydrostatic equilibrium after increasing the dimensionality. However, several aspects may amplify the errors that result from mapping the model onto a new grid and, as a result, the initial model might be pushed out of equilibrium when mapped in more than one dimension. It is worth noting that the two types of codes can use different equations of state, different hydrodynamic solvers and different boundary conditions (Zingale et al., 2002). Moreover, one-dimensional codes usually rely on Mixing Length Theory to describe convection. Since we do not have any guess on how to represent this one-dimensional fluid motion profile in the new multi-dimensional grid, velocities are set to zero after the mapping.

FLASH uses the mapping procedure described in Zingale et al. (2002), where mapping of an initial hydrostatic model onto an explicit, Godunov scheme (actually, a PPM scheme) is detailed. The idea is to construct an initial setup that contains the information of the initial one-dimensional model which will remain in hydrostatic equilibrium (over several hydrodynamical timescales) until a perturbation is imposed.

C.1 The initial model

The initial model adopted by Glasner et al. (1997) assumes accretion of solar-like material ($Z = 0.02$) on top of a $1\,M_{\odot}$ white dwarf at a rate of $5 \times 10^{-9}\,M_{\odot}\ \mathrm{yr}^{-1}$ until the mass of the accreted envelope was $\sim 2 \times 10^{-5}\,M_{\odot}$. The calculation was evolved until the temperature at the bottom layers of the accreted envelope reached $\sim 10^{8}$ K, that is, just before the thermonuclear runaway ensues. This one-dimensional model contains 51 layers. Of these, 25 correspond to the accreted envelope, and the remaining 26 layers belong to the core (see Tables C.1 to C.5). For each layer, several physical quantities such as the pressure, temperature, density, velocity and composition are tabulated. *FLASH* interpolates this initial model onto a two-dimensional (three-dimensional) computational domain with a spacing given by the finest grid. Radially, the core extends between $\sim 5.46 \times 10^{8}$ cm and $\sim 5.51 \times 10^{8}$ cm. The composition of the core material only comprises ^{12}C and ^{16}O, with $X(^{12}\mathrm{C})=X(^{16}\mathrm{O})=0.5$ by mass. On top of the core, a solar-like accreted envelope is placed — see Tables C.3, C.4 and C.5. Under the assumption of plane-parallel geometry, we have constructed a computational domain that extends up to 800 km and contains all the physical information of the initial one-dimensional model.

After a proper choice of the maximum level of refinement $\mathtt{lrefine}_{\mathtt{max}}$, the number of blocks `nblocky` and the number of cells `nyb`, a uniform grid is constructed by interpolation with $\mathtt{nblocky}\times\mathtt{nyb}\times 2^{\mathtt{lrefine}_{\mathtt{max}}-1}$ points (512 grid points for a choice of 4 blocks along the radial direction, 8 cells inside each block and 5 levels of refinement). This step is necessary because the original spacing is very coarse. Density, temperature and composition are taken as input from the new interpolated points and the new quantitites are returned by calling the equation of state (see Appendix A.3). This is a crucial step to make the input quantities (evaluated with another code) consistent with the new equation of state, and hence, fully consistent with *FLASH*. Abundances will be renormalized in case they get mangled due to inaccuracies in the interpolation step. When comparing the final thermodynamic quantities with the original values, the accuracy is very high — differences less than 1% (Zingale et al., 2002) are found. Finally, velocities are reset to 0. Note that the maximum velocity found in the intial model (see Table C.1 and Table C.2) is of the order of 10^{3} cm s^{-1}, which is small compared to the velocities achieved in the runaway phase (usually $\sim 10^{7}$ cm s^{-1}).

The next step is to modify the density profile to force the model to be in hydrostatic equilibrium. A hydrostatic equilibrium stage is reached when the velocity $\mathbf{v}$ is zero and therefore, Eqs. (A.1), (A.2) and (A.3) reduce to:

$$\frac{\partial \rho}{\partial t} = 0 \tag{C.1}$$

$$\nabla P = \rho \mathbf{g} \tag{C.2}$$

$$\frac{\partial \rho E}{\partial t} = 0 \tag{C.3}$$

whilst the equation for the variation in chemical abundances is given by:

$$\frac{\partial \rho X_i}{\partial t} = 0 \tag{C.4}$$

Then, the code uses an iteration method to adjust the density and pressure, such that these equations are satisfied. Describing the density as an average between two adjacent cells, Eq. (C.2) can be expressed as:

$$\langle P \rangle_i - \langle P \rangle_{i-1} = \frac{gdx}{2}(\langle \rho \rangle_i + \langle \rho \rangle_{i-1}) \tag{C.5}$$

where g is the gravitational acceleration and dx is the size of the cell. This reconstruction represents a first-order differencing. One could use a high-order differencing but this will not translate into a relevant improvement of the results (Zingale et al., 2002).

Starting from a fixed layer i with density $\langle \rho \rangle_i$, and taking the density $\langle \rho \rangle_{i-1}$ and pressure $\langle P \rangle_{i-1}$ from the layer below, Eq. (C.5) allows to integrate outwards by adjusting the pressure and density profiles to finally meet the hydrostatic equilibrium condition. Then, we can evaluate $\langle P \rangle_i$:

$$\langle P \rangle_i = \langle P \rangle_{i-1} + \frac{gdx}{2}(\langle \rho \rangle_i + \langle \rho \rangle_{i-1}) \tag{C.6}$$

The new pressure $\langle P \rangle_i$ satisfies hydrostatic equilibrium through the two layers involved in this reconstruction. However, this pressure is not consistent with the original density of the layer. Therefore, the next step is to implement an iteration process to make density and pressure consistent in this layer:

$$\delta \rho = \frac{\langle P \rangle_i - \langle P \rangle_0}{\frac{\partial P}{\partial \rho} - \frac{1}{2} dxg} \tag{C.7}$$

$$\langle \rho \rangle_i = \langle \rho \rangle_i + \delta \rho \tag{C.8}$$

where $\delta \rho$ is the correction to the density and $\langle P \rangle_0$ is the pressure corresponding to $\langle \rho \rangle_i$, that is, the value that results after calling the equation of state with $\langle \rho \rangle_i$ as input.

This loop, from Eq. (C.6) to Eq. (C.8), is repeated until convergence is found (sixth figure in the value of the density). The density thus constructed is now taken as the final density of the layer. Calling the equation of state once more, will update the thermodynamic quantities in this layer. This iteration method results in the construction of a density profile that guarantees hydrostatic equilibrium and that is consistent with the equation of state. We can continue this first-order differencing through the layers of the model by steeping outwards and iterating as described above. At the end, all the layers will be in hydrostatic equilibrium.

C.2 Boundary Conditions

The solution to our problem is sensitive to the boundary conditions imposed at the borders of the computational domain (Glasner et al., 2005). As mentioned in Appendix A, the boundary conditions are implemented in the guard cells — ghost cells that contain the information from neighboring blocks or physical boundaries (the real borders of the computational domain). Several combinations of boundary conditions can be adopted depending on the geometry and the type of code: reflecting at the bottom (Shankar & Arnett, 1994; Glasner et al., 1997; Kercek et al., 1998), outflow at the top (Shankar et al., 1992; Shankar & Arnett, 1994; Kercek et al., 1998) and periodic (Shankar et al., 1992; Kercek et al., 1998) or reflecting (Glasner et al., 2007) at the sides. However, we need boundary conditions that are as realistic as possible and that match the physical properties of the problem.

FLASH allows to implement hydrostatic boundary conditions at the top and the bottom of the domain. This is done by using the hydrostatic equilibrium equation in the guard cells — see Eq. (C.2). The iteration method described in the previous section is used to recompute the pressure and density profiles. From the last interior row of cells we want to integrate the pressure from the innermost to the outermost guard cell to finally meet hydrostatic equilibrium. To set hydrostatic boundary conditions in the frontiers, we have used a first-order differencing scheme and a Newton-Raphson iteration method as detailed in the previous section.

The balance between the pressure gradient and the gravity source can be complemented with an additional constraint on the velocity field:

1. At the bottom, we choose a reflect condition on the velocity along the direction perpendicular to the boundary by reversing its sign. This condition will enforce the rigid boundary condition that is required to represent the white dwarf core. Therefore, the material that hits the bottom will not flow off and instead, will be reflected.

2. At the top, we choose an outflow constraint on the velocity field. The normal velocity is given a zero gradient and therefore, waves will be allowed to flow

off the domain (a situation that resembles the outflow condition during a thermonuclear runaway). In fact, this boundary condition is just a simple outflow condition, but complemented with a readjusted density and pressure profile in order to support the material against gravity (the weight of the matter above).

3. Periodic boundary conditions are imposed at the vertical sides. This constraint imposes a wrap-around condition, such that the conditions found at one side are repeated at the other side. Therefore, waves that hit one side will appear at the other side. This boundary condition might impose softer consequences than using reflect boundary conditions.

   Since we only simulate a small slice of the star, imposing periodic conditions physically means that we are taking into account the presence of material at the sides. To test this, we have performed a simulation setting outflow boundary conditions at the sides. The formation of the initial temperature fluctuations is also found, but as soon as ^{12}C is grabbed from the core, material flows off the grid and convection cannot set in. As a consequence, there is a front that progressively moves upwards, but advancing irregularly (see Fig. C.1).

It is worth mentioning that we have also run a set of preliminary simulations to test the stability of the initial model. We found that the model remains indeed stable over a large number of hydrodynamical timescales when we turn combustion off.

C.3 Temperature perturbation

The *FLASH* code supports several kinds of perturbations. We have adopted Gaussian (see Chapter 2) and top-hat (see Chapter 3) temperature perturbations to break the initial hydrostatic equilibrium, without changing the density. The perturbation is imposed at an arbitrary point (x_0, y_0, z_0) and is characterized by a given influence radius (R_x, R_y, R_z). Adopting this notation, for a top-hat perturbation we have:

$$T = T_\mathrm{P} \quad \text{if} \quad \left(\frac{x-x_0}{R_x}\right)^2 + \left(\frac{y-y_0}{R_y}\right)^2 + \left(\frac{z-z_0}{R_z}\right)^2 \leq 1 \tag{C.9}$$

$$T = T_0 \quad \text{if} \quad \left(\frac{x-x_0}{R_x}\right)^2 + \left(\frac{y-y_0}{R_y}\right)^2 + \left(\frac{z-z_0}{R_z}\right)^2 > 1 \tag{C.10}$$

where T_P is the value of the perturbation and T_0 is the unperturbed value of the temperature. For the Gaussian perturbation we use:

$$T = T_\mathrm{P}\ \mathrm{e}^{-\left[\left(\frac{x-x_0}{R_x}\right)^2+\left(\frac{y-y_0}{R_y}\right)^2+\left(\frac{z-z_0}{R_z}\right)^2\right]} \tag{C.11}$$

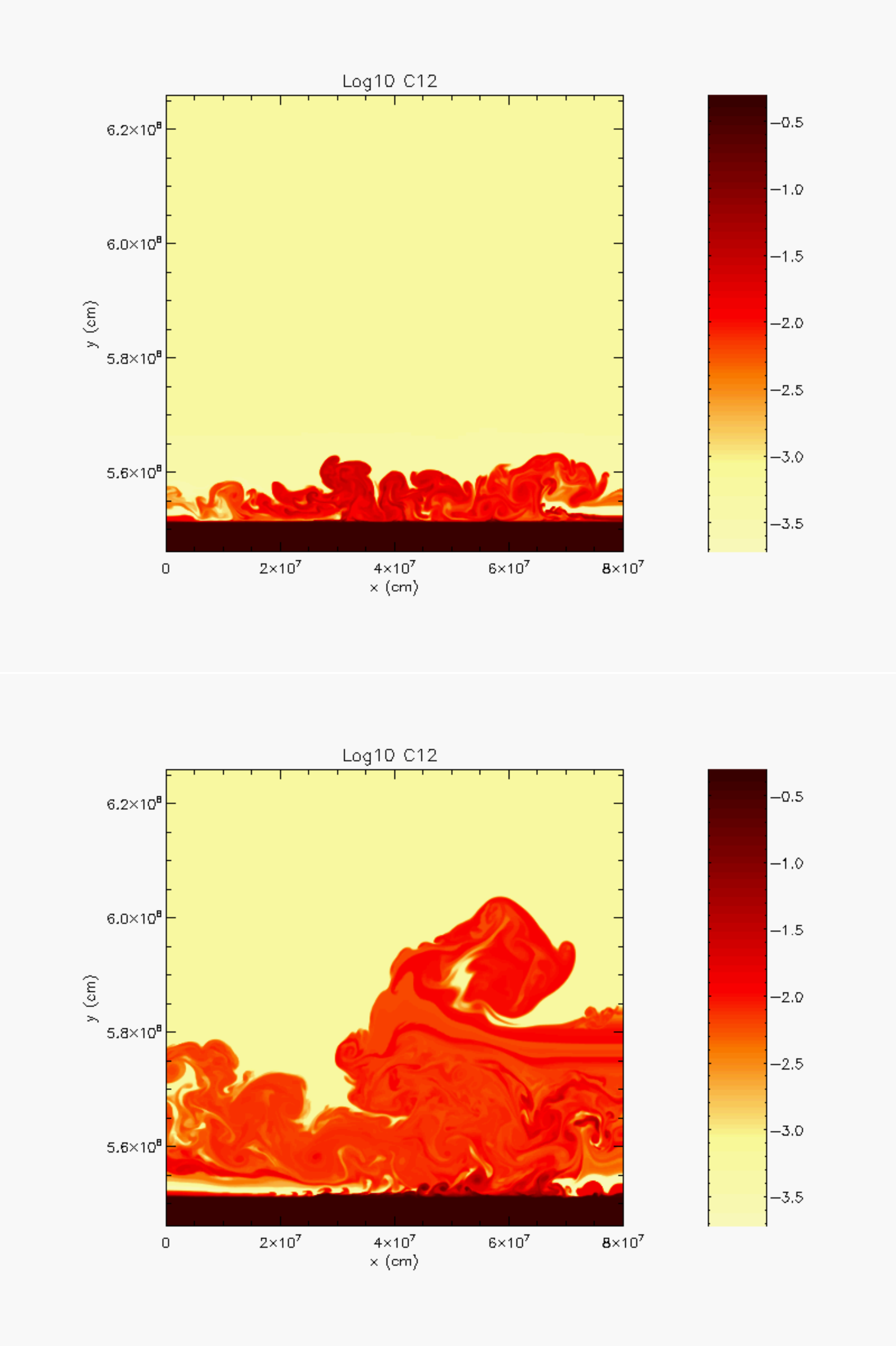

Figure C.1: Snapshots of the ^{12}C abundance in logarithmic scale at $t = 249$ s (upper panel) and $t = 261$ s (lower panel), showing how the front advances asymmetrically and disperses because of the choice of outflow boundary conditions at both sides.

where $T_{\rm P}$ is again the value of the perturbation.

We find that both types of perturbation give similar results (Casanova et al., 2010, 2011; Zingale et al., 2001). Usually we adopt a very small perturbation in size to affect the initial model as less as possible, but to guarantee that it is properly set in at least one cell of the domain (specially for the Gaussian perturbation), the current cell is split in arbitrary sub-cells. Specifically, in our simulations we have split each cell in 4 sub-cells along each direction. Then, the new temperature is computed in each sub-cell using the expressions given above for the perturbation. We evaluate the average temperature over all the sub-cells within the cell and, finally, this ultimate value is imposed as the final temperature in the zone. The accuracy of this procedure increases with the number of sub-cells.

The initial temperature perturbation breaks the hydrostatic equilibrium of the model, paving the road to the onset of convection (Shankar & Arnett, 1994; Kercek et al., 1998, 1999; Zingale et al., 2001). Other authors (Shankar et al., 1992), prefer instead to introduce a different perturbation, such as an initial energy deposition. It is worth noting that Glasner & Livne (1995) and Glasner et al. (1997) do not adopt any initial perturbation, but they find large temperature variations of about $\sim 20\%$ at the initial time, which we judge to be excessive.

Table C.1: Input model — white dwarf core properties.

R (cm)	v_y (cm s^{-1})	ρ (g cm^{-3})	T (K)	P (dyn cm^{-2})
5.4596653e+08	1.2954253e+01	5.6001159e+03	2.0837071e+07	8.4678059e+18
5.4601547e+08	1.3096678e+01	5.5274926e+03	2.0952766e+07	8.3467338e+18
5.4606462e+08	1.3241740e+01	5.4537303e+03	2.1085702e+07	8.2273348e+18
5.4611421e+08	1.3390246e+01	5.3782769e+03	2.1237583e+07	8.1087932e+18
5.4616441e+08	1.3542740e+01	5.3007883e+03	2.1410106e+07	7.9907018e+18
5.4621530e+08	1.3699638e+01	5.2210241e+03	2.1605020e+07	7.8728573e+18
5.4626697e+08	1.3861309e+01	5.1387932e+03	2.1824186e+07	7.7551583e+18
5.4631948e+08	1.4028112e+01	5.0539245e+03	2.2069639e+07	7.6375546e+18
5.4637290e+08	1.4200419e+01	4.9662499e+03	2.2343661e+07	7.5200215e+18
5.4642730e+08	1.4378632e+01	4.8755856e+03	2.2648880e+07	7.4025470e+18
5.4648276e+08	1.4563191e+01	4.7817246e+03	2.2988470e+07	7.2851256e+18
5.4653935e+08	1.4754587e+01	4.6844385e+03	2.3366070e+07	7.1677550e+18
5.4659718e+08	1.4953373e+01	4.5834544e+03	2.3785919e+07	7.0504345e+18
5.4665635e+08	1.5160177e+01	4.4784642e+03	2.4253369e+07	6.9331643e+18
5.4671699e+08	1.5375719e+01	4.3691142e+03	2.4774962e+07	6.8159453e+18
5.4677924e+08	1.5600830e+01	4.2550031e+03	2.5358664e+07	6.6987785e+18
5.4684327e+08	1.5836475e+01	4.1356882e+03	2.6013882e+07	6.5816650e+18
5.4690928e+08	1.6083792e+01	4.0106925e+03	2.6751961e+07	6.4646064e+18
5.4697751e+08	1.6344130e+01	3.8794292e+03	2.7587999e+07	6.3476043e+18
5.4704824e+08	1.6619113e+01	3.7412217e+03	2.8540436e+07	6.2306606e+18
5.4712181e+08	1.6910713e+01	3.5955721e+03	2.9627854e+07	6.1137773e+18
5.4719865e+08	1.7221372e+01	3.4419682e+03	3.0875504e+07	5.9969569e+18
5.4762375e+08	1.8991583e+01	1.2591026e+03	3.2224920e+07	5.8204086e+18
5.4810413e+08	2.1145657e+01	1.1005466e+03	3.5944085e+07	5.5859004e+18
5.4876971e+08	2.7131800e+01	7.9110415e+02	4.9098624e+07	5.3537182e+18
5.5029385e+08	9.2492143e+01	3.6058309e+02	4.9850255e+07	5.1175079e+18

Table C.2: Same as Table C.1, but for the accreted envelope.

R (cm)	v_y (cm s^{-1})	ρ (g cm^{-3})	T (K)	P (dyn cm^{-2})
5.5181629e+08	1.5792098e+02	3.5005197e+02	9.8353022e+07	4.8812107e+18
5.5335559e+08	2.2421693e+02	3.3966409e+02	9.6698941e+07	4.6520193e+18
5.5492367e+08	2.9189803e+02	3.2931773e+02	9.5024024e+07	4.4276705e+18
5.5660978e+08	3.6483591e+02	3.1869730e+02	9.3274010e+07	4.2014719e+18
5.5830189e+08	4.3820197e+02	3.0788340e+02	9.1462209e+07	3.9756651e+18
5.6002188e+08	5.1295092e+02	2.9718832e+02	8.9636924e+07	3.7567811e+18
5.6178401e+08	5.8971275e+02	2.8650463e+02	8.7779036e+07	3.5426350e+18
5.6359812e+08	6.6892914e+02	2.7577080e+02	8.5876042e+07	3.3321093e+18
5.6556751e+08	7.5514605e+02	2.6468257e+02	8.3868178e+07	3.1195230e+18
5.6756280e+08	8.4273557e+02	2.5333129e+02	8.1770769e+07	2.9073418e+18
5.6961104e+08	9.3289907e+02	2.4204860e+02	7.9637948e+07	2.7018802e+18
5.7173178e+08	1.0265189e+03	2.3072097e+02	7.7445596e+07	2.5011874e+18
5.7394024e+08	1.1242949e+03	2.1927985e+02	7.5176102e+07	2.3043069e+18
5.7625041e+08	1.2268861e+03	2.0768148e+02	7.2814964e+07	2.1108485e+18
5.7867527e+08	1.3349108e+03	1.9589725e+02	7.0349100e+07	1.9207790e+18
5.8135748e+08	1.4548114e+03	1.8361881e+02	6.7698746e+07	1.7297872e+18
5.8414267e+08	1.5797756e+03	1.7092139e+02	6.4873229e+07	1.5403528e+18
5.8707289e+08	1.7117443e+03	1.5816270e+02	6.1931486e+07	1.3583486e+18
5.9026427e+08	1.8560488e+03	1.4507751e+02	5.8794340e+07	1.1806595e+18
5.9381493e+08	2.0173091e+03	1.3133965e+02	5.5356739e+07	1.0043381e+18
5.9774291e+08	2.1965699e+03	1.1689219e+02	5.1566809e+07	8.3084024e+17
6.0214250e+08	2.3984307e+03	1.0177603e+02	4.7377287e+07	6.6305037e+17
6.0735065e+08	2.6388351e+03	8.5620457e+01	4.2590492e+07	5.0011462e+17
6.1381026e+08	2.9391655e+03	6.7785696e+01	3.6871714e+07	3.4173582e+17
6.3445218e+08	3.8981114e+03	3.7782369e+01	2.4943216e+07	1.2807606e+17

Table C.3: Initial composition of the accreted envelope (I).

R (cm)	^{1}H	^{3}He	^{4}He	^{7}Be	^{8}B
5.5181629e+08	6.9821346e-01	3.1913088e-07	2.8089900e-01	3.8033206e-09	4.1284952e-10
5.5335559e+08	6.9821372e-01	3.1921928e-07	2.8089896e-01	3.7806006e-09	3.8741702e-10
5.5492367e+08	6.9821407e-01	3.1933377e-07	2.8089889e-01	3.7535315e-09	3.5751951e-10
5.5660978e+08	6.9821448e-01	3.1947415e-07	2.8089881e-01	3.7230857e-09	3.2439190e-10
5.5830189e+08	6.9821497e-01	3.1963822e-07	2.8089870e-01	3.6907281e-09	2.8977981e-10
5.6002188e+08	6.9821551e-01	3.1981865e-07	2.8089857e-01	3.6584860e-09	2.5588666e-10
5.6178401e+08	6.9821609e-01	3.2001497e-07	2.8089841e-01	3.6268917e-09	2.2324324e-10
5.6359812e+08	6.9821672e-01	3.2022675e-07	2.8089821e-01	3.5964407e-09	1.9229653e-10
5.6556751e+08	6.9821741e-01	3.2045940e-07	2.8089797e-01	3.5668524e-09	1.6267515e-10
5.6756280e+08	6.9821817e-01	3.2071071e-07	2.8089767e-01	3.5391168e-09	1.3526988e-10
5.6961104e+08	6.9821897e-01	3.2097252e-07	2.8089731e-01	3.5143416e-09	1.1101319e-10
5.7173178e+08	6.9821981e-01	3.2124646e-07	2.8089687e-01	3.4924651e-09	8.9685090e-11
5.7394024e+08	6.9822071e-01	3.2153364e-07	2.8089633e-01	3.4734902e-09	7.1146658e-11
5.7625041e+08	6.9822168e-01	3.2183497e-07	2.8089569e-01	3.4574148e-09	5.5276343e-11
5.7867527e+08	6.9822271e-01	3.2215143e-07	2.8089491e-01	3.4441883e-09	4.1934979e-11
5.8135748e+08	6.9822385e-01	3.2249298e-07	2.8089397e-01	3.4334211e-09	3.0668243e-11
5.8414267e+08	6.9822510e-01	3.2285878e-07	2.8089286e-01	3.4252874e-09	2.1598180e-11
5.8707289e+08	6.9822642e-01	3.2324134e-07	2.8089161e-01	3.4196799e-09	1.4674064e-11
5.9026427e+08	6.9822785e-01	3.2365184e-07	2.8089020e-01	3.4161295e-09	9.4555633e-12
5.9381493e+08	6.9822945e-01	3.2410578e-07	2.8088858e-01	3.4143209e-09	5.6357169e-12
5.9774291e+08	6.9823123e-01	3.2461239e-07	2.8088674e-01	3.4140321e-09	3.0381549e-12
6.0214250e+08	6.9823324e-01	3.2518094e-07	2.8088466e-01	3.4149794e-09	1.4360086e-12
6.0735065e+08	6.9823559e-01	3.2584358e-07	2.8088222e-01	3.4169362e-09	5.4833224e-13
6.1381026e+08	6.9823847e-01	3.2665811e-07	2.8087923e-01	3.4198516e-09	1.3953296e-13
6.3445218e+08	6.9824128e-01	3.2745368e-07	2.8087631e-01	3.4228716e-09	1.0739722e-14

Table C.4: Initial composition of the accreted envelope (II).

R (cm)	^{12}C	^{13}C	^{13}N	^{14}N	^{15}N
5.5181629e+08	5.6169357e-04	1.3836168e-04	2.4713791e-04	1.3840691e-02	1.6012972e-07
5.5335559e+08	5.6257139e-04	1.3917889e-04	2.4613225e-04	1.3841121e-02	1.8500367e-07
5.5492367e+08	5.6368648e-04	1.4023131e-04	2.4483946e-04	1.3841658e-02	2.2194649e-07
5.5660978e+08	5.6502454e-04	1.4151439e-04	2.4326637e-04	1.3842295e-02	2.7529843e-07
5.5830189e+08	5.6654898e-04	1.4300514e-04	2.4144234e-04	1.3843012e-02	3.5134191e-07
5.6002188e+08	5.6817781e-04	1.4463514e-04	2.3945181e-04	1.3843773e-02	4.5543446e-07
5.6178401e+08	5.6989091e-04	1.4639838e-04	2.3730258e-04	1.3844573e-02	5.9940519e-07
5.6359812e+08	5.7166442e-04	1.4828937e-04	2.3500165e-04	1.3845408e-02	8.0032448e-07
5.6556751e+08	5.7351563e-04	1.5035404e-04	2.3249335e-04	1.3846296e-02	1.0885761e-06
5.6756280e+08	5.7538184e-04	1.5256961e-04	2.2980562e-04	1.3847225e-02	1.5040740e-06
5.6961104e+08	5.7716462e-04	1.5486237e-04	2.2702756e-04	1.3848164e-02	2.0730027e-06
5.7173178e+08	5.7883112e-04	1.5724466e-04	2.2414371e-04	1.3849121e-02	2.8466269e-06
5.7394024e+08	5.8034971e-04	1.5972418e-04	2.2114417e-04	1.3850100e-02	3.8679701e-06
5.7625041e+08	5.8167740e-04	1.6230632e-04	2.1802174e-04	1.3851103e-02	5.1904776e-06
5.7867527e+08	5.8277651e-04	1.6499686e-04	2.1476865e-04	1.3852137e-02	6.8603934e-06
5.8135748e+08	5.8364769e-04	1.6787668e-04	2.1128619e-04	1.3853233e-02	8.9581907e-06
5.8414267e+08	5.8425822e-04	1.7093299e-04	2.0758865e-04	1.3854388e-02	1.1493925e-05
5.8707289e+08	5.8462191e-04	1.7409919e-04	2.0375539e-04	1.3855579e-02	1.4368037e-05
5.9026427e+08	5.8479155e-04	1.7746342e-04	1.9967843e-04	1.3856843e-02	1.7594715e-05
5.9381493e+08	5.8481047e-04	1.8114446e-04	1.9521204e-04	1.3858225e-02	2.1218524e-05
5.9774291e+08	5.8471646e-04	1.8520555e-04	1.9027711e-04	1.3859753e-02	2.5222320e-05
6.0214250e+08	5.8454539e-04	1.8970716e-04	1.8479740e-04	1.3861453e-02	2.9581716e-05
6.0735065e+08	5.8431503e-04	1.9488586e-04	1.7848147e-04	1.3863416e-02	3.4443295e-05
6.1381026e+08	5.8402087e-04	2.0116574e-04	1.7080684e-04	1.3865810e-02	4.0112370e-05
6.3445218e+08	5.8373225e-04	2.0722989e-04	1.6338290e-04	1.3868132e-02	4.5396230e-05

Table C.5: Initial composition of the accreted envelope (III).

R (cm)	^{14}O	^{15}O	^{16}O	^{17}O	^{17}F
5.5181629e+08	3.1245880e-06	1.1318170e-04	5.8843582e-03	9.4994767e-05	3.5111963e-06
5.5335559e+08	3.0729606e-06	1.1185491e-04	5.8844239e-03	9.5004831e-05	3.4505888e-06
5.5492367e+08	3.0081522e-06	1.1017351e-04	5.8845074e-03	9.5016391e-05	3.3747346e-06
5.5660978e+08	2.9312072e-06	1.0815712e-04	5.8846077e-03	9.5028813e-05	3.2849198e-06
5.5830189e+08	2.8443375e-06	1.0585546e-04	5.8847227e-03	9.5041219e-05	3.1837978e-06
5.6002188e+08	2.7520579e-06	1.0338283e-04	5.8848468e-03	9.5052624e-05	3.0766510e-06
5.6178401e+08	2.6551209e-06	1.0075524e-04	5.8849796e-03	9.5062638e-05	2.9643664e-06
5.6359812e+08	2.5542249e-06	9.7987588e-05	5.8851206e-03	9.5070861e-05	2.8477668e-06
5.6556751e+08	2.4473775e-06	9.5020453e-05	5.8852732e-03	9.5077030e-05	2.7245696e-06
5.6756280e+08	2.3364266e-06	9.1897956e-05	5.8854356e-03	9.5080384e-05	2.5969403e-06
5.6961104e+08	2.2253243e-06	8.8728723e-05	5.8856025e-03	9.5080420e-05	2.4694254e-06
5.7173178e+08	2.1136691e-06	8.5499380e-05	5.8857752e-03	9.5076769e-05	2.3415599e-06
5.7394024e+08	2.0013415e-06	8.2204050e-05	5.8859542e-03	9.5068970e-05	2.2132044e-06
5.7625041e+08	1.8883855e-06	7.8840913e-05	5.8861403e-03	9.5056467e-05	2.0844115e-06
5.7867527e+08	1.7748753e-06	7.5408525e-05	5.8863341e-03	9.5038610e-05	1.9552708e-06
5.8135748e+08	1.6578798e-06	7.1812536e-05	5.8865418e-03	9.5014017e-05	1.8224611e-06
5.8414267e+08	1.5387663e-06	6.8084308e-05	5.8867628e-03	9.4981444e-05	1.6875710e-06
5.8707289e+08	1.4205698e-06	6.4313574e-05	5.8869928e-03	9.4940727e-05	1.5540449e-06
5.9026427e+08	1.3005467e-06	6.0405986e-05	5.8872386e-03	9.4889712e-05	1.4187976e-06
5.9381493e+08	1.1755608e-06	5.6244453e-05	5.8875096e-03	9.4824781e-05	1.2783433e-06
5.9774291e+08	1.0450626e-06	5.1787962e-05	5.8878113e-03	9.4742255e-05	1.1321417e-06
6.0214250e+08	9.0891296e-07	4.7005304e-05	5.8881492e-03	9.4637998e-05	9.8012548e-07
6.0735065e+08	7.6230590e-07	4.1691585e-05	5.8885424e-03	9.4502778e-05	8.1705097e-07
6.1381026e+08	5.9681943e-07	3.5482989e-05	5.8890250e-03	9.4319830e-05	6.3375180e-07
6.3445218e+08	4.4667970e-07	2.9675644e-05	5.8894958e-03	9.4128106e-05	4.6807991e-07

Appendix D

Supplementary movies

Three supplementary movies have been included in the attached CD-ROM. The first one, 2D_C12.wmv, describes the evolution of the ^{12}C abundance in the 2-D model A (see chapter 3), showing the development of the first instabilities, and the way convection sets in and spreads over the envelope. Around $t \sim 150$ s, a set of hydrodynamic instabilities are clearly seen at the core-envelope interface. These fluctuations begin to dredge-up material from the core and pave the road for the development of convection. Convective transport appears initially in the form of small convective cells that because of conservation of vorticity in 2-D tend to merge into bigger cells with a size comparable to the size of the envelope. At the end of the simulation, the fluid motion becomes rather violent as the convective front progressively moves upwards. At $t \sim 496$ s, the front reaches the top of the computational domain. The mean, mass-averaged CNO abundance in the envelope reaches ~ 0.22, by mass, in agreement with the values inferred from the ejecta of CO novae.

Two-dimensional slices of a 3-D model showing the evolution of the ^{12}C and ^{15}O abundances (3D_C12.wmv and 3D_O15.mwv), from the onset of the initial fluctuations to the time when the convective front reaches the top of the computational domain, have also been included in the attached CD-ROM. The 2-D slices have been taken along the xz plane (arbitrarily at $y = 6 \times 10^7$ cm) of the overall 3-D volume. Similar patterns to those described above for the 2-D simulations are also found. A major exception is the way in which convection develops: in contrast to the 2-D case (Casanova et al., 2010, 2011), the convective eddies do not recombine. They tend to dissipate by breaking into smaller convective cells, transferring their energy to progressively smaller scales. These structures, vortices and filaments, undergo a similar fate down to approximately the Kolmogorov scale. This last stage is, however, intermittent and our 3D simulations appear to resolve at least the upper dissipation range. Thus the Kolmogorov scale provides an estimate of the size of the smallest eddies present in the flow. The intermittent and filamentary behavior, characteristic of these late stages, translates into contrast structures that arise as inhomogeneous abundance distributions, a well-known feature observed in the ejecta from novae. The mean, mass-averaged CNO abundance in the envelope at the end of this simulation, ~ 0.20, is very similar to the value reported above for the 2-D simulations.

Appendix E

Computational resources

The 2-D and 3-D simulations reported in this thesis, have been performed on the MareNostrum Supercomputer, which is located at the Barcelona Supercomputing Center. The MareNostrum Supercomputer has 10,240 processors and is ranked in the 118th position according to the Top500 list (as 2011), which ranks the largest supercomputers in the world. We have been granted a total amount of 1,067 kh through the following projects:

- Multi-dimensional simulation of nova outbursts: searching the source of metallicity enhancement at the core-envelope interface, 158 kh, *AECT-2010-1-0014.*
- Multi-dimensional simulation of stellar explosions: classical and primordial novae, and type I X-ray bursts, 323 kh, *AECT-2010-2-0002.*
- Multi-dimensional simulation of stellar explosions: neon-rich and primordial novae, and type I X-ray bursts, 281 kh, *AECT-2010-3-0013.*
- Mixing in classical novae and type I X-Ray bursts: a multi-dimensional approach, 305 Kh, *AECT-2011-1-0006.*

In Table E.1, we show the number of nodes and the time required in all the simulations reported in this thesis.

Table E.1: Computational details.

Model	Resolution (km)	Computational Domain (km)	Nodes	Time (kh)
A	1.56 × 1.56	800 × 800	256	3
B	1.56 × 1.56	800 × 800	256	2.3
C	1.56 × 1.56	800 × 800	256	2.9
D	1.56 × 1.56	800 × 800	256	3
E	1.56 × 1.56	800 × 800	256	2.9
F	1.56 × 1.56	1600 × 800	256	4.9
G	1.56 × 1.56	800 × 1000	256	3.6
H	1 × 1	800 × 800	256	32
I	0.39 × 0.39	800 × 800	256	110
3-D	3.25 × 3.25	800 × 800 × 800	256–512	150

Bibliography

Alexakis, A., Calder, A. C., Dursi, L. J., Rosner, R., Truran, J. W., Fryxell, B., Zingale, M., Timmes, F. X., Olson, K. & Ricker, P., 2004a. On the nonlinear evolution of wind-driven gravity waves. *Physics of Fluids*, **16**, 3256–3268.

Alexakis, A., Calder, A. C., Heger, A., Brown, E. F., Dursi, L. J., Truran, J. W., Rosner, R., Lamb, D. Q., Timmes, F. X., Fryxell, B., Zingale, M., Ricker, P. M. & Olson, K., 2004b. On Heavy Element Enrichment in Classical Novae. *ApJ*, **602**, 931–937.

Alexakis, A., Young, Y. & Rosner, R., 2002. Shear instability of fluid interfaces: Stability analysis. *Phys. Rev. E*, **65**(2), 026313–+.

Amari, S., 2002. Presolar grains from novae: their isotopic ratios and radioactivities. *New A Rev.*, **46**, 519–524.

Amari, S., Gao, X., Nittler, L. R., Zinner, E., José, J., Hernanz, M. & Lewis, R. S., 2001. Presolar Grains from Novae. *ApJ*, **551**, 1065–1072.

Angulo, C., Arnould, M., Rayet, M., Descouvemont, P., Baye, D. et al., 1999. A compilation of charged-particle induced thermonuclear reaction rates. *Nuclear Physics A*, **656**, 3–183.

Arnett, D., Meakin, C. & Young, P. A., 2009. Turbulent Convection in Stellar Interiors. II. The Velocity Field. *ApJ*, **690**, 1715–1729.

Arnett, W. D. & Meakin, C., 2010. Turbulent Cells in Stars: I. Fluctuations in Kinetic Energy. *ArXiv e-prints*.

Bader, G. & Deuflhard, P., 1983. A Semi-Implicit Mid-Point Rule for Stiff Systems of Ordinary Differential Equations. *Numerische Mathematic*, **41**, 373–398.

Bode, M. F. & Evans, A., 2008. *Classical Novae*. Cambrige: Cambridge University Press.

Böhm-Vitense, E., 1958. Über die Wasserstoffkonvektionszone in Sternen verschiedener Effektivtemperaturen und Leuchtkräfte. Mit 5 Textabbildungen. *ZAp*, **46**, 108–+.

Boisseau, J. R., Wheeler, J. C., Oran, E. S. & Khokhlov, A. M., 1996. The Multidimensional Structure of Detonations in Type IA Supernovae. *ApJ*, **471**, L99+.

Boris, J. & Book, D. L., 1997. Flux-Corrected Transport. *Journal of Computational Physics*, **135**, 172–186.

Busso, M., Wasserburg, G. J., Nollett, K. M. & Calandra, A., 2007. Can Extra Mixing in RGB and AGB Stars Be Attributed to Magnetic Mechanisms? *ApJ*, **671**, 802–810.

Calder, A. C., Alexakis, A., Dursi, L. J., Rosner, R., Truran, J. W., Fryxell, B., Ricker, P., Zingale, M., Olson, K., Timmes, F. X. & MacNeice, P., 2002a. Mixing by Non-linear Gravity Wave Breaking on a White Dwarf Surface. In M. Hernanz & J. José, ed., *Classical Nova Explosions*, vol. 637 of *American Institute of Physics Conference Series*, 134–138.

Calder, A. C., Fryxell, B., Plewa, T., Rosner, R., Dursi, L. J. et al., 2002b. On Validating an Astrophysical Simulation Code. *ApJS*, **143**, 201–229.

Cameron, A. G. W., 1959. Pycnonuclear Reations and Nova Explosions. *ApJ*, **130**, 916–+.

Casanova, J., José, J., García-Berro, E., Calder, A. & Shore, S. N., 2010. On mixing at the core-envelope interface during classical nova outbursts. *A&A*, **513**, L5+.

Casanova, J., José, J., García-Berro, E., Calder, A. & Shore, S. N., 2011. Mixing in classical novae: a 2-D sensitivity study. *A&A*, **527**, A5+.

Christy, R. F., 1966. A Study of Pulsation in RR Lyrae Models. *ApJ*, **144**, 108–+.

Clayton, D. D., 1981. Li-7 gamma-ray lines from novae. *ApJ*, **244**, L97+.

Clayton, D. D. & Hoyle, F., 1974. Gamma-Ray Lines from Novae. *ApJ*, **187**, L101+.

Clayton, D. D. & Hoyle, F., 1976. Grains of Anomalous Isotopic Composition from Novae. *ApJ*, **203**, 490–496.

Colella, P. & Glaz, H. M., 1985. Efficient solution algorithms for the Riemann problem for real gases. *Journal of Computational Physics*, **59**, 264–289.

COLELLA, P. & WOODWARD, P. R., 1984. The Piecewise Parabolic Method (PPM) for Gas-Dynamical Simulations. *Journal of Computational Physics*, **54**, 174–201.

COLGATE, S. A. & WHITE, R. H., 1966. The Hydrodynamic Behavior of Supernovae Explosions. *ApJ*, **143**, 626.

DUERBECK, H. W., 2008. Novae:an historical perspective. In M. F. Bode & A. Evans, ed., *Classical Nova Explosions*, vol. 43 of *Cambridge Astrophysics*, 1–15. Cambridge: Cambridge University Press.

DURISEN, R. H., 1977. Accretion of rotating fluids by barytropes - Numerical results for white-dwarf models. *ApJ*, **213**, 145–156.

EMERY, A. F., 1968. An Evaluation of Several Differencing Methods for Inviscid Fluid Flow Problems. *Journal of Computational Physics*, **2**, 306.

EVANS, A., 1990. Formation and Evolution of Dust in Novae. In A. Cassatella & R. Viotti, ed., *IAU Colloq. 122: Physics of Classical Novae*, vol. 369 of *Lecture Notes in Physics, Berlin Springer Verlag*, 253–+.

FORESTER, C. K., 1977. Higher order monotonic convective difference schemes. *Journal of Computational Physics*, **23**, 1–22.

FRYXELL, B., MÜLLER, E. & ARNETT, D., 1989. Computation of multidimensional flows with non-uniform composition. In W. Hillebrandt & E. Müller, ed., *Nuclear Astrophysics*, 100–102.

FRYXELL, B., OLSON, K., RICKER, P., TIMMES, F. X., ZINGALE, M., LAMB, D. Q., MACNEICE, P., ROSNER, R., TRURAN, J. W. & TUFO, H., 2000. FLASH: An Adaptive Mesh Hydrodynamics Code for Modeling Astrophysical Thermonuclear Flashes. *ApJS*, **131**, 273–334.

FRYXELL, B. A. & WOOSLEY, S. E., 1982. Finite propagation time in multidimensional thermonuclear runaways. *ApJ*, **261**, 332–336.

FUJIMOTO, M. & IBEN, JR., I., 1992. Constraints on element mixing in classical novae. *ApJ*, **399**, 646–655.

FUJIMOTO, M. Y., 1988. Differential rotation and elemental mixing in accreting stars. *A&A*, **198**, 163–172.

GAMEZO, V. N., WHEELER, J. C., KHOKHLOV, A. M. & ORAN, E. S., 1999. Multilevel Structure of Cellular Detonations in Type IA Supernovae. *ApJ*, **512**, 827–842.

GEHRZ, R. D., 1999. Infrared studies of classical novae and their contributions to the ISM. *Phys. Rep.*, **311**, 405–418.

GEHRZ, R. D., 2008. Infrared studies of classical novae. In M. F. Bode & A. Evans, ed., *Classical Nova Explosions*, vol. 43 of *Cambridge Astrophysics*, 167–193. Cambridge: Cambridge University Press.

GEHRZ, R. D., TRURAN, J. W., WILLIAMS, R. E. & STARRFIELD, S., 1998. Nucleosynthesis in Classical Novae and Its Contribution to the Interstellar Medium. *PASP*, **110**, 3–26.

GLASNER, A. & LIVNE, E., 2002. Multidimensional Nova Simulations. In M. Hernanz & J. José, ed., *Classical Nova Explosions*, vol. 637 of *American Institute of Physics Conference Series*, 124–133.

GLASNER, S. A. & LIVNE, E., 1995. Convective hydrogen burning down a nova outburst. *ApJ*, **445**, L149–L151.

GLASNER, S. A., LIVNE, E. & TRURAN, J. W., 1997. Reactive Flow in Nova Outbursts. *ApJ*, **475**, 754–+.

GLASNER, S. A., LIVNE, E. & TRURAN, J. W., 2005. The Sensitivity of Multidimensional Nova Calculations to the Outer Boundary Condition. *ApJ*, **625**, 347–350.

GLASNER, S. A., LIVNE, E. & TRURAN, J. W., 2007. Novae: The Evolution from Onset of Convection to the Runaway. *ApJ*, **665**, 1321–1333.

GLASNER, S. A. & TRURAN, J. W., 2009. Carbon-Nitrogen-Oxygen "Breakout" and Nucleosynthesis in Classical Novae. *ApJ*, **692**, L58–L61.

GODUNOV, S. K., 1959. A Difference Scheme for Numerical Solution of Discontinuous Solution of Hydrodynamic Equations. *Math. Sbornik*, **47**, 271–306.

GODUNOV, S. K., ZABRODIN, G. P. & PROKOPOV, G. P., 1961. A computational scheme for two-dimensional nonstationary problems of gas dynamics and calculation of the flow from a shock wave approaching a stationary state. *U.S.S.R. Comput. Math. Math. Phys.*, **1**, 1187–1219.

GOMEZ-GOMAR, J., HERNANZ, M., JOSE, J. & ISERN, J., 1998. Gamma-ray emission from individual classical novae. *MNRAS*, **296**, 913–920.

GUREVITCH, L. E. & LEBEDINSKY, A. I., 1957. On the causes of stellar bursts. In G. H. Herbig, ed., *Non-stable stars*, vol. 3 of *IAU Symposium*, 77–+.

HENZE, M., PIETSCH, W., SALA, G., DELLA VALLE, M., HERNANZ, M., GREINER, J., BURWITZ, V., FREYBERG, M. J., HABERL, F., HARTMANN, D. H., MILNE, P. & WILLIAMS, G. G., 2009. The very short supersoft X-ray state of the classical nova M31N 2007-11a. *A&A*, **498**, L13–L16.

Hernanz, M., 2008. Gamma-rays from classical novae. In M. F. Bode & A. Evans, ed., *Classical Nova Explosions*, vol. 43 of *Cambridge Astrophysics*, 252–283. Cambridge: Cambridge University Press.

Hernanz, M. & José, J., eds., 2002. *Classical Nova Explosions*, vol. 637 of *American Institute of Physics Conference Series*.

Hernanz, M., José, J., Coc, A., Gómez-Gomar, J. & Isern, J., 1999. Gamma-Ray Emission from Novae Related to Positron Annihilation: Constraints on its Observability Posed by New Experimental Nuclear Data. *ApJ*, **526**, L97–L100.

Hernanz, M., Jose, J., Coc, A. & Isern, J., 1996. On the Synthesis of 7Li and 7Be in Novae. *ApJ*, **465**, L27+.

Iben, Jr., I., 1975. Thermal pulses; p-capture, alpha-capture, s-process nucleosynthesis; and convective mixing in a star of intermediate mass. *ApJ*, **196**, 525–547.

Iben, Jr., I. & Fujimoto, M. Y., 2008. The evolution of nova-producing binary stars. In M. F. Bode & A. Evans, ed., *Classical Nova Explosions*, vol. 43 of *Cambridge Astrophysics*, 34–76. Cambridge: Cambridge University Press.

Iben, Jr., I., Fujimoto, M. Y. & MacDonald, J., 1991. Diffusion and mixing in classical nova precursors. *ApJ*, **375**, L27–L29.

Iben, Jr., I., Fujimoto, M. Y. & MacDonald, J., 1992. Diffusion and mixing in accreting white dwarfs. *ApJ*, **388**, 521–540.

Iliadis, C., Champagne, A., José, J., Starrfield, S. & Tupper, P., 2002. The Effects of Thermonuclear Reaction-Rate Variations on Nova Nucleosynthesis: A Sensitivity Study. *ApJS*, **142**, 105–137.

José, J., 1996. *Thermonuclear burning at the edge of stellar degenerate cores*. Ph.D. thesis, Univ. Barcelona.

José, J., 2005. Prospects in Classical Nova Modeling and Nucleosynthesis. *Nuclear Physics A*, **758**, 713–720.

José, J., Coc, A. & Hernanz, M., 1999a. Nuclear Uncertainties in the NENA-MGAL Cycles and Production of ^{22}Na and ^{26}Al during Nova Outbursts. *ApJ*, **520**, 347–360.

José, J., Coc, A. & Hernanz, M., 1999b. Nuclear Uncertainties in the NENA-MGAL Cycles and Production of ˆ22NA and ˆ26AL during Nova Outbursts. *ApJ*, **520**, 347–360.

José, J., García-Berro, E., Hernanz, M. & Gil-Pons, P., 2007. The First Nova Explosions. *ApJ*, **662**, L103–L106.

José, J. & Hernanz, M., 1998. Nucleosynthesis in Classical Novae: CO versus ONe White Dwarfs. *ApJ*, **494**, 680–+.

José, J. & Hernanz, M., 2007a. The origin of presolar nova grains. *Meteoritics and Planetary Science*, **42**, 1135–1143.

José, J. & Hernanz, M., 2007b. TOPICAL REVIEW: Nucleosynthesis in classical nova explosions. *Journal of Physics G Nuclear Physics*, **34**, 431–+.

José, J. & Hernanz, M., 2008. 10 Gyr of classical nova explosions. *Journal of Physics G Nuclear Physics*, **35**(1), 014024–+.

José, J., Hernanz, M., Amari, S., Lodders, K. & Zinner, E., 2004. The Imprint of Nova Nucleosynthesis in Presolar Grains. *ApJ*, **612**, 414–428.

Jose, J., Hernanz, M. & Coc, A., 1997. New Results on 26Al Production in Classical Novae. *ApJ*, **479**, L55+.

José, J., Hernanz, M. & Iliadis, C., 2006. Nucleosynthesis in classical novae. *Nuclear Physics A*, **777**, 550–578.

José, J. & Shore, S. N., 2008. Observational mysteries and theoretical challenges. In M. F. Bode & A. Evans, ed., *Classical Nova Explosions*, vol. 43 of *Cambridge Astrophysics*, 121–125. Cambridge: Cambridge University Press.

Kercek, A., Hillebrandt, W. & Truran, J. W., 1998. Two-dimensional simulations of the thermonuclear runaway in an accreted atmosphere of a C+O White Dwarf. *A&A*, **337**, 379–392.

Kercek, A., Hillebrandt, W. & Truran, J. W., 1999. Three-dimensional simulations of classical novae. *A&A*, **345**, 831–840.

Kippenhahn, R. & Thomas, H., 1978. Accretion belts on white dwarfs. *A&A*, **63**, 265–272.

Kolmogorov, A. N., 1991a. Dissipation of Energy in the Locally Isotropic Turbulence. *Royal Society of London Proceedings Series A*, **434**, 15–17.

Kolmogorov, A. N., 1991b. The local structure of turbulence in incompressible viscous fluid for very large Reynolds numbers. *Royal Society of London Proceedings Series A*, **434**, 9–13.

Kovetz, A. & Prialnik, D., 1985. CNO abundances resulting from diffusion in accreting nova progenitors. *ApJ*, **291**, 812–821.

Kovetz, A. & Prialnik, D., 1997. The Composition of Nova Ejecta from Multicycle Evolution Models. *ApJ*, **477**, 356–+.

Kraft, R. P., 1963. Novae:an historical perspective. In Z. Kopal, ed., *Advances in Astronomy and Astrophysics*, vol. 2, 43. New York and London: Academic Press.

Kraft, R. P., 1964. Binary Stars among Cataclysmic Variables. III. Ten Old Novae. *ApJ*, **139**, 457–+.

Krautter, J., 2008. X-ray emission from classical novae in outburst. In M. F. Bode & A. Evans, ed., *Classical Nova Explosions*, vol. 43 of *Cambridge Astrophysics*, 232–251. Cambridge: Cambridge University Press.

Kutter, G. S. & Sparks, W. M., 1987. Stellar accretion of matter possessing angular momentum. *ApJ*, **321**, 386–393.

Kutter, G. S. & Sparks, W. M., 1989. Modeling the classical nova outburst. I - Exploring the physics of a new mechanism. *ApJ*, **340**, 985–1005.

Landau, L. D. & Lifshitz, E. M., 1987. *Fluid mechanics*. Oxford: Pergamon Press.

Lapidus, A., 1967. A Detached Shock Calculation by Second-Order Finite Differences. *Journal of Computational Physics*, **2**, 154–+.

Leising, M. D. & Clayton, D. D., 1987. Positron annihilation gamma rays from novae. *ApJ*, **323**, 159–169.

Lesieur, M., Yaglom, A. & David, F., eds., 2001. *New trends in turbulence*.

Livio, M. & Truran, J. W., 1987. Spin-up and mixing in accreting white dwarfs. *ApJ*, **318**, 316–325.

Lohner, R., 1987. An adaptive finite element scheme for transient problems in CFD. *Computer Methods in Applied Mechanics and Engineering*, **61**, 323–338.

MacDonald, J., 1983. Mixing by shear instabilities in differentially rotating inhomogeneous stars with application to accreting white dwarf models for novae. *ApJ*, **273**, 289–298.

MacNeice, P., Olson, K. M., Mobarry, C., De Fainchtein, R. & Packer, C., 2000. PARAMESH: A parallel adaptive mesh refinement community toolkit. *Computer Physics Communications*, **126**, 330–354.

Malone, C. M., Nonaka, A., Almgren, A. S., Bell, J. B. & Zingale, M., 2011. Multidimensional Modeling of Type I X-ray Bursts. I. Two-dimensional Convection Prior to the Outburst of a Pure He-4 Accretor. *ApJ*, **728**, 118–+.

Meakin, C. A., 2006. *Hydrodynamic modeling of massive star interiors*. Ph.D. thesis, The University of Arizona, Arizona, USA.

Meakin, C. A. & Arnett, D., 2007. Turbulent Convection in Stellar Interiors. I. Hydrodynamic Simulation. *ApJ*, **667**, 448–475.

Monchmeyer, R. & Muller, E., 1989. A Conservative Second-Order Difference Scheme for Curvilinear Coordinates - Part One - Assignment of Variables on a Staggered Grid. *A&A*, **217**, 351.

Newton, I., 1726. *Philosophiae naturalis principia mathematica.* Colonia: A. Philibert.

Nittler, L. R. & Hoppe, P., 2005. Are Presolar Silicon Carbide Grains from Novae Actually from Supernovae? *ApJ*, **631**, L89–L92.

Nordhaus, J., Busso, M., Wasserburg, G. J., Blackman, E. G. & Palmerini, S., 2008. Magnetic Mixing in Red Giant and Asymptotic Giant Branch Stars. *ApJ*, **684**, L29–L32.

Paczyński, B., 1965. Cataclysmic Variables Among Binary Stars. II. Physical Parameters for Novae. *Acta Astron.*, **15**, 197–+.

Palmerini, S. & Busso, M., 2008. Al-26 production from magnetically induced extramixing in AGB stars. *New A Rev.*, **52**, 412–415.

Payne-Gaposchkin, C., 1957. Book Reviews: The Galactic Novae. *Science*, **126**, 1350–1351.

Pickering, W. H., 1895. A new star in Carina. *The Observatory*, **18**, 436–436.

Plewa, T. & Müller, E., 1999. The consistent multi-fluid advection method. *A&A*, **342**, 179–191.

Pope, S. B., 2000. *Turbulent Flows*. Cambrige: Cambridge University Press.

Potekhin, A. Y., Chabrier, G. & Yakovlev, D. G., 1997. Internal temperatures and cooling of neutron stars with accreted envelopes. *A&A*, **323**, 415–428.

Press, W. H., Flannery, B. P., Teukolsky, S. A. & Vetterling, W. T., 1996. *The art of scientific computing*. Cambridge: Cambridge University Press.

Prialnik, D. & Kovetz, A., 1984. The effect of diffusion on prenova evolution - CNO-enriched envelopes. *ApJ*, **281**, 367–374.

Rosner, R., Alexakis, A., Young, Y., Truran, J. W. & Hillebrandt, W., 2001. On the C/O Enrichment of Nova Ejecta. *ApJ*, **562**, L177–L179.

Sala, G. & Hernanz, M., 2005. Models for the soft X-ray emission of post-outburst classical novae. *A&A*, **439**, 1061–1073.

SCHATZMAN, E., 1949. Remarques sur le phénomène de novae. *Annales d'Astrophysique*, **12**, 281–+.

SCHATZMAN, E., 1951. Remarques sur le phénomène de Nova: IV. L'onde de détonation due à l'isotope ^{3}He. *Annales d'Astrophysique*, **14**, 294–+.

SEDOV, L. I., 1959. *Similarity and Dimensional Methods in Mechanics*. New York: Academic Press.

SHAFTER, A. W., 2002. The Galactic Nova Rate. In M. Hernanz & J. José, ed., *Classical Nova Explosions*, vol. 637 of *American Institute of Physics Conference Series*, 462–471.

SHANKAR, A. & ARNETT, D., 1994. Thermonuclear runaways in nova outbursts. 2: Effect of strong, instantaneous, local fluctuations. *ApJ*, **433**, 216–228.

SHANKAR, A., ARNETT, D. & FRYXELL, B. A., 1992. Thermonuclear runaways in nova outbursts. *ApJ*, **394**, L13–L15.

SHARA, M. M., 1982. Localized thermonuclear runaways and volcanoes on degenerate dwarf stars. *ApJ*, **261**, 649–660.

SHEN, K. J. & BILDSTEN, L., 2009. The Effect of Composition on Nova Ignitions. *ApJ*, **692**, 324–334.

SHORE, S. N., 2007. *Astrophysical Hydrodynamics: An Introduction*. San Francisco: John Wiley & Sons.

SHORE, S. N., 2008. Optical and ultraviolet evolution. In M. F. Bode & A. Evans, ed., *Classical Nova Explosions*, vol. 43 of *Cambridge Astrophysics*, 194–231. Cambridge: Cambridge University Press.

SHORE, S. N., LIVIO, M. & VAN DEN HEUVEL, E. P. J., eds., 1994a. *Interacting binaries*. Saas-Fee Advanced Course 22: Interacting Binaries.

SHORE, S. N., STARRFIELD, S., GONZALEZ-RIESTRAT, R., HAUSCHILDT, P. H. & SONNEBORN, G., 1994b. Dust formation in Nova Cassiopeiae 1993 seen by ultraviolet absorption. *Nature*, **369**, 539–541.

SHORE, S. N., STARRFIELD, S. & SONNEBORN, G., 1996. The Ultraviolet and X-Ray View of the Demise of Nova V1974 Cygni. *ApJ*, **463**, L21+.

SHU, C. & OSHER, S., 1989. Efficient Implementation of Essentially Non-oscillatory Shock-Capturing Schemes, II. *Journal of Computational Physics*, **83**, 32.

SOD, G. A., 1978. A survey of several finite difference methods for systems of nonlinear hyperbolic conservation laws. *Journal of Computational Physics*, **27**, 1–31.

SPARKS, W. M., 1969. Dynamical Models of Novae. *ApJ*, **156**, 569–+.

SPARKS, W. M. & KUTTER, G. S., 1987. Nuclear runaways in a C/O white dwarf accreting H-rich material possessing angular momentum. *ApJ*, **321**, 394–403.

STARRFIELD, S., 1989. Thermonuclear processes and the classical nova outburst. In M. F. Bode & A. Evans, ed., *Classical Nova Explosions*, 39. New York: John Wiley & Sons.

STARRFIELD, S., ILIADIS, C. & HIX, W. R., 2008. Thermonuclear processes. In M. F. Bode & A. Evans, ed., *Classical Nova Explosions*, vol. 43 of *Cambridge Astrophysics*, 77–82. Cambridge: Cambridge University Press.

STARRFIELD, S., ILIADIS, C., HIX, W. R., TIMMES, F. X. & SPARKS, W. M., 2009. The Effects of the pep Nuclear Reaction and Other Improvements in the Nuclear Reaction Rate Library on Simulations of the Classical Nova Outburst. *ApJ*, **692**, 1532–1542.

STARRFIELD, S., SPARKS, W. M. & TRURAN, J. W., 1974. CNO abundances and hydrodynamic models of the nova outburst. II - 1.00 solar mass models with enhanced carbon and oxygen. *ApJS*, **28**, 247–270.

STARRFIELD, S., TRURAN, J. W., SPARKS, W. M. & KUTTER, G. S., 1972. CNO Abundances and Hydrodynamic Models of the Nova Outburst. *ApJ*, **176**, 169–+.

STARRFIELD, S., TRURAN, J. W., WIESCHER, M. C. & SPARKS, W. M., 1998. Evolutionary sequences for Nova V1974 Cygni using new nuclear reaction rates and opacities. *MNRAS*, **296**, 502–522.

STRANG, G., 1968. On the Construction and Comparison of Difference Schemes. *SIAM Journal on Numerical Analysis*, **5**, 506–517.

TIMMES, F. X., 1999. Integration of Nuclear Reaction Networks for Stellar Hydrodynamics. *ApJS*, **124**, 241–263.

TIMMES, F. X., 2000. Physical Properties of Laminar Helium Deflagrations. *ApJ*, **528**, 913–945.

TIMMES, F. X. & ARNETT, D., 1999. The Accuracy, Consistency, and Speed of Five Equations of State for Stellar Hydrodynamics. *ApJS*, **125**, 277–294.

TIMMES, F. X. & SWESTY, F. D., 2000. The Accuracy, Consistency, and Speed of an Electron-Positron Equation of State Based on Table Interpolation of the Helmholtz Free Energy. *ApJS*, **126**, 501–516.

TIMMES, F. X., ZINGALE, M., OLSON, K., FRYXELL, B., RICKER, P., CALDER, A. C., DURSI, L. J., TUFO, H., MACNEICE, P., TRURAN, J. W. & ROSNER, R., 2000. On the Cellular Structure of Carbon Detonations. *ApJ*, **543**, 938–954.

VAN LEER, B., 1979. Towards the ultimate conservative difference scheme. V - A second-order sequel to Godunov's method. *Journal of Computational Physics*, **32**, 101–136.

WALKER, M. F., 1954. Nova DQ Herculis (1934): an Eclipsing Binary with Very Short Period. *PASP*, **66**, 230–+.

WARNER, B., 2008. Properties of novae: an overview. In M. F. Bode & A. Evans, ed., *Classical Nova Explosions*, vol. 43 of *Cambridge Astrophysics*, 16–33. Cambridge: Cambridge University Press.

WEAVER, T. A., ZIMMERMAN, G. B. & WOOSLEY, S. E., 1978. Presupernova evolution of massive stars. *ApJ*, **225**, 1021–1029.

WILLIAM, F. A., 1985. *Combustion Theory*. Berkeley: Perseus Books.

WOODWARD, P. & COLELLA, P., 1984. The numerical simulation of two-dimensional fluid flow with strong shocks. *Journal of Computational Physics*, **54**, 115–173.

WOOSLEY, S. E., 1986. Nucleosynthesis and Stellar Evolution. In J. Audouze, C. Chiosi, & S. E. Woosley, ed., *Saas-Fee Advanced Course 16: Nucleosynthesis and Chemical Evolution*, 1–+.

YAKOVLEV, D. G. & SHALYBKOV, D. A., 1989. Degenerate Cores of White Dwarfs and Envelopes of Neutron Stars - Thermodynamics and Plasma Screening in Thermonuclear Reactions. *Astrophysics and Space Physics Reviews*, **7**, 311–+.

YAKOVLEV, D. G. & URPIN, V. A., 1980. Thermal and Electrical Conductivity in White Dwarfs and Neutron Stars. *Soviet Ast.*, **24**, 303–+.

YARON, O., PRIALNIK, D., SHARA, M. M. & KOVETZ, A., 2005. An Extended Grid of Nova Models. II. The Parameter Space of Nova Outbursts. *ApJ*, **623**, 398–410.

ZALESAK, S. T., 1978. Fully multidimensional flux-corrected transport. Tech. rep., Naval Research Lab.

ZINGALE, M., DURSI, L. J., ZUHONE, J., CALDER, A. C., FRYXELL, B., PLEWA, T., TRURAN, J. W., CACERES, A., OLSON, K., RICKER, P. M., RILEY, K., ROSNER, R., SIEGEL, A., TIMMES, F. X. & VLADIMIROVA, N., 2002. Mapping Initial Hydrostatic Models in Godunov Codes. *ApJS*, **143**, 539–565.

ZINGALE, M., TIMMES, F. X., FRYXELL, B., LAMB, D. Q., OLSON, K., CALDER, A. C., DURSI, L. J., RICKER, P., ROSNER, R., MACNEICE, P. & TUFO, H. M., 2001. Helium Detonations on Neutron Stars. *ApJS*, **133**, 195–220.

ZINGALE, M. A., 2000. *Helium detonations on neutron stars*. Ph.D. thesis, The University of Chicago.